

**The Observation of Enhanced Thomson  
Scattering in Submicron-Laser Plasmas**

by

**Steven Howard Batha**

Submitted in Partial Fulfillment  
of the  
Requirements for the Degree  
DOCTOR OF PHILOSOPHY

Supervised by Professor David D. Meyerhofer  
Department of Mechanical Engineering  
College of Engineering and Applied Science

University of Rochester  
Rochester, New York

1989

**© Copyright by Steven Howard Batha 1989**

**All Rights Reserved**

## *Curriculum Vitae*

The author was born on March 20, 1961 in Buffalo, New York. He entered Dartmouth College as a National Merit Scholar in 1979 and received a Bachelor of Arts degree with honors in physics in 1983. Later that year he entered the graduate program in mechanical engineering at the University of Rochester. He was awarded a Master of Science degree in Mechanical and Aerospace Sciences by the College of Engineering and Applied Science in 1984. He held a Mechanical Engineering Departmental Fellowship in 1983-84. Subsequent to 1984, he held an appointment as an LLE Fellow. In 1987-88, he was a Link Energy Foundation Fellow. His thesis research was supervised by Professor Leonard M. Goldman until Professor Goldman's retirement in 1987 and was completed under the supervision of Professor David D. Meyerhofer.

## Acknowledgments

The author would like to acknowledge the significant contributions made to the understanding and direction of this work by his advisors, Professor David D. Meyerhofer and Professor Leonard M. Goldman. Without their critical evaluation and probing questions, many of the details and subtleties of this series of experiments would have been lost. Special thanks go to Professor Albert Simon for always answering questions about his theory, to Mr. Raymond Bahr and Professor Wolf Seka for teaching me how to be an experimental plasma physicist, and to Dr. Robert Keck for helping me reactivate the x-ray continuum spectrometer.

The staff of the Laboratory for Laser Energetics has made the production of this dissertation and the experiments that are described within it much easier. Specifically, the author would like to thank Mr. W. Beich, Mr. W. Lockman, Miss N. Wong, and Miss E. Roberts of GDL operations, Ms. Mary Strife, LLE librarian, and L. Boyle and L. Cardone of word processing for always being of assistance. Mr. E. Kowaluk always willingly discussed photographic processing and analysis with me. The author would also like to thank the plasma physics group at Lawrence Livermore National Laboratory for the invitation to perform the experiments on the Nova laser system. Dr. R. Paul Drake, Dr. Chris Darrow, and Mr. David Montgomery are singled out.

Dr. Jacques Delettrez and Dr. R. Stephen Craxton very generously shared the results of many computer simulations with me. It has been a joy to collaborate with Professor Colin McKinstrie on many different projects over the past six years. The author would like to thank my colleague, Mr. Lawrence Kingsley, for many useful discussions and much thoughtful advice for many years. And of course, without Margo's loving encouragement, this dissertation could not have been finished.

# **The Observation of Enhanced Thomson Scattering in Submicron-Laser Plasmas**

## *Abstract*

Frequency up-scattered light produced by laser-plasma interaction was measured under three different plasma conditions. The corresponding down-scattered light was also observed. The measured wavelengths were, in all cases, in good agreement with the results of the enhanced Thomson scattering (ETS) theory. The up-scattered band, shifted to a frequency higher than the laser frequency  $\omega_0$ , had not previously been systematically studied. The other was down-shifted in frequency to between  $\omega_0$  and  $\omega_0/2$  and typically has been referred to as the Raman scattering band.

Enhanced Thomson scattering is not an instability, but rather depends on the presence of nonlinear plasma processes (resonance absorption) and instabilities (stimulated Raman scattering or two plasmon decay) to produce fast and superfast electrons, respectively, that enhance background plasma waves to large amplitudes. Incoming laser light scatters from the enhanced density fluctuations into two “plasma-line” features, one on each side of the laser frequency. The position of these bands depends on the fast and superfast electron temperatures through the phase velocity of the plasma waves that are enhanced.

The primary variation in the plasmas studied was in scale length. Variations were produced by changing laser parameters such as wavelength and energy. The first experiment was conducted using a 60-J, single-beam, 527-nm laser focused to a small

spot, producing a scale length of about 80  $\mu\text{m}$ . The presence of fast electrons from resonance absorption was inferred. The second experiment was performed using a ten-beam, 20-kJ, 351-nm laser. Nine low-intensity beams were used to produce an ultra-long-scale-length plasma with a scale length of approximately 5,000 laser wavelengths. The tenth, or “interaction,” beam, obliquely incident on a 15- $\mu\text{m}$ -thick CH foil, was delayed 2.7 ns to simulate interaction with a reactor-type target. The third experiment was conducted using a single-beam, 2-kJ, 351-nm, high-intensity laser which created a plasma with a 200- $\mu\text{m}$  scale length.

# Table of Contents

<i>Curriculum Vitae</i> .....	iii
Acknowledgments .....	iv
Abstract .....	v
List of Tables .....	ix
List of Figures .....	x
I. Introduction .....	1
A. Plasma Processes in the Corona .....	3
B. Enhanced Thomson Scattering .....	8
C. Summary .....	9
II. Theory .....	12
A. Ordinary Thomson Scattering .....	13
B. Scattering from Non-Equilibrium Plasmas .....	23
C. Enhanced Thomson Scattering in a Laser-Produced Plasma .....	36
D. Predictions of the Theory .....	49
E. Alternative Theory .....	55
F. Summary .....	62
III. Enhanced Thomson Scattering Experiments at 0.53 $\mu\text{m}$ .....	63
A. Experiment .....	64
B. Results .....	74
C. Discussion .....	85
D. Summary .....	89
IV. Long-Scale-Length Experiments .....	91

A.	Experiment .....	92
B.	Results .....	100
C.	Discussion .....	114
D.	Summary .....	131
V.	Single-Beam Experiments at 0.35 $\mu\text{m}$ .....	134
A.	Experiment .....	135
B.	Results .....	135
C.	Discussion .....	145
D.	Summary .....	151
VI.	Discussion and Conclusion .....	153
A.	Success of Theory .....	153
B.	Deviations from the Theory .....	158
C.	Scale-Length and Wavelength Effects .....	163
D.	Conclusion .....	164
A.	LLE Experiments .....	166
1.	GDL Intensity Determination .....	166
2.	GDL Diagnostics .....	171
3.	Data Analysis .....	172
B.	Film Calibration .....	175
C.	LLNL Experiments .....	181
1.	Nova Laser Conditions .....	181
2.	Optical Diagnostics .....	182
3.	Data Analysis .....	186
	References .....	190



## List of Tables

I-1	Parametric Instabilities.....	6
IV-1	Long-Scale-Length Shots at LLNL.....	101
V-1	Single-Beam Shots at LLNL.....	144
VI-1	Typical Plasma Conditions.....	155
B-1	Film Processing.....	178

## List of Figures

I-1	Feedback Mechanism for SRS.....	5
I-2	Plasma Coupling Processes.....	7
II-1	Salpeter Spectral-Density Function.....	24
II-2	Bump-on-Tail Instability .....	47
II-3	Large Region with No Damping.....	48
II-4	ETS Predicted Scattering Bands.....	53
II-5	Spectral "Gaps".....	57
III-1	GDL ETP.....	66
III-2	Target/Observation Geometries.....	69
III-3	Streak-Camera Setup.....	70
III-4	Time-Integrated Electron Temperatures.....	73
III-5	Time-Integrated Down-Scattering .....	75
III-6	Time-Integrated Up-Scattering.....	76
III-7	ETS Calculated Scattering Bands.....	78
III-8	Time-Resolved Down-Scattering .....	79
III-9	Variations in Down-Scattering .....	81
III-10	Down-Scattering Appears in Bursts.....	83
III-11	Two Components in Up-Scattering .....	84
III-12	Complete Scattered-Light Spectrum.....	86
III-13	ETS Predicted Scattering Bands for a Tilted Target.....	87

IV-1	Nova System Timing .....	94
IV-2	Irradiation Geometry.....	96
IV-3	Diagnostic Geometry.....	98
IV-4	Optical Spectra from the Interaction Shot.....	102
IV-5	Temporal History of Up-Scattering and $3\omega_0/2$ Emission.....	105
IV-6	Temporal Evolution of Maximum On-Axis Electron Density .....	106
IV-7	Isodensity Contours at Start of Interaction Pulse.....	107
IV-8	Correlation Between Up- and Down-Scattering .....	109
IV-9	Optical Spectra from the Null Shot.....	110
IV-10	Temporal History of Interaction and Null Shot.....	112
IV-11	FFLEX Measurement of Time-Integrated Electron Temperatures.....	113
IV-12	Simultaneous Up- and Down-Scattering .....	115
IV-13	Calculated ETS Bands .....	116
IV-14	Electron Temperature Contours During Interaction Pulse .....	118
IV-15	Phase-Velocity Symmetry of Up- and Down-Scattering .....	120
IV-16	Density at Origin of Scattering.....	122
IV-17	Observed Scattering Plasma Waves.....	125
IV-18	Frequency Shift of Up- and Down-Scattering .....	126
IV-19	Measured Variation in Width of Up-Scattering Band .....	128
IV-20	Enhanced Thomson Scattering Early in Time.....	130
IV-21	Enhanced Thomson Scattering During Null Shot .....	132
V-1	Temporal Evolution of a CH target.....	136
V-2	Scattered-Light Spectrum from Shot 18012208.....	138

V-3	Anomalous $3\omega/2$ Emission .....	139
V-4	Spectrum at Time I of Shot 18012906.....	140
V-5	Spectrum at Time II of Shot 18012906.....	141
V-6	Scattered-Light Spectrum from a Au Target.....	143
V-7	Down-Scattering Details.....	146
V-8	Density Profile at Burn-Through of a CH Target.....	147
V-9	Density Profile at 500 ps of a CH Target.....	149
A-1	Pinhole-Camera X-Ray Image.....	168
A-2	GDL Focus Scan .....	170
A-3	Streak Camera Wavelength Calibration.....	173
B-1	Spectral Response of Two Kodak Films .....	176
B-2	Film Response of Four Kodak Films.....	180
C-1	SOS-II Light-Collection Optics.....	183
C-2	Transmission of Light-Collection Optics .....	185
C-3	Wave-Vector-Matching Diagrams .....	189

# Chapter I: Introduction

There are two ways to harvest large amounts of energy from the atom: fission and fusion. Fission is the splitting apart of large nuclei to smaller, more stable ones. The excess binding energy is converted into heat through the release of energetic neutrons. This well understood process has been known since 1940;<sup>1</sup> however, in the past 20 years, many disadvantages have been discovered, including the real and perceived danger of accidents and disposal of radioactive wastes from nuclear (fission) power plants.

Fusion, the merging of two light elements to make a heavier element,



does not have most of these disadvantages. The reaction is not a chain reaction and the radioactive wastes generated by fusion, primarily through activation of the support structure and fuel-handling equipment, have much shorter half-lives than those produced by fission. There is also much less radioactive waste produced.

The two major areas of fusion research differ in their approaches to confining and heating the fuel. Magnetic confinement fusion (MCF) relies on magnetic bottles to confine the fuel. Heating is done by electric fields, neutral particle beams, or rf waves. Inertial confinement fusion (ICF) uses the mass of the fuel itself to confine the fuel. Direct-drive ICF uses large laser or particle beams that are focused onto small glass microballoons containing the fuel. The beams heat the outside of the pellet and cause the surface of the pellet to ablate. To conserve momentum, the inside surface of the pellet must move inward (the "rocket effect"). The pellet implodes and the fuel is compressed to hundreds of times its initial density. It is also adiabatically heated as it is

compressed. Indirect-drive ICF, some details of which are still classified, first converts the laser energy into x rays which then implode the pellet.

Important proof-of-principle experiments in the last year have shown the viability of ICF. Direct-drive target experiments at the University of Rochester have achieved compression of greater than one hundred times liquid fuel density by utilizing cryogenically cooled DT targets and by using extremely uniform target-irradiation conditions produced by distributed phase plates.<sup>2</sup> By using an optimized indirect-drive target, Lawrence Livermore National Laboratory has achieved a volume compression ratio of about  $3 \times 10^4$  and a neutron yield that is essentially in agreement with spherical implosion calculations.<sup>3</sup> In addition, target ignition has been apparently achieved, in classified experiments, using the radiation from a nuclear weapon as the driver.<sup>4</sup>

Many problems and challenges remain to be overcome before commercial ICF power becomes available. Two of the major difficulties are energy coupling and fuel preheat by fast electrons. Energy coupling is important because the overall efficiency of the process is proportional to absorption efficiency. Fast-electron generation is a problem because the electrons can deposit their energy in the cold fuel before the imploding shock front can compress the fuel, reducing the overall efficiency of the fusion reaction because the compression occurs on a higher adiabat. The origin of both problems is in the pellet corona. Not surprisingly, the high temperatures and short time scales of an ICF interaction produce a plasma around the pellet. Laser light will propagate through a plasma if the electron plasma frequency,  $\omega_p [= (4\pi e^2 n_e / m_e)^{1/2}]$ , is less than the laser frequency,  $\omega_0$ . The plasma is termed *overdense* where  $\omega_p > \omega_0$  and *underdense* where  $\omega_p < \omega_0$ . The *critical density*,  $n_c$ , is the density at which the laser light is reflected (i.e., where  $\omega_p = \omega_0$ ). The pellet corona is then the entire region where the plasma density is less than the critical density. It is here where the laser light

is absorbed and fast electrons are produced.

### **A. Plasma Processes in the Corona**

Laser light is absorbed primarily due to inverse bremsstrahlung (IB) and resonance absorption (RA).<sup>5</sup> Inverse bremsstrahlung, also known as collisional absorption, occurs when an electron absorbs a photon during a collision with an ion. Consequently, in a laser plasma, the electrons are heated and the laser beam is absorbed. Inverse bremsstrahlung occurs only in the corona because the laser cannot penetrate the critical surface.

Resonance absorption (RA) causes laser energy to be converted into electron suprathermal energy at the critical surface of the plasma when there is a component of the laser electric field parallel to the density gradient. The electric field excites resonant plasma waves at the critical surface which are then damped. Since any laser beam has a non-zero divergence, RA is always possible. Hot electrons are then created by wavebreaking — a situation where the electric field has grown large enough at the critical density surface that electrons are accelerated through it in less than one oscillation period.<sup>6</sup> Resonance absorption is important with 1- $\mu\text{m}$  and 0.53- $\mu\text{m}$  lasers, but is less important for 0.351- $\mu\text{m}$ -laser irradiation, because with shorter laser wavelengths the collision frequency is higher, leading to higher absorption due to IB and consequently less absorption by RA.

Parametric instabilities may also produce hot electrons. In stimulated Raman scattering, a typical parametric instability, an initial noise source in the electron density ( $\delta n$ ) interacts with the electric field of the laser to give rise to a transverse current ( $\delta n \cdot E_0$ ). The current radiates a scattered wave,  $E_s$ . The ponderomotive force

between the two light waves,  $\nabla(\mathbf{E}_0 \cdot \mathbf{E}_S)$ , causes density perturbations,  $\delta n$ , that reinforce the initial noise sources. Thus, the density fluctuations and scattered light levels grow exponentially. The most common parametric instabilities in a laser plasma are three-wave interactions whose pump,  $(\omega_0, \mathbf{k}_0)$ , and daughter waves,  $(\omega_{1,2}, \mathbf{k}_{1,2})$ , satisfy energy- and momentum-matching conditions:

$$\omega_0 = \omega_1 + \omega_2 \quad (\text{I-2})$$

$$\mathbf{k}_0 = \mathbf{k}_1 + \mathbf{k}_2 \quad (\text{I-3})$$

The rate of energy transfer between the pump and daughter waves increases with time. The feedback loops for each instability are similar and an example of a feedback loop for one such instability, the stimulated Raman scattering instability (SRS), is shown in Figure I-1. The pump wave is the laser, and the daughter waves are a scattered light wave,  $(\omega_s, \mathbf{k}_s)$ , and a plasma wave,  $(\omega_p, \mathbf{k}_p)$ . The SRS instability may be either convective, where the wave grows as it moves through the plasma, or absolute, where the growth of the wave is temporal only.

There are other parametric instabilities besides SRS. These are summarized in Table I-1 and the regions in the laser plasma where these instabilities occur are shown in Figure I-2. The first two (SRS and SBS) are very detrimental to ICF because they reflect large amounts of the laser light and thereby limit the amount of energy absorbed. Up to 10% of the incident energy may be reflected by SRS in a plasma created by a 1.06- $\mu\text{m}$  laser<sup>7</sup> and up to several percent is reflected by SRS in a 0.53- $\mu\text{m}$ -laser plasma.<sup>8</sup> Increased reflectance is also found when Brillouin scattering is present.<sup>9-11</sup>

Inverse bremsstrahlung raises the average thermal level of the electrons in the plasma while resonance absorption creates hot electrons that are substantially hotter than the thermal background temperature. The two plasmon decay and absolute SRS (SRS-A) instabilities create still more energetic electrons, called superhot electrons, at



## Feedback Mechanism for SRS

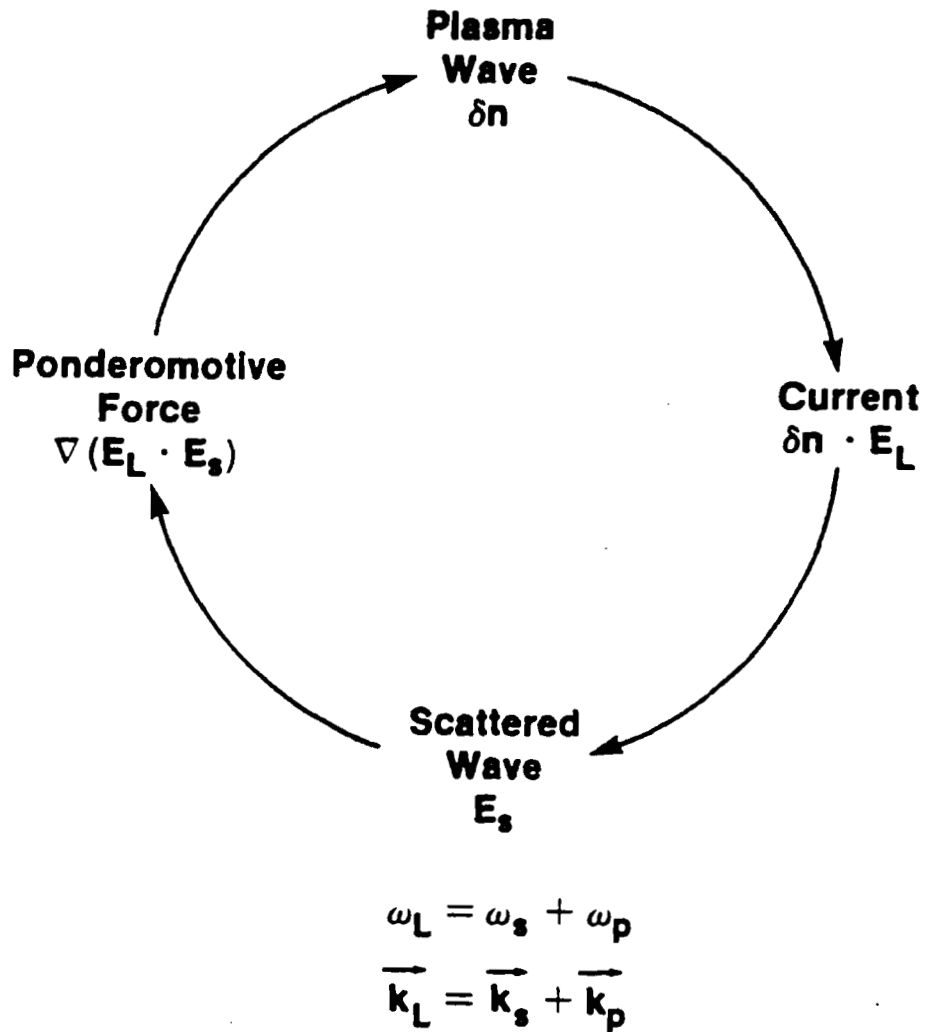


Figure I-1. The feedback loop for the stimulated Raman scattering instability. The instability is driven by the interaction between an initial electron-density perturbation (noise) that produces a transverse current, due to the oscillatory pump wave, which in turn produces a scattered EM wave. The ponderomotive force of the interacting incident and scattered EM waves enhances the initial density perturbations.

---

**Table I-1: Parametric Instabilities**


---

Stimulated Brillouin Scattering	(SBS)	$\omega_0 \rightarrow \omega_s + \omega_{ia}$
Stimulated Raman Scattering	(SRS)	$\omega_0 \rightarrow \omega_s + \omega_p$
Parametric Decay Instability	(PDI)	$\omega_0 \rightarrow \omega_{ia} + \omega_p$
Two Plasmon Decay Instability	(TPD)	$\omega_0 \rightarrow \omega_p + \omega_p$

---

$\omega_0$  = incident laser

$\omega_{ia}$  = ion-acoustic wave

$\omega_p$  = plasma wave

$\omega_s$  = scattered light wave

---

# Plasma Coupling Processes

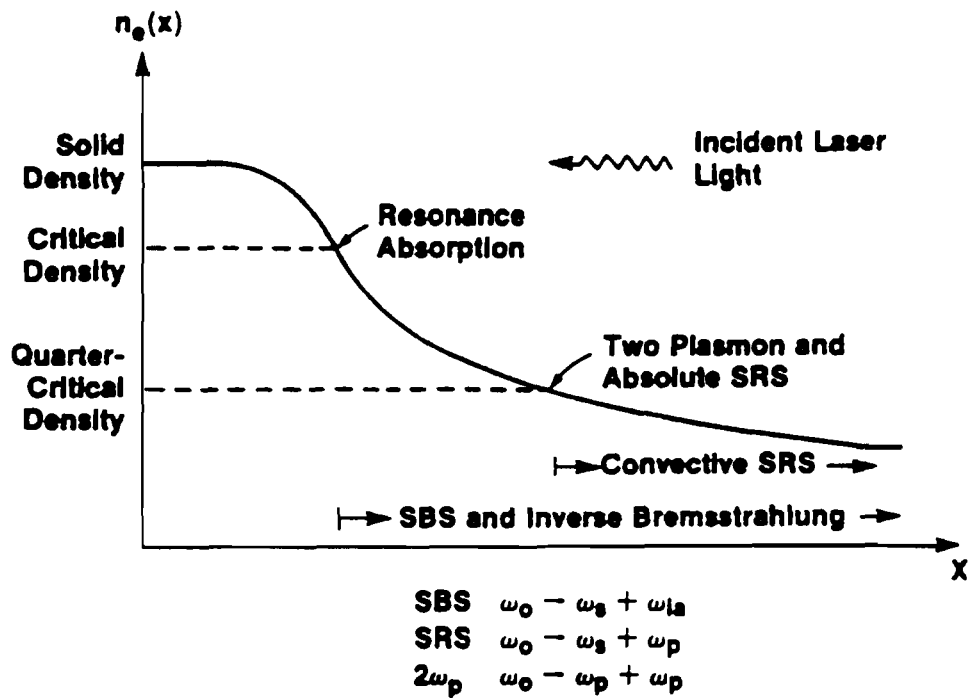


Figure I-2. Plasma coupling processes occur in the corona where  $\omega_p < \omega_0$ . Some instabilities are restricted to certain density regions by frequency and wave-number matching conditions.

the quarter-critical density surface. Therefore, there may be three components to the electron-temperature distribution: a cold background from IB, a hot component from RA at the critical surface, and a superhot component from SRS-A or TPD at the quarter-critical surface.

## B. Enhanced Thomson Scattering

The plasma processes presented in the last section also lead to another reaction: enhanced Thomson scattering (ETS).<sup>12,13</sup> Physically, ETS is the scattering of the pump wave from density fluctuations that have been enhanced by the presence of suprathermal electrons. The scattered light is emitted in two frequency bands; one is up-scattered to a frequency higher than the laser frequency and the other is down-scattered to a lower frequency. More than one pair of bands may be present if both hot- and superhot-electron components are present.

Particular care must be used to distinguish between three related, but different processes that occur in a plasma. *Ordinary Raman scattering* (ORS), in general, refers to the scattering of frequency up- and down-shifted EM waves as the result of the interaction of an incident wave with an electron-plasma wave. *Stimulated Raman scattering* (SRS), refers to a special form of this in which feedback between the pump wave, the scattered EM wave, and the plasma wave produces a parametric instability with exponential growth of the daughter waves.

Thomson scattering<sup>14,15</sup> of a laser by a plasma is a powerful diagnostic in which a probe laser is scattered into two “electron-line” features whose shift from the laser frequency is equal to the Bohm-Gross frequency [ $\Delta\omega = (\omega_{pe}^2 + 3k^2 v_e^2)^{1/2}$ ]. In terminology reminiscent of the density and temperature diagnostic, *enhanced Thomson*

*scattering* refers to the large increase in scattering into the electron-line frequency when the local plasma-wave amplitude is enhanced by the presence of a non-Maxwellian distribution of electrons. This is also a form of ordinary Raman scattering. For this reason, ETS has also been called “Enhanced Incoherent Ordinary Raman Scattering” (EIORS).<sup>12</sup>

Enhanced Thomson scattering may be an obstacle to achieving fusion because it is yet another process that increases the reflectivity of the plasma. It is also a signature of processes detrimental to achieving fusion that are occurring elsewhere in the plasma corona. In particular, ETS is a signature of suprathermal electron production.

Current theories of the convective SRS instability (SRS-C) predict a threshold intensity that is much higher than the experimentally observed threshold of down-scattered light while ETS has no threshold, *per se*. The enhanced Thomson scattering bands can be confused with the scattered light from SRS-C, as will be discussed later. This may mean that the classic theories on the production of SRS-C may actually be in better agreement with experiments than previously thought. It also means, however, that the overall picture of coronal physics must be modified to explicitly include the production of up-scattered light bands.

### C. Summary

This dissertation shows the existence of ETS in several different experiments under widely varying conditions. In all cases, the measured wavelengths of the up-and down-scattered bands were found to be in good agreement with the theoretical predictions.

The theory of enhanced Thomson scattering is discussed in Chapter II,

beginning with classical Thomson scattering of an EM wave from a free electron. Perkins and Salpeter's<sup>14</sup> derivation of scattering from the ionosphere when the electron distribution contains energetic electrons is reviewed and then Simon's<sup>12</sup> generalization to a nonuniform plasma is presented. The chapter concludes with a discussion of competing theories, including SRS-C and anti-Stokes generation.

Chapter III reports the results of experiments performed at the Laboratory for Laser Energetics using the single-beam Glass Development Laser operating at 0.527  $\mu\text{m}$ . The plasmas created had moderate scale lengths and were characterized by a three-component electron-temperature distribution. Scattering bands at frequencies above  $3\omega_0/2$  were observed on the same target shots as down-scattered bands were observed, eliminating the possibility that the up-scattered light was the anti-Stokes mode of the SRS-C instability.

A very different experiment was conducted at Lawrence Livermore National Laboratory using the Nova laser operating at 0.351  $\mu\text{m}$  and is described in Chapter IV. A high-intensity laser beam was passed through a preformed plasma that had an ultra-long scale length. Time-resolved up- and down-scattered spectra, as well as time-integrated hot-electron temperatures, were collected and are included in Chapter IV.

A single-beam experiment was also performed using a single arm of Nova. This provided a good contrast to the GDL experiments, since the experiment was conducted at 0.351  $\mu\text{m}$  with thirty times the laser energy and six times the laser intensity. These results are presented in Chapter V. In this case, both ETS and SRS were observed on the same shots.

A summary of the experimental results is given in Chapter VI. The applicability of the ETS theory under the three very different irradiation conditions is also discussed.

For the three experiments, the ETS theory accurately reproduces the position of the down-scattered band, the appearance and position of the up-scattered band, and explains the appearance of both scattered-light bands even below the theoretical convective stimulated Raman scattering threshold. Deviations from the theory are also discussed.

The appendices contain additional explanations of the experiments. Appendix A describes the GDL system and the diagnostics used in that experiment in more depth. Appendix B discusses an experiment that measured the absolute responses of several films that are important in the interpretation of the GDL experiments. Appendix C describes the Nova laser system and the diagnostics used in that experiment.

## Chapter II: Theory

Thomson scattering is the process by which an electromagnetic wave accelerates an electron, causing it to radiate. This description can be generalized to include the scattering of a laser (or microwave) beam from collections of electrons in a plasma. The application of this theory has resulted in a very powerful diagnostic for measuring the temperature and density of low-density plasmas such as occur in tokamaks<sup>16</sup> and CO<sub>2</sub>-laser-produced plasmas.<sup>17</sup> The scattering theory has been extended to include plasmas that can be described by a non-Maxwellian temperature distribution.<sup>14</sup> This has been particularly useful in ionospheric experiments where solar ultraviolet and x rays have heated a small fraction of the free electrons to very high temperatures as compared to the background electron temperature. In a laser plasma, there may be three different electron temperatures present: a cold background temperature from bulk heating of the plasma, a hot temperature created by the resonance absorption of laser light at the critical surface, and a superhot component created by either the two plasmon decay or the absolute stimulated Raman scattering instability at the quarter-critical plasma-density surface.

This chapter will quickly review the ordinary Thomson scattering theory and Salpeter's approximation that describes the plasma density and temperature diagnostic. Then, following Perkins and Salpeter,<sup>14</sup> the case of non-Maxwellian plasmas will be presented, treating first the collisionless case to show the effects of Landau damping, and then the collisional case. Simon's generalization<sup>12,13</sup> to a nonuniform plasma is straightforward if an average "directed velocity" of the electrons can be defined in terms of the measured electron temperatures. The primary result of this theory is the



prediction of “scattering bands” whose wavelength and presence are not predicted by the usual parametric instabilities present in a laser plasma. In particular, the appearance of “gaps” in the scattered light spectrum are predicted by this theory.

It will be shown that the most important factors in determining the wavelength of the scattered light are the hot or superhot electron temperature and the angle between the laser and the density gradient. The wavelength shift is greater for hotter electron temperatures. The angle not only determines the direction of the emitted light, but also how much the light is subsequently refracted. Other factors, such as the average ionic charge of the plasma and the bulk electron temperature, have a lesser effect.

Several competing theories have been advanced to explain anomalies in the scattered light spectrum, particularly the existence of a “gap” between the down-scattered light and the plasma emission at  $\omega_0/2$ . Only one other explanation has been offered to explain the existence of up-scattered features (those at higher frequencies than the laser). These theories are touched upon briefly to act as a basis for comparison in the succeeding chapters describing the results of the experiments.

Finally, the major results are summarized and a brief discussion of the assumptions and limits of the enhanced Thomson scattering model are given.

## A. Ordinary Thomson Scattering

A free electron will scatter electromagnetic radiation. The *effective scattering cross section*<sup>18</sup> of the interaction is defined as the power scattered into a given solid angle divided by the incident power. This can be calculated as follows. First, consider a plane, linearly polarized wave with an electric field

$$\mathbf{E}_i = \mathbf{E}_{i0} \cos(\mathbf{k} \cdot \mathbf{r} - \omega_i t + \alpha) ,$$

propagating in the  $\hat{n}$  direction incident on an electron at rest. The subscript "i" will denote the incident wave. The force due to the magnetic field of the EM wave is negligible if it is assumed that the velocity of the electron is very much less than the speed of light. By defining the dipole moment as  $\mathbf{d} = e\mathbf{r}$ , the equation of motion of the electron leads to

$$\frac{d^2\mathbf{d}}{dt^2} = \frac{e^2}{m} \mathbf{E}_i . \quad (\text{II-1})$$

Since it is assumed that the velocity of the unperturbed electron is small, the scattered radiation is at the same frequency as the incident radiation ( $\omega_s = \omega_i$ ) and the scattered intensity into a solid angle  $d\Omega$  is given by the dipole radiation formula<sup>19</sup>

$$dI = \frac{e^4}{4\pi m^2 c^3} (\mathbf{E}_i \times \hat{n})^2 d\Omega . \quad (\text{II-2})$$

The unit vector  $\hat{n}$  is in the scattering direction. The scattering cross section is defined to be

$$d\sigma = \frac{dI}{S_i} , \quad (\text{II-3})$$

where  $S_i = cE_i^2/4\pi$  is the magnitude of the Poynting vector of the incident wave.

Letting  $\theta$  be the angle between  $\mathbf{E}_{i0}$  and  $\hat{n}$  yields

$$d\sigma = \left( \frac{e^2}{mc^2} \right)^2 \sin^2\theta d\Omega . \quad (\text{II-4})$$

The *Thomson cross section* is then obtained by integrating Eq. (II-4) over all angles,

$$\alpha_T = \frac{8\pi}{3} \left( \frac{e^2}{mc^2} \right)^2 = \frac{8\pi}{3} r_0^2 , \quad (\text{II-5})$$

where  $r_0 (= 2.82 \times 10^{-13} \text{ cm})$  is the classical electron radius.

The differential scattering cross section of unpolarized light is also easily calculated, assuming  $\psi$  is the scattering angle between the incident and scattered wave vectors, to be<sup>18</sup>

$$d\sigma = \frac{1}{2} \left( \frac{e^2}{mc^2} \right)^2 (1 + \cos^2\psi) d\Omega . \quad (\text{II-6})$$

Scattering of elliptically polarized light is of interest because the Glass Development Laser at the Laboratory for Laser Energetics has a slight elliptical polarization.<sup>20</sup> If the incident laser has an electric field of

$$\mathbf{E} = \mathbf{A} \cos(\omega t + \alpha) + \mathbf{B} \sin(\omega t + \alpha)$$

with  $\mathbf{A}$  and  $\mathbf{B}$  perpendicular to each other, the scattering cross section is given by<sup>18</sup>

$$d\sigma = \left( \frac{e^2}{mc^2} \right)^2 \frac{(\mathbf{A} \times \hat{\mathbf{n}})^2 + (\mathbf{B} \times \hat{\mathbf{n}})^2}{A^2 + B^2} d\Omega . \quad (\text{II-7})$$

The frequency of the scattered radiation is different than the incident frequency if the restriction of small electron velocity is relaxed. The assumption that  $v \ll c$  is retained, however, so that the magnetic field contribution to the scattered power is zero. The equation of motion<sup>21</sup> is similar to Eq. (II-1), except that the time-scale of interest is the retarded time,  $t'$ :

$$m \frac{d\mathbf{v}}{dt'} = e\mathbf{E}_{i0} \cos[\mathbf{k}_i \cdot \mathbf{r}(t') - \omega_i t'] . \quad (\text{II-8})$$

The retarded time may be approximated by

$$t' = t - (|\mathbf{R} - \hat{\mathbf{n}} \cdot \mathbf{r}|/c) , \quad (\text{II-9})$$

where  $\mathbf{R}$  is the position of the observer with respect to the moving charge. If the influence of the EM wave on the translational motion of the electron is ignored, the scattered electric field is given by the field of a moving charge

$$\mathbf{E}_s(\mathbf{R},t) = \left( \frac{c}{cR} \right) [\hat{\mathbf{n}} \times (\hat{\mathbf{n}} \times \frac{d\beta}{dt'})]_{\text{ret}} \quad (\text{II-10})$$

with  $\beta \equiv (\hat{\mathbf{n}} \cdot \mathbf{v})/c$ , and its derivative is evaluated at the retarded time. Equations (II-8) and (II-9) are used to evaluate the scattered field in terms of the real time:

$$\mathbf{E}_s(\mathbf{R},t) = \frac{r_0^2}{R} [\hat{\mathbf{n}} \times (\hat{\mathbf{n}} \times \mathbf{E}_{i0})] \cos[k_s R - \omega_s t - \mathbf{k} \cdot \mathbf{r}(0)] \quad (\text{II-11})$$

The wave propagates at the Doppler-shifted frequency

$$\omega_s = \omega_i + \omega = \omega_i + \mathbf{k} \cdot \mathbf{v} \quad (\text{II-12})$$

with the wave vectors

$$\mathbf{k} = \mathbf{k}_s - \mathbf{k}_i, \quad \mathbf{k}_s = (\omega_s/c) \hat{\mathbf{n}} \quad \text{and} \quad \mathbf{k}_i = (\omega_i/c) \hat{\mathbf{f}} \quad (\text{II-13})$$

The angular factor in Eq. (II-11) depends on the polarization of the incident wave. If the angle between  $\hat{\mathbf{n}}$  and  $\hat{\mathbf{f}}$  is defined as  $\theta$ , and  $\phi_0$  is the angle between the polarization vector of the incident wave and the plane containing  $\hat{\mathbf{n}}$  and  $\hat{\mathbf{f}}$ , the angular factor takes on the simple form:

$$[\hat{\mathbf{n}} \times (\hat{\mathbf{n}} \times \hat{\mathbf{f}})]^2 = 1 - \sin^2 \theta \cos^2 \phi_0 \quad (\text{II-14a})$$

for polarized radiation, and

$$[\hat{\mathbf{n}} \times (\hat{\mathbf{n}} \times \hat{\mathbf{f}})]^2 = 1 - \frac{1}{2} \sin^2 \theta \quad (\text{II-14b})$$

for unpolarized radiation.

The total Doppler shift has two sources.<sup>22</sup> The first is that the incident wave has a Doppler-shifted frequency, as seen by the moving electron. The second shift is from the component of the electron velocity in the direction of the scattering. Equating the Doppler-shifted frequencies and then rearranging, recovers Eq. (II-12):

$$\omega_s = \omega_i \left( 1 - \frac{\hat{\mathbf{f}} \cdot \mathbf{v}}{c} \right) \left( 1 - \frac{\hat{\mathbf{n}} \cdot \mathbf{v}}{c} \right)^{-1} = \omega_i + \mathbf{k} \cdot \mathbf{v} \quad (\text{II-15})$$

The quantity of interest for any real experiment is the scattered power into some solid angle  $d\Omega$  at a frequency  $\omega_s$ :

$$\frac{dP_s(\mathbf{R}, \omega_s)}{d\Omega} = R^2 \left( \frac{c}{4\pi} \right) E_s^2 . \quad (\text{II-16})$$

Substituting the expression for the scattered electric field obtained in Eq. (II-11) into this equation yields the power scattered by a single electron

$$P_s(\mathbf{R}, \omega_s) d\Omega = \frac{c^2 r_0^2}{8\pi} E_{i0}^2 d\Omega [\hat{n} \times (\hat{n} \times \hat{f})]^2 . \quad (\text{II-17})$$

The electron radiates at the Doppler-shifted frequency,  $\omega_s$ , given by Eq. (II-12), which reflects the electron velocity. The electron velocity distribution may be determined from this equation. Since the scattered frequency is given [Eq. (II-12)] in terms of the electron velocity component ( $v_k$ ) in the direction of the differential scattering vector ( $\mathbf{k}$ ), the scattered intensity in a given frequency range about  $\omega_s$  is proportional to the number of electrons in a corresponding velocity range about  $v_k$ .<sup>23</sup>

Because the ions are much more massive than the electrons, they scatter much less. Therefore, the time-averaged power scattered per unit solid angle at the observer from an incident EM wave is a superposition of the scattered electric fields from each electron. This is equivalent to integrating the scattered field from each electron over the electron velocity distribution<sup>23</sup>:

$$\frac{dP_s}{d\Omega} = \frac{cR^2}{4\pi} \left( \sum_{j=1}^N \mathbf{E}_{js} \sum_{l=1}^N \mathbf{E}_{ls} \right) , \quad (\text{II-18})$$

which may be rearranged by separating out the terms where  $j=l$  ( $N$  is the total number of electrons), yielding

$$\frac{dP_s}{d\Omega} = \frac{cR^2}{8\pi} N E_s^2 + \frac{cR^2}{4\pi} N(N-1) \overline{(\mathbf{E}_j \cdot \mathbf{E}_{j \neq l})} . \quad (\text{II-19})$$

The first term represents incoherent scattering which is the simple sum of scattering from uncorrelated electrons. The second term is coherent scattering from correlated groups of electrons. The electrons may be correlated by being a part of a Debye shielding cloud, by some collective motion such as electron density fluctuations produced by a parametric instability, or some other process. The size of a typical electron feature is of the order of the Debye length. At the quarter-critical density surface of a 527-nm-laser-produced plasma with a temperature of 1 keV, the Debye length is approximately 7 nm.

It is useful to introduce the scattering parameter  $\alpha$ ,

$$\alpha \equiv \frac{1}{k\lambda_D} = \frac{1.08 \times 10^{-4} \lambda_i(\text{cm})}{\sin(\theta/2)} \left[ \frac{n_e(\text{cm}^{-3})}{T_e(\text{eV})} \right]^{1/2}, \quad (\text{II-20})$$

where  $k = 2\pi \sin(\theta/2)/\lambda_i$  and  $\lambda_D = (KT/4\pi en)^{1/2}$  is the Debye wavelength. When  $\alpha$  is small, that is,  $\lambda_i \ll \lambda_D$ , the EM wave incoherently scatters from the individual electrons because the incident wavelength is smaller than the dimensions of a typical electron feature (of the order of the size of a Debye sphere). In this case, the second term of Eq. (II-19) is zero and the scattered light spectrum gives the electron distribution. When  $\alpha$  is large, the second term of Eq. (II-19) dominates the distribution of the scattered power because the incident wavelength is larger than a Debye length so that the scattering is from "coarser-grained" features and the scattered light spectrum will reflect this.

The density of a laser-produced plasma is high enough that the scattering parameter is always larger than one for any commercially available laser. Thus, the calculation of the scattered power from a plasma must include the effects of collective motions. That is, the EM wave scatters from shielding clouds of electrons, rather than

from individual electrons. Each particle in a plasma may be considered as a test particle moving with velocity  $\mathbf{v}'$ , shielded by a cloud of oppositely charged particles, and also as a part of the shielding clouds around other test particles. It is helpful here to note that the electron density at  $(\mathbf{x}, t)$  in the vicinity of a test charge, at position  $\mathbf{x}'$ , is<sup>24</sup>

$$n_e(\mathbf{x}, t; \mathbf{x}', \mathbf{v}') = \bar{n}_e + \bar{n}_e \frac{4\pi e^2}{m} \lim_{\epsilon \rightarrow 0} \int \frac{\exp [i\mathbf{k} \cdot (\mathbf{x} - \mathbf{x}')] \mathbf{k} \cdot \nabla_{\mathbf{v}'} f_{\alpha 0}}{k^2 D(\mathbf{k}, \mathbf{k} \cdot \mathbf{v}') (\mathbf{k} \cdot \mathbf{v} - \mathbf{k} \cdot \mathbf{v}' - i\epsilon)} \times \frac{d\mathbf{k}}{(2\pi)^3} dv + \int \exp [i\mathbf{k} \cdot (\mathbf{x} - \mathbf{x}')] \frac{d\mathbf{k}}{(2\pi)^3}, \quad (\text{II-21})$$

with

$$D(\mathbf{k}, \mathbf{k} \cdot \mathbf{v}') = 1 - \sum_{\alpha} \frac{\omega_{p\alpha}^2}{k^2} \lim_{\epsilon \rightarrow 0} \left[ \int \frac{2\mathbf{k} \cdot \mathbf{v} (\partial f_{\alpha 0} / \partial v^2) dv}{\mathbf{k} \cdot \mathbf{v} - \mathbf{k} \cdot \mathbf{v}' - i\epsilon} \right]. \quad (\text{II-22})$$

The total scattered electric field is the ensemble average of the field scattered by one electron [Eq. (II-17)]:

$$\mathbf{E}_{s, \text{tot}}(\mathbf{R}, t) = -\frac{c}{cR} \int_V d\mathbf{r} \int d\mathbf{v} F_e(\mathbf{r}, \mathbf{v}, t') \left[ \frac{\hat{\mathbf{n}} \times \{(\hat{\mathbf{n}} - \boldsymbol{\beta}) \times \boldsymbol{\beta}\}}{(1 - \hat{\mathbf{n}} \cdot \boldsymbol{\beta})^3} \right]_{\mathbf{R}}. \quad (\text{II-23})$$

where  $\int d\mathbf{v} F_e = n(\mathbf{x}, t)$  is the average electron density. The time-averaged scattered power is then the sum over all test particles in the plasma,

$$P_s(\mathbf{R}) d\Omega = \frac{cR^2}{4\pi} d\Omega \lim_{T \rightarrow \infty} \frac{1}{T} \int_{-\infty}^{+\infty} dt |\mathbf{E}_{s, \text{tot}}|^2. \quad (\text{II-24})$$

The quantity measured in an experiment is the power scattered in some frequency range  $\omega_s \pm d\omega_s/2$ , since any detector accepts radiation only over a finite range. Therefore, the scattered power must be expressed in terms of frequency. To achieve this, the Fourier transform of the electric field is defined as

$$E_{s, \text{tot}}(\omega_s) = \int_{-\infty}^{+\infty} dt E_{s, \text{tot}}(t) \exp \{ -i\omega_s t \} . \quad (\text{II-25})$$

The application of Parseval's theorem results in an expression for the scattered power per unit frequency

$$P_s(\mathbf{R}, \omega_s) d\Omega d\omega_s = \frac{cR^2 d\Omega}{4\pi} \lim_{T \rightarrow \infty} \frac{1}{\pi T} \int_{\omega_s - d\omega_s/2}^{\omega_s + d\omega_s/2} d\omega_s \left| \int_{-\infty}^{+\infty} dt E_{s, \text{tot}}(t) e^{-i\omega_s t} \right|^2 . \quad (\text{II-26})$$

Recalling that  $E_{s, \text{tot}}$  is proportional to the number of scatterers, Eq. (II-26) shows that the scattered power is proportional to the square of the total number of scatterers, or, equivalently, the square of the density of the plasma.

Taking the spatial and temporal Fourier transforms of the density and substituting into Eq. (II-26) yields an expression for the scattered power,

$$P_s(\mathbf{R}, \omega_s) d\Omega d\omega_s = \frac{c d\Omega}{4\pi} \lim_{T \rightarrow \infty} \frac{d\omega_s}{\pi T} \left| \int_{-\infty}^{+\infty} dt \frac{e^2}{mc^2} E_i \left[ \hat{\mathbf{n}} \times (\hat{\mathbf{n}} \times \hat{\mathbf{f}}) \right] \right. \\ \left. \times \int_V dr n_e(r, t) \exp \left[ -i\omega_s \left( t - \frac{\hat{\mathbf{n}} \cdot \mathbf{r}}{c} + \frac{R}{c} \right) \right] \cos(\mathbf{k}_i \cdot \mathbf{r} - \omega_i t) \right|^2 . \quad (\text{II-27})$$

After substituting the Fourier transform of the electron density and then performing the integrals over wave vectors, time, and position, the scattered power can be written in terms of the ensemble average of the density fluctuations,

$$P_s(\mathbf{R}, \omega_s) d\Omega d\omega_s = \frac{cE_{i0}^2 r_0^2}{16\pi^2} d\Omega d\omega_s \left| \hat{\mathbf{n}} \times (\hat{\mathbf{n}} \times \hat{\mathbf{f}}) \right|^2 N S(\mathbf{k}, \omega) , \quad (\text{II-28})$$

with

$$S(\mathbf{k}, \omega) \equiv \lim_{T, V \rightarrow \infty} \frac{1}{TV} \left\langle \frac{|\ln_{e0}(\mathbf{k}, \omega)|^2}{n_{e0}} \right\rangle \quad (\text{II-29})$$



identified as the spectral density function. The curly braces denote an ensemble average. Examination of Eq. (II-28) shows that all of the spectral information is contained in the spectral density function. By measuring the frequency spectrum at a given scattering angle, or the wave-vector spectrum at a given frequency, information on the size and frequency of electron density fluctuations can be obtained.

The spectral density function has been calculated<sup>15</sup> in terms of  $G_e$  and  $G_i$ , the dielectric susceptibilities of the electrons and ions, respectively, and the zero-order velocity distributions  $f_{e0}(\omega/k)$  and  $f_{i0}(\omega/k)$ . It is

$$S(k, \omega) = \frac{2\pi}{k} \left| 1 - \frac{G_e}{\epsilon} \right|^2 f_{e0}(\omega/k) + \frac{2\pi Z}{k} \left| \frac{G_e}{\epsilon} \right|^2 f_{i0}(\omega/k) , \quad (\text{II-30})$$

with  $\epsilon = 1 + G_e + G_i$ .

If the zero-order electron- and ion-velocity distributions are Maxwellian with characteristic thermal velocities  $v_e$  and  $v_i$ , defined as  $v_a \equiv (2k_B T_e/m_a)^{1/2}$ , the susceptibilities take the simple form<sup>15</sup>

$$G_e = -\alpha^2 W(x_e) \quad (\text{II-31a})$$

$$G_i = -Z \left( \frac{T_e}{T_i} \right) \alpha^2 W(x_i) \quad (\text{II-31b})$$

where the dimensionless frequency variables are  $x_e = \omega/kv_e$ ,  $x_i = \omega/kv_i$ , and  $\alpha$  retains its earlier definition. The plasma dispersion function is  $W(x)$ :

$$W(x) = 1 - 2xe^{-x^2} \int_0^x e^{p^2} dp - i\pi^{1/2} xe^{-x^2} , \quad (\text{II-32})$$

and the real and imaginary parts of  $W(x)$  are denoted by  $Rw(x)$  and  $Iw(x)$ , respectively. The function  $Iw(x)$  represents Landau damping. The spectral density function is easily calculated to be<sup>25</sup>

$$S(\mathbf{k}, \omega) = \frac{2\sqrt{\pi}}{kv_e} \left[ \frac{A_e + A_i}{|\mathbf{k}|^2} \right], \quad (\text{II-33})$$

where

$$A_e = \exp(-x_e^2) \left[ \left( 1 + \alpha^2 Z \frac{T_e}{T_i} R w(x_e) \right)^2 + \left( \alpha^2 Z \frac{T_e}{T_i} I w(x_e) \right)^2 \right] \quad (\text{II-34a})$$

$$A_i = Z \left( \frac{m_i T_e}{m_e T_i} \right)^{1/2} \exp(-x_i^2) \left[ (\alpha^2 R w(x_e))^2 + (\alpha^2 I w(x_e))^2 \right] \quad (\text{II-34b})$$

and

$$|\mathbf{k}|^2 = \left[ 1 + \alpha^2 \left( R w(x_e) + Z \frac{T_e}{T_i} R w(x_e) \right) \right]^2 + \left[ \alpha^2 I w(x_e) + \alpha^2 Z \frac{T_e}{T_i} I w(x_e) \right]^2. \quad (\text{II-35})$$

An interesting approximation is due to Salpeter.<sup>26</sup> When  $T_e \approx T_i$ , the quantity  $x_e/x_i \ll 1$ . The spectral density function is now greatly simplified to

$$S(\mathbf{k}, \omega) = \frac{2\pi^{1/2}}{kv_e} \Gamma_\alpha(x_e) + \frac{2\pi^{1/2}}{kv_i} Z \left( \frac{\alpha^2}{1 + \alpha^2} \right)^2 \Gamma_\beta(x_e), \quad (\text{II-36})$$

where

$$\Gamma_\rho(x) = \frac{\exp(-x^2)}{[1 + \rho^2 R w(x)]^2 + [\rho^2 I w(x)]^2} \quad (\text{II-37a})$$

$$\beta^2 = \frac{Z\alpha^2 T_e}{1 + \alpha^2 T_i}. \quad (\text{II-37b})$$

This approximation shows many of the features that are important in a plasma with a Maxwellian distribution. For small values of the scattering parameter,  $\alpha$ , the scattered frequency is proportional to the electron velocity distribution in the direction of  $\mathbf{k}$ , the differential scattering vector. More importantly, when  $\alpha$  is large, two "plasma-line"

features appear at frequencies  $\omega_s$  where the denominator of  $\Gamma$  is a minimum. These frequencies are shifted from the incident EM frequency by the Bohm-Gross frequency,  $\omega_{BG}$ ,

$$\omega_s = \omega_i \pm \omega_{BG} \quad (\text{II-38a})$$

$$\omega_{BG}^2 = \omega_{pe}^2 + 3v_T^2 k^2 . \quad (\text{II-38b})$$

An example of the electron feature spectrum is shown in Figure II-1.

As shall be shown in the rest of this chapter, enhancements of the level of scattering of the plasma-line feature may occur for electron distributions that deviate from Maxwellian.

## B. Scattering from Non-Equilibrium Plasmas

Non-Maxwellian electron distributions give rise to greatly enhanced scattering levels of the "plasma-line" feature. This effect was first observed in ionospheric experiments conducted at Arecibo<sup>27</sup> and explained by Perkins and Salpeter.<sup>14</sup> The principal result of their work, the power spectrum near the plasma line including the effects of electron-ion collisions, will be generalized in the next section to the conditions of laser-produced plasmas following Simon's derivation.

This section begins with the derivation of the power spectrum near the plasma line in a *collisionless* plasma. This result does not show all of the features of the collisional case, but is much easier to derive.

The derivation and notation of Perkins and Salpeter<sup>14</sup> will be followed closely. The following assumptions are made: (1) the plasma is uniform and consists of  $N$  electrons and  $N/Z$  ions of charge  $Z$ ; (2) the plasma fills a volume  $V$  so that the electron density is  $n = N/V$ ; and (3) the ions are motionless. This last assumption is valid

## Salpeter Spectral-Density Function

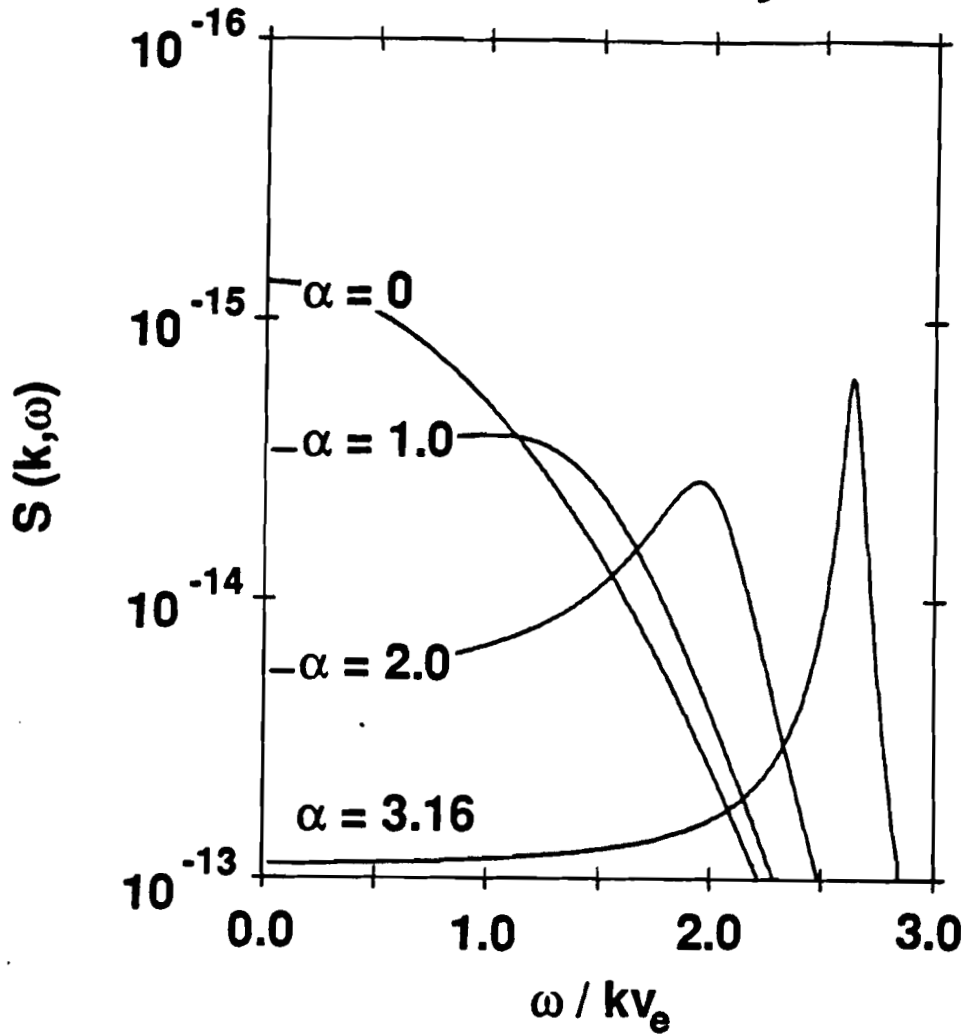


Figure II-1. The Salpeter approximation to the spectral density function as a function of the scattering parameter,  $\alpha$ , for electron and ion temperatures equal to 1500 eV.

because the ion thermal velocities are much smaller than the electron velocities. An expression for the power spectrum near the plasma line will be derived by assuming that the electron distribution function, which satisfies the Vlasov equation, consists of three terms representing the average velocity distribution, ion effects, and time-dependent fluctuations from the time-averaged distribution, respectively. The first two terms are considered known and used to solve for the level of the fluctuations whose Fourier transform is related to the power spectrum. The two important physical effects for the collisionless case are the excitation of plasma waves by fast electrons whose phase velocity is in resonance with the electron distribution at the Bohm-Gross frequency and the broadening of these resonance regions by Landau damping.

The electron distribution is described by the function

$$F(\mathbf{x}, \mathbf{v}, t) = F_0(\mathbf{v}) + F_1(\mathbf{x}, \mathbf{v}) + f(\mathbf{x}, \mathbf{v}, t) \quad (\text{II-39})$$

where  $F_0$  is a zero-order isotropic distribution normalized to 1,  $F_1$  is the first-order time-independent distribution, and  $f$  is the first-order time-dependent distribution that is responsible for the enhancement of the plasma lines. The first-order potential,  $\Phi_1$ , is produced by  $F_1$ . The zero-order potential, due to  $F_0$ , is zero. The complete distribution function,  $F$ , satisfies the Vlasov equation and Poisson's equation:

$$\frac{\partial F}{\partial t} + \mathbf{v} \cdot \frac{\partial F}{\partial \mathbf{x}} + \frac{e}{m} \nabla \Phi \cdot \frac{\partial F}{\partial \mathbf{v}} = 0, \quad (\text{II-40})$$

$$\nabla^2 \Phi = 4\pi e \left[ n \int F d\mathbf{v} - Z \sum_{j=1}^{NZ} \delta(\mathbf{x} - \mathbf{R}_j) \right]. \quad (\text{II-41})$$

The total electrostatic potential is  $\Phi$  and  $\mathbf{R}_j$  is the position of the  $j$ th ion. Since the zero-order part of the potential is zero, the quantity  $\Phi$  is first-order and consists of a time-dependent term from  $f$ , and a time-independent term,  $\Phi_1$ .

The method of solution for Eqs. (II-40) and (II-41) is to take the

Fourier-Laplace transform and then linearize the result by keeping only those terms that are first order in  $f$  or  $Q$ , where  $Q$  is the Fourier-Laplace transform of the electron density:

$$Q(\mathbf{k}, \omega) = \sum_{i=1}^N \int_0^{\infty} dt \exp \{ -i\mathbf{k} \cdot \mathbf{x}_i(t) + (i\omega - \gamma)t \} , \quad (\text{II-42})$$

the summation is over all electrons, and  $\gamma$  is a small positive number. The transform of the time-dependent distribution,  $f$ ,

$$f(\mathbf{k}, \mathbf{v}, \omega) = \int_{-\infty}^{+\infty} d\mathbf{x} \int_0^{\infty} dt f(\mathbf{x}, \mathbf{v}, t) \exp \{ -i\mathbf{k} \cdot \mathbf{x} + (i\omega - \gamma)t \} , \quad (\text{II-43})$$

is related to  $Q$  (for nonzero  $\omega$ ) by

$$Q(\mathbf{k}, \omega) = n \int d\mathbf{v} f(\mathbf{k}, \mathbf{v}, \omega) . \quad (\text{II-44})$$

By taking the Fourier-Laplace transform of Eq. (II-38), the electrostatic potential can be expressed in terms of  $Q$ :

$$\frac{-4\pi e}{k^2} Q(\mathbf{k}, \omega) = \int d\mathbf{x} \int_0^{\infty} dt \Phi \exp \{ -i\mathbf{k} \cdot \mathbf{x} + (i\omega - \gamma)t \} . \quad (\text{II-45})$$

The contribution to  $Q$  comes only from the potential due to  $f$  since  $\Phi_1$  is independent of time.

The linearized transform of the time-dependent part of Eq. (II-40) is

$$\begin{aligned} & (\gamma + i\mathbf{k} \cdot \mathbf{v} - i\omega) f(\mathbf{k}, \mathbf{v}, \omega) - i \left( \frac{\omega_p^2}{nk^2} \right) Q(\mathbf{k}, \omega) \mathbf{k} \cdot \frac{\partial F_0}{\partial \mathbf{v}} \\ & - i \left( \frac{\omega_p^2}{nV} \right) \sum_{\mathbf{q}} \left\{ \frac{Q(\mathbf{q}, \omega)}{q^2} \mathbf{q} \cdot \frac{\partial F_1(\mathbf{k} - \mathbf{q}, \mathbf{v})}{\partial \mathbf{v}} \right. \end{aligned}$$

$$\left. -\frac{\Phi_1(\mathbf{k}-\mathbf{q})}{4\pi e} (\mathbf{k}-\mathbf{q}) \cdot \frac{\partial f(\mathbf{q},\mathbf{v},\omega)}{\partial \mathbf{v}} \right\} = f(\mathbf{k},\mathbf{v},t=0) . \quad (\text{II-46})$$

The sum over  $\mathbf{q}$  contains all the terms bilinear in the first-order parameters  $f$  and  $\Phi_1$ , or  $Q$  and  $F_1$ , which represent the electron-ion collisions. These terms represent the three-wave excitation of an electron density fluctuation ( $\mathbf{q}$ ) by an electron density fluctuation ( $\mathbf{k}$ ) interacting with the static electron-ion correlations ( $\mathbf{q}-\mathbf{k}$ ). These terms will be important when the collisional case is considered, but neglecting these terms yields a collisionless equation:

$$(\gamma + i\mathbf{k} \cdot \mathbf{v} - i\omega) f(\mathbf{k},\mathbf{v},\omega) - i \frac{\omega_p^2}{nk^2} Q(\mathbf{k},\omega) \mathbf{k} \cdot \frac{\partial F_0}{\partial \mathbf{v}} = f(\mathbf{k},\mathbf{v},0) . \quad (\text{II-47})$$

Let  $\eta(\mathbf{k},\mathbf{v},\omega)$  and  $\psi(\mathbf{k},\omega)$  be the collisionless approximations of  $f$  and  $Q$ , respectively.

Then

$$\eta(\mathbf{k},\mathbf{v},\omega) = \frac{-if(\mathbf{k},\mathbf{v},0) + (\omega_p^2/nk^2) \psi(\mathbf{k},\omega) \mathbf{k} \cdot \partial F_0 / \partial \mathbf{v}}{\mathbf{k} \cdot \mathbf{v} - \omega - i\gamma} . \quad (\text{II-48})$$

Multiplying by the density  $n$ , integrating over velocity space, and using Eq. (II-43), yields the solution for  $\psi$ :

$$\psi(\mathbf{k},\omega) = \left( \frac{-in}{\epsilon_0(\mathbf{k},\omega)} \right) \int \frac{f(\mathbf{k},\mathbf{v},0) d\mathbf{v}}{\mathbf{k} \cdot \mathbf{v} - \omega - i\gamma} , \quad (\text{II-49})$$

with the definition

$$\epsilon_0(\mathbf{k},\omega) = 1 - \frac{\omega_p^2}{k^2} \int \frac{\mathbf{k} \cdot \partial F_0 / \partial \mathbf{v} d\mathbf{v}}{\mathbf{k} \cdot \mathbf{v} - \omega - i\gamma} . \quad (\text{II-50})$$

The integral in Eq. (II-49) consists of a sum over  $N$  terms, since

$$f(\mathbf{k},\mathbf{v},t=0) = \frac{1}{n} \sum_i \exp(-i\mathbf{k} \cdot \mathbf{x}_i) \delta(\mathbf{v} - \mathbf{v}_i) , \quad (\text{II-51})$$

where  $\mathbf{x}_i$  and  $\mathbf{v}_i$  are the initial position and velocity of the  $i$ th electron.

The power spectrum is given by

$$I(\omega) = \lim_{\gamma \rightarrow 0} \left( \frac{\gamma}{\pi N} \right) |Q(\mathbf{k}, \omega)|^2, \quad (\text{II-52})$$

and the approximation,  $\psi$ , is substituted for  $Q$ . Substituting Eqs. (II-49) and (II-51) into Eq. (II-52) yields

$$I(\mathbf{k}, \omega) = \lim_{\gamma \rightarrow 0} \left( \frac{\gamma}{\pi N} \right) |\epsilon_0(\mathbf{k}, \omega)|^2 \times \sum_{ij} \frac{\exp\{-i\mathbf{k} \cdot (\mathbf{x}_i - \mathbf{x}_j)\}}{(\mathbf{k} \cdot \mathbf{v}_i - \omega - i\gamma)(\mathbf{k} \cdot \mathbf{v}_j - \omega + i\gamma)}. \quad (\text{II-53})$$

The double sum can be evaluated by separating out the terms where  $i = j$ , to obtain

$$\sum_{ij} = \lim_{\gamma \rightarrow 0} \frac{\gamma}{\pi N} \left\{ \int_{-\infty}^{+\infty} \frac{F_0(\mathbf{v}) d\mathbf{v}}{(\mathbf{k} \cdot \mathbf{v} - \omega)^2 + \gamma^2} + (N-1) \iint \frac{F_0(\mathbf{v}_i) F_0(\mathbf{v}_j) \langle \exp\{i\mathbf{k} \cdot (\mathbf{x}_i - \mathbf{x}_j)\} \rangle}{(\mathbf{k} \cdot \mathbf{v}_i - \omega - i\gamma)(\mathbf{k} \cdot \mathbf{v}_j - \omega - i\gamma)} d\mathbf{v}_i d\mathbf{v}_j \right\}. \quad (\text{II-54})$$

The quantity  $\langle \rangle$  indicates an average over the positions of the two electrons with their velocities kept constant. At resonance,  $\omega = \mathbf{k} \cdot \mathbf{v}$ , and as  $\gamma \rightarrow 0$ , the first term of Eq. (II-54) is of order  $\gamma^{-1}$  (a large value), while the second term tends to a constant limit because the denominator can only be in resonance at one phase velocity.<sup>26</sup> Clearly, the second term may be neglected so that only the terms where  $i = j$  survive the limit. The power spectrum then reduces to

$$I(\mathbf{k}, \omega) = k^{-1} F_0^{(1)}(\omega/k) |\epsilon_0(\mathbf{k}, \omega)|^2, \quad (\text{II-55})$$

where the term,  $F_0^{(1)}(u)$ , is defined as a one-dimensional velocity distribution:



$$F_0^{(1)}(u) \equiv \int_{|u|}^{\infty} F_0(v) 2\pi v dv . \quad (\text{II-56})$$

An approximation to the collisionless dielectric function [Eq. (II-50)] can be made since the phase velocity,  $v_\phi = \omega/k$ , satisfies  $v_\phi \ll \omega_p/k$  for all values of interest,<sup>28</sup>

$$\epsilon_0(k, \omega) = 1 - \frac{\omega_p^2}{\omega^2} \left[ 1 + \frac{3k^2 k_B \bar{T}}{m\omega^2} \right] + i\pi \frac{\omega_p^2}{k^2} \frac{dF_0^{(1)}(\omega/k)}{d(\omega/k)} . \quad (\text{II-57})$$

The average temperature,  $\bar{T}$ , is defined by

$$3k_B \bar{T} = \int mv^2 F_0(v) dv . \quad (\text{II-58})$$

Large enhancements of the power spectrum (the "plasma lines") occur at frequencies where the real part of  $\epsilon_0$  vanishes. Denoting these frequencies as  $\omega_{BG}$ , the enhancements occur at

$$\omega = \pm \omega_{BG} = \pm (\omega_p^2 + 3k^2 k_B \bar{T} / m)^{1/2} . \quad (\text{II-59})$$

Near these frequencies, the power spectrum has the form

$$I(k, \omega) = \frac{\omega_{BG}^2 F_0^{(1)}(\omega_{BG}/k)}{4k \left\{ (\omega - \omega_{BG})^2 + \left[ \frac{\pi \omega_{BG} \omega_p^2}{2 k^2} \left( \frac{dF_0^{(1)}(u)}{du} \right)_{u = \omega/k} \right]^2 \right\}} . \quad (\text{II-60})$$

The second term of the denominator of Eq. (II-60) is very small, showing the resonant nature of the power spectrum when  $\omega \approx \omega_{BG} \approx \omega_p$  and that the line has a Lorentzian shape. The width of this plasma line is determined by the Landau damping term.

The goal of the rest of this section is to derive an expression for the power spectrum near the plasma line including electron-ion collisions, which will give the correct width of the plasma lines. The natural approach to this problem is to use a

Fokker-Planck equation that correctly models the electron-ion collisions. The collision term, or drag on the particle, represents the loss of energy due to a large number of small angle deflections. By using a Green's function to represent a test particle traveling through the plasma to solve the Fokker-Planck equation, the electron-density term will be seen to contain terms that describe the excitation of plasma waves by random collisions. That same Green's function will also describe the damping of those waves. Finally, the power spectrum will be derived.

The starting point is to derive the Fokker-Planck equation for  $f(\mathbf{k}, \mathbf{v}, \omega)$  without neglecting the collision terms by rewriting Eq. (II-46) to solve for  $f(\mathbf{q}, \mathbf{v}, \omega)$  in terms of  $f(\mathbf{k}, \mathbf{v}, \omega)$  and then substituting back into the original Eq. (II-46)<sup>14</sup>:

$$\begin{aligned} (\mathbf{k} \cdot \mathbf{v} - \omega - i\gamma) f(\mathbf{k}, \mathbf{v}, \omega) + i\nu(\mathbf{v}) \frac{\partial}{\partial v_\alpha} (v^2 \delta_{\alpha\beta} - v_\alpha v_\beta) \frac{\partial f(\mathbf{k}, \mathbf{v}, \omega)}{\partial v_\beta} \\ = S(\mathbf{k}, \mathbf{v}, \omega) + \frac{\omega_p^2}{nk^2} Q(\mathbf{k}, \omega) \mathbf{k} \cdot \frac{\partial F_0}{\partial \mathbf{v}} , \end{aligned} \quad (\text{II-61})$$

where the source term representing electron-ion collisions is

$$\begin{aligned} S(\mathbf{k}, \mathbf{v}, \omega) = -i f(\mathbf{k}, \mathbf{v}, 0) + \frac{\omega_p^2}{k^2 nV} \sum_{\mathbf{q}} \Phi_1(\mathbf{q} - \mathbf{k}) \\ \times \{ [e\psi(\mathbf{k}, \omega)/k_B \langle \zeta \rangle] \mathbf{k} \cdot [\partial \Psi(\mathbf{v})/\partial \mathbf{v}] \\ - (k^2/4\pi e) (\mathbf{k} - \mathbf{q}) \cdot [\partial \eta(\mathbf{k}, \mathbf{v}, \omega)/\partial \mathbf{v}] \} . \end{aligned} \quad (\text{II-62})$$

Several definitions have been made here,

$$\Psi(\mathbf{v}) \equiv \langle \zeta \rangle \xi^{-1}(\mathbf{v}) F_0(\mathbf{v}) , \quad (\text{II-63})$$

$$\langle \zeta \rangle^{-1} \equiv \int F_0(\mathbf{v}) \xi^{-1}(\mathbf{v}) d\mathbf{v} , \quad \frac{m\mathbf{v}}{k_B \xi(\mathbf{v})} = -\frac{d}{d\mathbf{v}} \ln F_0(\mathbf{v}) , \quad (\text{II-64})$$

and the collisional terms are

$$v(v) = \frac{Z\omega_p^2 \ln \Lambda}{8\pi n v^3} ; \quad \bar{v} = \int \frac{v(v) m v_z^2}{k_B \xi(v)} F_0(v) dv . \quad (\text{II-65})$$

In the above,  $\Psi$  is a modification of the zero-order distribution function,  $v$  is the collision frequency,  $\bar{v}$  is an average collision frequency, and  $\Lambda \equiv 4\pi n \lambda_D^3$ . If  $F_0$  is a Maxwellian, the term  $\xi(v)$  is independent of the velocity and is equal to the temperature of the Maxwellian. Consequently,  $\langle \zeta \rangle = \xi = T$ , and  $\Psi = F_0$ . Because the distribution  $F_1$  is independent of time, its contribution to the scattered spectrum is a delta function at zero frequency. This represents the effects of the ions which were assumed to be fixed. This term shall be neglected because the light is mostly scattered by the shielding electrons. The indirect effects of  $F_1$  in Eq. (II-46) will be retained, however.

A Green's function will be used to solve Eq. (II-61). The Green's function satisfies

$$\left[ \mathbf{k} \cdot \mathbf{v} - \omega - i\gamma + iv(v) \frac{\partial}{\partial v_\alpha} (v^2 \delta_{\alpha\beta} - v_\alpha v_\beta) \frac{\partial}{\partial v_\beta} \right] G(\mathbf{k}, \mathbf{v}, \mathbf{v}', \omega) = -i \delta(\mathbf{v} - \mathbf{v}') , \quad (\text{II-66})$$

and describes the propagation of a test electron through a plasma of fixed discrete ions shielded by the static electron shielding clouds. Using this definition,  $f(\mathbf{k}, \mathbf{v}, \omega)$  may be written as

$$f(\mathbf{k}, \mathbf{v}, \omega) = i \int d\mathbf{v}' G(\mathbf{k}, \mathbf{v}, \mathbf{v}', \omega) \times \left\{ S(\mathbf{k}, \mathbf{v}', \omega) + \frac{\omega_p^2}{k^2 n} Q(\mathbf{k}, \omega) \mathbf{k} \cdot \frac{\partial F_0}{\partial \mathbf{v}'} \right\} . \quad (\text{II-67})$$

The quantity  $Q$  and the dielectric function are expressed in terms of the velocity integral of  $G$ ,

$$H(\mathbf{k}, \mathbf{v}', \omega) = \int d\mathbf{v} G(\mathbf{k}, \mathbf{v}, \mathbf{v}', \omega) , \quad (\text{II-68})$$

as

$$Q(\mathbf{k}, \omega) = \frac{i n}{\epsilon(\mathbf{k}, \omega)} \int d\mathbf{v}' H(\mathbf{k}, \mathbf{v}', \omega) S(\mathbf{k}, \mathbf{v}', \omega) , \quad (\text{II-69})$$

and

$$\epsilon(\mathbf{k}, \omega) = 1 - \frac{i \omega_p^2}{k^2} \int d\mathbf{v}' H(\mathbf{k}, \mathbf{v}', \omega) \mathbf{k} \cdot \frac{\partial F_0}{\partial \mathbf{v}'} . \quad (\text{II-70})$$

The denominator of Eq. (II-69) represents the damping of plasma waves while the numerator represents the excitation of those waves due to random collisions represented by  $S$ , the source term for fluctuations. Both of these terms require approximations of the function  $H$ . Since plasma waves are damped primarily by the randomization of the electrons by electron-ion collisions, the approximation in the denominator must be a function that slows down along the direction of motion and that reproduces the average position vector  $\langle \mathbf{x} \rangle$ . By inverting the Fourier-Laplace transform for  $G$ , Eq. (II-66), and using the correct initial condition,  $G(\mathbf{x}, \mathbf{v}, \mathbf{v}', 0) = \delta(\mathbf{x}) \delta(\mathbf{v} - \mathbf{v}')$ ,  $\langle \mathbf{x} \rangle$  may be calculated as

$$\langle \mathbf{x} \rangle = \int \mathbf{x} G d\mathbf{x} d\mathbf{v} = \mathbf{v}' (2v)^{-1} (1 - e^{-2vt}) . \quad (\text{II-71})$$

Representing  $G$  as a delta function in position and velocity space that reproduces  $\langle \mathbf{x} \rangle$  correctly will be an adequate approximation to use in the denominator of Eq. (II-69),

$$\begin{aligned} H(\mathbf{k}, \mathbf{v}', \omega) &\approx H^D(\mathbf{k}, \mathbf{v}', \omega) \\ &= \int_0^{\infty} \exp \{ (i\omega - \gamma)t - i\mathbf{k} \cdot \mathbf{v}' (2v)^{-1} (1 - e^{-2vt}) \} dt . \end{aligned} \quad (\text{II-72})$$

From the collisionless case, it is expected that the dielectric function will only be important for frequencies  $\omega \approx \omega_p$  and for scattering parameters  $\alpha \gg 1$ . In this limit,

$\epsilon(\mathbf{k}, \omega)$  becomes

$$\epsilon(\mathbf{k}, \omega) = 1 - \frac{\omega_p^2}{\omega^2} \left( 1 + \frac{3k^2 k_B \bar{T}}{m \omega^2} \right) - i \left\{ \frac{2\omega_p^2 \bar{v}}{\omega^3} - \frac{\pi\omega_p^2}{k^2} \left( \frac{\partial F_0^{(1)}}{\partial u} \right)_{u=\omega/k} \right\}. \quad (\text{II-73})$$

In the above,

$$\bar{T} = T, \quad \bar{v} = \omega_p Z \Lambda^{-1} \ln \Lambda (2\pi)^{1/2} / 6 \quad (\text{II-74})$$

because, according to Eqs. (II-58) and (II-65), these quantities depend mainly on particles of average energy so that the function  $F_0$  may be replaced by a Maxwellian in their calculation. The damping is now due to two effects: electron-ion collisions (via  $\bar{v}$ ) and Landau damping. The two damping terms are now stated explicitly. In the limit of zero collision frequency, Eq. (II-57) is recovered and  $\epsilon(\mathbf{k}, \omega)$  becomes  $\epsilon_0(\mathbf{k}, \omega)$ .

An approximation to the numerator may be obtained by considering a Fokker-Planck equation that describes sideways deflections correctly on a short time scale,  $v\tau \ll 1$ , which will correctly model the excitation of plasma waves. This approximate Fokker-Planck equation is the Fourier-Laplace transform of Eq. (II-65) with the variable tensor  $(v^2 \delta_{\alpha\beta} - v_\alpha v_\beta)$  replaced by a constant tensor  $(v^2 \delta_{\alpha\beta} - v'_\alpha v'_\beta)$ . This equation models sideways deflections correctly. The solution of this new equation is then used to calculate the approximation of  $H$  used in the numerator,  $H^N(\mathbf{k}, \mathbf{v}', \omega)$ . Only components of  $\partial H^N / \partial v'$  that are perpendicular to  $\mathbf{v}'$  will be needed and will be denoted by the subscript  $xy$ :

$$(\partial H^N / \partial v')_{xy} = -k_{xy} \int_0^\infty dt \left[ it - \frac{2}{3} v\tau^3 (\mathbf{k} \cdot \mathbf{v}') \right]$$

$$\times \exp\{(i\omega - i\mathbf{k} \cdot \mathbf{v}' - \gamma)t - \frac{1}{3}vt^3[\mathbf{v}'^2\mathbf{k}^2 - (\mathbf{k} \cdot \mathbf{v}')^2]\} . \quad (\text{II-75})$$

Finally, two simplifying approximations are made that allow a calculation of the numerator of Eq. (II-69). The first is that the limit  $\gamma \rightarrow 0$  represents an average over long times so that initial conditions, such as the term  $f(\mathbf{k}, \mathbf{v}, 0)$ , may be neglected. The second is that only terms that are logarithmically dominant sums over  $\mathbf{q}$  will be kept. In particular, only the largest term in the limit of large  $\mathbf{q}$  will be kept. This leads to an expression for the numerator of Eq. (II-69):

$$i n \int d\mathbf{v}' H^N(\mathbf{k}, \mathbf{v}', \omega) S(\mathbf{k}, \mathbf{v}', \omega) = \sum_i S^i(\mathbf{k}, \mathbf{x}_i, \mathbf{v}_i, \omega) , \quad (\text{II-76})$$

where

$$S^i = \left( \frac{-e}{mV} \right) \sum_{\mathbf{q}} \Phi_1(\mathbf{k} - \mathbf{q}) e^{-i\mathbf{q} \cdot \mathbf{x}_i} (\mathbf{q} \cdot \mathbf{v}_i - \omega - i\gamma)^{-1} (\mathbf{k} - \mathbf{q}) \cdot (\partial H^N(\mathbf{k}, \mathbf{v}_i, \omega) / \partial \mathbf{v}_i) . \quad (\text{II-77})$$

The power spectrum depends on the double sum

$$\sum_{ij} S^i (S^j)^* . \quad (\text{II-78})$$

This is really a quadruple sum when the sums over  $\mathbf{q}$  and  $\mathbf{q}'$  are considered. As before, only the  $i = j$  terms are logarithmically divergent, leaving the double sum over  $\mathbf{q}$  and  $\mathbf{q}'$ . Using the same reasoning, however, reduces the result to a sum over the  $\mathbf{q} = \mathbf{q}'$  terms. Therefore, the power spectrum is proportional to

$$\lim_{\gamma \rightarrow 0} \left( \frac{\gamma}{\pi N} \right) \left[ \sum_{ij} S^i (S^j)^* \right] = \lim_{\gamma \rightarrow 0} \frac{\gamma}{\pi} \int d\mathbf{v} F_0(\mathbf{v}) \left( \frac{\partial}{\partial v_\alpha} H^N \right) T_{\alpha\beta}(\mathbf{v}) \left( \frac{\partial}{\partial v_\beta} H^N \right) , \quad (\text{II-79})$$

where

$$T_{\alpha\beta}(\mathbf{v}) = \int \frac{d\mathbf{k} e^2 |\Phi_1(\mathbf{k})|^2 k_\alpha k_\beta}{(2\pi)^3 m^2 V [(\mathbf{q} \cdot \mathbf{v} + \mathbf{k} \cdot \mathbf{v} - \omega)^2 + \gamma^2]} . \quad (\text{II-80})$$

Only the elements of  $T_{\alpha\beta}$  perpendicular to  $\mathbf{v}$  are nonzero. These elements are equal to  $\mathbf{v}(\mathbf{v})v^2/\gamma$  if only the logarithmically dominant part of the integral is kept by cutting off the integration at  $k = k_B \langle \zeta \rangle / e^2$ . The sum then becomes,

$$\begin{aligned} \lim_{\gamma \rightarrow 0} \left( \frac{\gamma}{\pi N} \right) \left[ \sum_{ij} S^i (S^j)^* \right] \\ = \frac{1}{\pi} \int d\mathbf{v} F_0(\mathbf{v}) \left| \frac{\partial H^N}{\partial v} \right|_{xy}^2 \mathbf{v}(\mathbf{v}) v^2 \\ = \frac{k^2}{\pi \omega^4} \int d\mathbf{v} F_0(\mathbf{v}) (v_{xy})^2 \mathbf{v}(\mathbf{v}) + \frac{F_0^{(1)}(\omega/k)}{k} . \end{aligned} \quad (\text{II-81})$$

This last integral is

$$\int d\mathbf{v} F_0(\mathbf{v}) (v_{xy})^2 \mathbf{v}(\mathbf{v}) = 2\bar{v} k_B T / m , \quad (\text{II-82})$$

where  $F_0(\mathbf{v})$  has been replaced by a Maxwellian because this integral is not sensitive to the high energy tail.

The power spectrum may now be calculated by inserting Eqs. (II-73) and (II-82) into Eq. (II-53),

$$I(\mathbf{k}, \omega) = |\epsilon(\mathbf{k}, \omega)|^{-2} \{ 2\bar{v} k_B T m^{-1} + k^{-1} F_0^{(1)}(\omega/k) \} . \quad (\text{II-83})$$

This result is similar to that of the collisionless case of Eq. (II-55). The dielectric function,  $\epsilon$ , is given by Eq. (II-73) and has sharp resonances when  $\omega = \pm \omega_{BG}$ , just as in the collisionless case. Near these frequencies, the power spectrum has the form

$$I(k, \omega) = \frac{\omega_{BG}^2 \{F_0^{(1)}(\omega_{BG}/k) + 2k^3 k_B T \bar{v} / \pi m \omega_{BG}^4\}}{4k \left\{ (\omega - \omega_{BG})^2 + \frac{\omega_p^4}{\omega_{BG}^4} \left[ \bar{v} - \frac{\pi}{2} \frac{\omega_{BG}^3}{k^2} \left( \frac{\partial F_0^{(1)}}{\partial u} \right)_{u = \omega_{BG}/k} \right]^2 \right\}} \quad (\text{II-84})$$

In the limit of zero collision frequency, this reduces to the collisionless result, Eq. (II-60).

### C. Enhanced Thomson Scattering in a Laser-Produced Plasma

The main result of the previous section [Eq. (II-84)] can be generalized to predict the spectral location of scattered-light bands emanating from a laser-produced plasma.<sup>12,13,29</sup> The bands are the result of the interaction between the heating laser beam and density fluctuations whose amplitudes have been enhanced by the presence of fast or superfast electrons created by parametric instabilities or resonance absorption in the underdense corona. If no hot or superhot electrons are present, the density fluctuations still exist, but their amplitudes are not enhanced above the background thermal level. Incoming laser light will still Thomson scatter from the thermal plasma waves in the standard manner,<sup>17</sup> although much more weakly than in ETS.<sup>30</sup>

The electron-velocity distribution is not a simple Maxwellian in a laser-produced plasma and the zero-order velocity distribution used to determine the location of the scattering bands must reflect the nonisotropic nature of the electrons. In general, the distribution consists of three terms: a cold background at temperature  $T_c$ , a hot component caused by resonance absorption of the laser at the critical surface with temperature  $T_h$ , and a superhot component of temperature  $T_{sh}$  that may come from either the two plasmon decay instability or the absolute stimulated Raman scattering



instability. For example, it was found that under the conditions of the experiment described in Chapter III, a plasma produced by a 527-nm laser had a cold temperature of 1.5 keV, a hot temperature of between 5 and 10 keV, and a superhot temperature greater than 15 keV.<sup>31</sup> The plasma studied in Chapter IV, produced by 351-nm radiation, had a cold temperature of about 2.7 keV and a superhot temperature of 25 keV. No hot-electron temperature was observed or inferred.

The power spectrum [Eq. (II-84)] is restated here with a slight change of notation so as to follow Reference 13 more closely:

$$I(\mathbf{k}, \omega) = |\epsilon(\mathbf{k}, \omega)|^2 [2\nu k_B T_c (\pi m \omega^4)^{-1} + P_0] . \quad (\text{II-85})$$

The wave number and frequency of the plasma wave are given by  $\mathbf{k} = \mathbf{k}_0 - \mathbf{k}_s$  and  $\omega = \omega_0 - \omega_s$ , respectively. It is assumed that the bulk of the electrons can be described by a Maxwellian distribution with the cold background temperature  $T_c$ . The effective dielectric function, including collisions, is given by

$$\epsilon(\mathbf{k}, \omega) = 1 - \frac{\omega_p^2}{\omega^2} \left( 1 + \frac{3k^2 k_B T_c}{m \omega^2} \right) - i \left( \frac{2\omega^2 \bar{\nu}}{\omega^3} - \frac{\pi \omega_p^2}{k^2} P_0' \right) . \quad (\text{II-86})$$

The terms  $P_0$  and  $P_0'$  are integrals over the zero-order uniform isotropic electron distribution,  $F_0$ , [Eqs. (II-49) and (II-50)];

$$P_0 = \lim_{\gamma \rightarrow 0} \frac{\gamma}{\pi} \int \frac{F_0(\mathbf{v}) d\mathbf{v}}{[(\mathbf{k} \cdot \mathbf{v} - \omega)^2 + \gamma^2]} , \quad (\text{II-87})$$

and

$$P_0' = \lim_{\gamma \rightarrow 0} \frac{\gamma}{\pi} \int \frac{\mathbf{k} \cdot \partial F_0 / \partial \mathbf{v} d\mathbf{v}}{[(\mathbf{k} \cdot \mathbf{v} - \omega)^2 + \gamma^2]} . \quad (\text{II-88})$$

The effect of fast and superfast electrons will be modelled by generalizing  $F_0$ .

The definition of the average collision frequency is retained, so that when

applied to the bulk Maxwellian,

$$\frac{\bar{v}}{\omega_p} = \frac{Z \ln \Lambda}{n \lambda_D^3 3(2\pi)^{3/2}} \ll 1 . \quad (\text{II-89})$$

The major contributor to the collision frequency comes from particles of average energy [Eq. (II-64)]. That is, the contribution from non-thermal electrons is considered to be negligible as compared to the contribution from the background Maxwellian,  $F_0$ . Substituting Eqs. (II-86) through (II-89) into Eq. (II-85) yields the power spectrum,

$$I(\mathbf{k}, \omega) = \frac{\omega_p^2 [ P_0 + 2k^2 k_B T_c \bar{v} (\pi \omega_p^4 m)^{-1} ]}{4 \{ (\omega - \omega_p)^2 + [ \bar{v} - \pi \omega_p^3 P_0' (2k^2)^{-1} ]^2 \}} . \quad (\text{II-90})$$

The thermal correction term is small and has been neglected so that  $\omega_{BG} = \omega_p$ .

The power spectrum determines the shape of the scattered spectrum. The scattered power, however, is the product of the total number of scatterers,  $N$ , and the power spectrum:

$$\frac{1}{P_i} \frac{dP}{d\Omega d\omega_s} = \frac{N}{A} \sigma_T(\theta, \phi) I(\mathbf{k}, \omega) , \quad (\text{II-91})$$

where  $A$  is the area of the laser beam. The Thomson scattering cross section,

$$\sigma_T(\theta, \phi) = r_0^2 [ 1 - \sin^2 \theta_s \cos^2(\phi - \phi_0) ] , \quad (\text{II-92})$$

accounts for variations at angles,  $\theta_s$ , from the incident directions, and  $\phi - \phi_0$  is the angle between the projection of the scattered beam on the plane normal to the incident and the incident electric polarization vector. Because this is an inhomogeneous plasma, the total scattered power is then a function of position in the plasma through the varying density,  $n(x)$ , and the density (position) dependence of the power spectrum. If the plasma varies along the direction of the laser beam, say in the  $x$  direction, then the

scattered power is more properly generalized to

$$\frac{1}{P_i} \frac{dP}{d\Omega d\omega_s} = \int n(x) \sigma_T I(k, \omega, x) dx, \quad (\text{II-93})$$

where the dependence of the power spectrum,  $I(k, \omega)$ , on position through  $\omega_p^2$  and  $F_0$ , is explicitly stated in  $I(k, \omega, x)$ . The electron temperature is assumed to be constant throughout the plasma corona.

Because  $I(k, \omega)$  is resonant at points where  $\omega^2 = \omega_p^2$ , the integral (over  $x$ ) in Eq. (II-93) will be highly peaked at points,  $x_0$ , where the frequency,  $\omega$ , is at its critical density:  $\omega^2 = \omega_p^2(x_0)$ . The density may then be expanded in a Taylor series about this point,

$$\omega_p^2(x) = \frac{4\pi e^2}{m} n(x) = \omega_p^2(x_0) + \frac{4\pi e^2}{m} n'(x_0) (x - x_0), \quad (\text{II-94})$$

so that

$$\omega_p^2(x) = \omega_p^2(x_0) [1 + (x - x_0)/L]. \quad (\text{II-95})$$

The local density scale length,  $L$ , is defined by

$$L \equiv \frac{n(x_0)}{n'(x_0)}. \quad (\text{II-96})$$

Substituting this into Eq. (II-93) yields

$$\frac{1}{P_i} \frac{dP}{d\Omega d\omega_s} = n(x_0) \sigma_T \omega^2 [P_0 + 2k^2 k_B T_c \bar{v} (\pi m \omega^4)^{-1}] R, \quad (\text{II-97})$$

where

$$R = \int_{x_0}^{+\infty} \frac{dx}{\omega^2 (x - x_0)^2 L^{-2} + (2\bar{v} - \pi \omega^3 P_0' k^{-2})^2}$$

$$= \frac{\pi L}{|\omega| |2\nu - \pi \omega^3 P'_0 k^{-2}|} \quad (\text{II-98})$$

The integral is over all of the underdense plasma. Because the numerator of  $I(k, \omega)$  [Eq. (II-90)] is nonresonant, the values of the plasma frequency and of the integral  $P_0$  have been assumed to be those of the resonant point. The scattered power, prior to specializing to a laser plasma, is then

$$\frac{1}{P_i} \frac{dP}{d\Omega d\omega_s} = \frac{n(x_0) \sigma_T L |\omega| \pi [P_0 + 2k^2 k_B T_c \bar{v} (\pi m \omega^4)^{-1}]}{|2\nu - \pi \omega^3 P'_0 k^{-2}|} \quad (\text{II-99})$$

Large enhancements in the scattered power can occur when the growth of the plasma waves via inverse Landau damping, represented by  $P'_0$ , balances the damping due to collisions.

There remains only to develop a realistic model of the electron distribution function,  $F_0$ . The bulk of the electrons are heated by inverse bremsstrahlung absorption of the laser energy. For plasmas where  $Zv_{osc}^2/v_T^2 \ll 1$ , (the case here), the electrons may be characterized by a Maxwellian distribution with a cold temperature,  $T_c$ , because the electron-electron collisions are rapid enough to thermalize the distribution produced by inverse bremsstrahlung.<sup>32,33</sup>

Electron-heating mechanisms occur at positions in the plasma where large electric fields are produced. The large fields drive strong electron oscillations that produce longitudinal electron-plasma waves. One possible mechanism for the production of the fast electrons is wavebreaking that occurs when the orbits of the electrons cross each other,<sup>34</sup> or more physically, wavebreaking occurs when the oscillation velocity of the electron in the enhanced electric field equals the phase velocity of the wave. Electrons are accelerated to energies far above their thermal levels and are excited in a beam. If the amplitude of plasma-wave field at wavebreaking is denoted by

$E_w$ , the energy gained by an electron through wavebreaking is approximately  $eE_w L$  because the electrons accelerate through a potential  $eE_w$  over a scale-length distance,  $L$ .<sup>35</sup> These electrons may still maintain their relative velocity distribution, but now have a directed velocity,  $v_b$ . The electrons are in a beam that is traveling up or down the density gradient because the electron plasma waves will tend to propagate in this direction due to refraction.<sup>13</sup> The beam can be reflected by sheaths at either the overdense or underdense edges of the plasma so it is possible for the same electrons to traverse the plasma more than once. A characteristic “temperature” is assigned to this beam of electrons by

$$k_B T_b = \frac{1}{3} m v_b^2 . \quad (\text{II-100})$$

There are two classes of mechanisms that can produce the greatly enhanced electric fields needed to create non-thermal electrons. The first of these is resonance absorption<sup>30</sup> which occurs at the critical-density surface and creates a large electric field which resonantly drives electron oscillations producing longitudinal electron-plasma waves.<sup>37</sup> The amplitude of the plasma-wave field,  $E_w$ , at wavebreaking in a linear density profile is<sup>38</sup>

$$\frac{eE_w}{m\omega_0} = \sqrt{\frac{2cE_d L}{m}} , \quad (\text{II-101})$$

where  $E_d$  is the component of the laser field that drives the oscillation and  $L$  is the linear density scale length. The electrons produced by RA are termed “fast” or “hot” and can cause a large amount of fuel preheat in inertial confinement fusion of infrared-laser irradiated targets. Shorter-wavelength lasers suppress the production of fast electrons.

Parametric instabilities at densities below critical produce superhot electrons where the instability has increased the electric field so that electrons are accelerated via

wavebreaking or trapping in an electron-plasma wave. Trapping occurs when the plasma-wave field vector is strong enough to accelerate electrons to the wave-phase speed,  $v_\phi$ , from an initial velocity  $U$  in a single period<sup>39</sup>:

$$U + \frac{2\pi e E_w}{m\omega} = v_\phi . \quad (\text{II-102})$$

Trapping is the more dominant acceleration mechanism because the required electric field is lower than that for wavebreaking. Wavebreaking may still be important, and, in the corona, produces electron-plasma waves with a phase velocity<sup>40</sup> of  $v_\phi = c/\sqrt{3}$ . According to some simulations, the electron distribution produced is approximately Maxwellian,<sup>39,41</sup> although there is some experimental evidence that the electrons are in a nearly monoenergetic beam.<sup>42</sup> Because the instabilities are in a cycle of exponential growth, saturation, and collapse, the accelerated electrons emerge in bursts that move through the plasma and can be reflected at sheaths. Locally, this produces a transient bump-on-tail (BOT) electron velocity distribution if the number of hot electrons exceeds some minimum value.

The two conditions for fast electron generation are the production of plasma waves and the localization of the generation region. Three parametric instabilities satisfy these criteria. The first is the two plasmon decay (TPD) instability. This three-wave process satisfies the energy matching condition

$$\omega_i = \omega_1 + \omega_2 , \quad (\text{II-103})$$

and the two daughter plasma waves must each satisfy the dispersion relation

$$\omega_{1,2}^2 = \omega_{pe}^2 + 3 v_T^2 k_{1,2}^2 . \quad (\text{II-104})$$

When combined, these two conditions constrain the instability to the quarter-critical density surface. The existence of this instability is difficult to show in submicron-laser plasmas since the two decay products are non-radiating plasma waves. The presence of

TPD, however, has been inferred from measurements of super-hard x rays,<sup>40</sup> the x-ray continuum,<sup>43</sup> secondary emission<sup>44</sup> at  $3\omega_0/2$ , and also by increases in the level of unpolarized scattering at  $\omega_0/2$ .<sup>45</sup> The plasma waves have been measured directly in a CO<sub>2</sub>-laser-produced plasma using a Thomson scattering diagnostic.<sup>46</sup> The superhot electrons produced by TPD in a UV-laser plasma have also been measured directly with an electron spectrometer.<sup>47</sup>

The second hot-electron generating instability is absolute stimulated Raman scattering (SRS-A),<sup>48</sup> which occurs at either the  $n_c/4$  surface or at the extremum of a parabolic density profile.<sup>49</sup> In Raman scattering, the two daughter waves are a plasma wave obeying the dispersion relation Eq. (II-104), and a scattered-light wave obeying the dispersion relation

$$\omega_s^2 = \omega_{pe}^2 + c^2 k_s^2, \quad (\text{II-105})$$

where  $\omega_s(k_s)$  is the wave frequency (wave vector) of the scattered light wave. The absolute instability grows in time at a localized position, in contrast to the convective stimulated Raman scattering (SRS-C) instability which grows as a function of position (the region of growth “convects” through the plasma). Observations of scattering that have been unequivocally attributed to SRS-C are rare.<sup>45,50</sup> The SRS-A instability, however, has been conclusively identified from observations of scattered light at  $\omega_0/2$  or at wavelengths appropriate to the peak density present in a plasma with a parabolic density profile.<sup>45,51</sup>

Another parametric instability that can produce suprathermal electrons is the Parametric Decay Instability (PDI).<sup>52</sup> The daughter waves for this three-wave interaction are an ion-acoustic wave and a plasmon. For this reason, PDI is also known as the ion-plasmon decay instability. Because the ion frequency is always much smaller than the pump frequency, the instability occurs near the critical density. The

plasma wave vector is much larger than the pump wave vector at the critical density which means that the plasmon and the ion-acoustic wave have large transverse components. It is expected that in long-scale-length plasmas, PDI will be a more important source of fast electrons than will resonance absorption.<sup>52</sup>

There is now enough information to build a model of the electron distribution function. In general, the distribution function will consist of three parts; however, only two temperature components will be considered here: the cold and superhot components. The effects of adding the hot-electron component will be discussed in the next section. The temperature of the superhot component will be assigned by assuming that the mean thermal energy of the superhot electrons is equal to the energy in the beam:

$$k_B T_{sh} = k_B T_b = \frac{1}{3} m v_b^2 . \quad (\text{II-106})$$

Therefore, the electron distribution function is

$$F_0(v) = F_c(v) + f_{sh} F_{sh}(v) , \quad (\text{II-107})$$

where

$$F_c(v) = \frac{1}{2} \left( \frac{m}{2\pi k_B T_c} \right)^{3/2} \exp \left( - \frac{m}{2k_B T_c} v^2 \right) , \quad (\text{II-108})$$

and

$$F_{sh}(v) = \frac{1}{2} \left( \frac{m}{2\pi k_B T_c} \right)^{3/2} \mathbf{X} \exp \left( - \frac{m}{2k_B T_c} [(v_x - v_{sh})^2 + v_y^2 + v_z^2] \right) + \{ v_{sh} \rightarrow -v_{sh} \} . \quad (\text{II-109})$$

The superhot-electron fraction,  $f_{sh}$ , is simply the number of superhot electrons divided by the number of cold background electrons at any local point. It is usually smaller



than 1 for a laser plasma. The only free parameter is  $f_{sh}$  if the cold and superhot electron temperatures for a particular experiment are known.

The total scattered power may then be found from inserting Eqs. (II-107) and (II-100) into Eq. (II-99),

$$\frac{1}{P_i} \frac{dP}{d\Omega d\lambda_s} = \frac{n_c L \sigma_T}{\lambda_0} S, \quad (\text{II-110})$$

where the differential scattered power is now in terms of the scattered wavelength,  $d\lambda_s$ , to make comparison with experiments easier. The incident laser wavelength is  $\lambda_0$ , corresponding to a critical density  $n_c$ . The density scale length has been assumed to be constant. The shape factor,  $S$ , is

$$S = \frac{1}{2} \left( \frac{\omega_s}{\omega_0} \right)^2 \frac{\omega W}{\omega_0 D}, \quad (\text{II-111})$$

where

$$W = (E_p/k_B T_c)^{1/2} \exp(-E_p/k_B T_c) + k_B T_c \bar{\nu} / E_p \pi^{1/2} |\omega| + f_{sh} \mu^{1/2} |y| \exp[-\mu(|y|^2 - 1)^2], \quad (\text{II-112})$$

$$D = (\bar{\nu} / \pi^{1/2} |\omega|) + (E_p/k_B T_c)^{3/2} \exp(-E_p/k_B T_c) + f_{sh} \mu^{3/2} y^2 (|y| - 1) \exp[-\mu(|y| - 1)^2], \quad (\text{II-113})$$

and

$$E_p \equiv \frac{1}{2} m \left( \frac{\omega}{k} \right)^2, \quad \omega \equiv \omega_0 - \omega_s, \quad k \equiv |\mathbf{k}_0 - \mathbf{k}_s|, \\ \mu \equiv \frac{3T_{sh}^2 k_x^2}{2T_c k^2}, \quad \text{and} \quad y^2 \equiv \frac{2E_p k^2}{3k_x^2 k_B T_{sh}}. \quad (\text{II-114})$$

The average collision frequency can also be found:

$$\frac{\nu}{\omega} \approx \frac{\omega Z \ln \Lambda}{\omega_0^3 (2\pi)^{3/2} (n\lambda_D^3)_c}, \quad (\text{II-115})$$

where  $(n\lambda_D^3)_c$  is evaluated at the critical surface. These equations are only valid for  $\omega_s \approx \omega_p$  and have been derived by neglecting the contribution of the central ion peak.

Scattering bands occur for frequencies where the shape factor is resonant. That is, large increases in the scattered power occur for frequencies that make the shape factor denominator,  $D$ , small or negative. This term can only be negative if  $|y| - 1 < 0$ , making the third term of  $D$  negative. This is equivalent to requiring that

$$m(\omega/k_x)^2/3 < T_{sh}; \quad (\text{II-116})$$

the phase velocity of the electron-plasma wave must fall on the reverse slope of the hot-electron pulse, as shown in Figure II-2. If the phase velocity is larger than this value, the radiation will be damped. Inspection of Figure II-2 shows that there is also a limit on how small the phase velocity may be that depends not only on the value of the hot-electron pulse "temperature," but also on the width of the background Maxwellian distribution through  $T_c$ .

As  $T_c$  gets larger, the total electron distribution function no longer has two separate peaks as in Figure II-2, but develops a plateau where the two different components overlap as shown in Figure II-3. In this plateau region there is no reverse slope to amplify any plasma waves, however, there is no positive slope to Landau damp the waves. Hence the electron-plasma waves appear enhanced by the lack of actual damping. Increasing  $T_c$  will narrow and then eliminate the region available for growth. For very small  $T_c$ , the width of the "bump" is very narrow and the resonance region is correspondingly small. Increasing  $T_{sh}$ , the energy of the superhot-electron pulse, allows reverse-slope growth for larger values of  $T_c$ .

## Bump-on-tail Instability

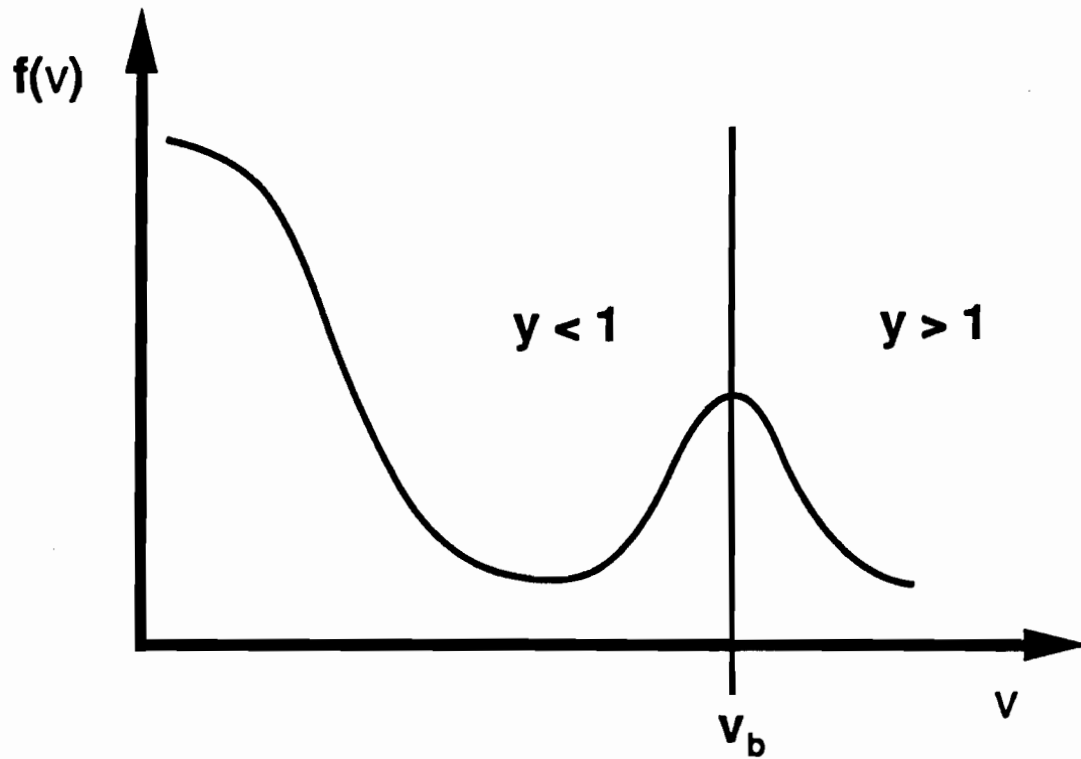


Figure II-2. Considerable enhancement of electron-plasma waves is possible when  $y < 1$ . This corresponds to the wave phase velocity falling on the reverse slope of the hot-electron pulse.

## Large Region with no Damping

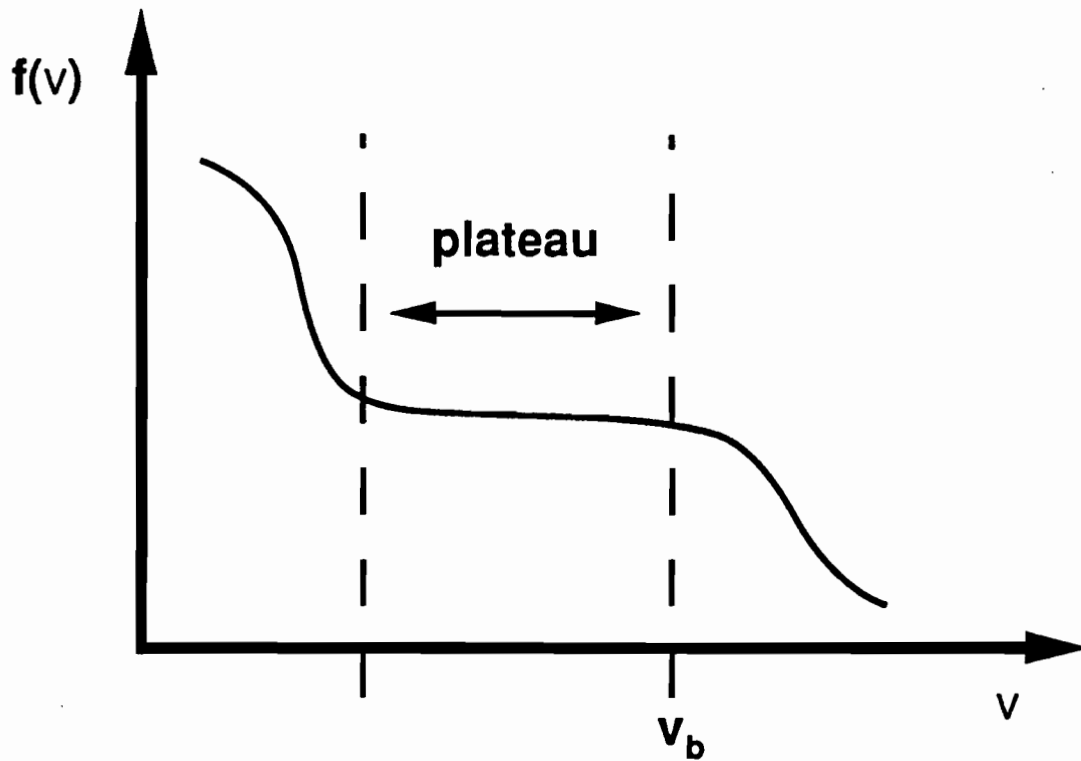


Figure II-3. For lower values of  $T_b$  and higher values of  $T_c$ , a large plateau is formed that will neither enhance nor damp the plasma waves. For still lower values of  $T_b$ , all plasma waves are damped and there is no scattering.

## D. Predictions of the Theory

Enhanced Thomson scattering is fundamentally different than the parametric instabilities. For example, the stimulated Raman scattering instability (SRS) occurs due to the coupling of a scattered electromagnetic (EM) wave with a plasma wave through the presence of an oscillating EM pump wave. An initial electron-density perturbation (noise) produces a transverse current due to the oscillatory pump wave, which in turn produces a scattered EM wave. The ponderomotive force of the interacting incident and scattered EM waves enhances the initial density perturbations.<sup>53</sup> This feedback mechanism will amplify the plasma and scattered EM wave amplitudes exponentially until the instability saturates by convection or by some nonlinear process. To initiate this cycle, the pump wave must be strong enough to overcome any losses in this system, including convection and damping of the waves. Therefore, a threshold pump power (i.e., threshold laser intensity) will exist for SRS.

Even below the threshold for the SRS instability, there will still be “ordinary” Raman scattering of EM light by interaction of the pump wave with collective thermal fluctuations in the plasma. This scattered EM light is what is called the “electron-line feature” of classical Thomson scattering. As long as the plasma waves are at thermal levels, the fractional energy scattered this way is quite small. The blackbody emission from a laser-produced plasma has been estimated to be  $10^{-3}$  J/sr/cm<sup>2</sup> for conditions appropriate to a Novette green experiment.<sup>54</sup> The apparent noise level was measured in an experiment<sup>54</sup> where the noise was assumed to be the amount of energy scattered into the wavelength region between 600 and 950 nm from a low laser-intensity irradiance ( $\lambda_{\text{laser}} = 0.53 \mu\text{m}$ ) and was found to be  $e^7$  to  $e^9$  times greater than the blackbody emission. Thermal Thomson scattering will increase the noise level above thermal. The total Thomson cross section is calculated to be  $\sigma \approx 7 \times 10^{-10}$  cm<sup>2</sup> for scattering

from a plasma volume of  $10^{-6} \text{ cm}^3$  at the quarter-critical density of a 527-nm-laser-produced plasma.<sup>55</sup> If, for some reason, the electron distribution deviates significantly from Maxwellian, considerable enhancement of some of the plasma-wave levels may exist. In such a case, enhancement of the corresponding Raman scattering may occur. This chain of events is known as enhanced Thomson scattering. If only the lower frequency electron-line feature is measured, this process could be easily mistaken for SRS-C since the SRS-C signal also occurs near this frequency range.

Even when the SRS threshold is exceeded, the exponential growth of the scattered EM wave proceeds from an initial noise level. Those plasma densities at which enhanced plasma-wave levels already exist will contribute most efficiently to the initial Raman noise level; thus the enhanced "seed" may still determine the frequency spectrum of the observable SRS scattering.

Equations (II-103) through (II-105) imply that the frequency of the Raman scattered light is proportional to the plasma density at its origin and that the scattered SRS EM wave may occur only in the frequency interval<sup>56</sup>  $\omega_0/2 < \omega_s < \omega_0$ . The threshold for convective SRS (SRS-C) in an inhomogeneous plasma is given by<sup>57</sup>

$$\left( \frac{v_{\text{osc}}}{c} \right)^2 k_0 L > 1 , \quad (\text{II-117})$$

where  $v_{\text{osc}}$  is the electron oscillatory velocity,  $k_0$  is the laser wave number inside the plasma, and  $L$  is the plasma scale length. In physical units, the threshold condition on the incident intensity may be written as

$$I_{\text{SRS-C}} = \frac{4.4 \times 10^{17} \text{ W}}{L_{\mu} \lambda_{\mu} \text{ cm}^2} , \quad (\text{II-118})$$

with  $L_{\mu}$  and  $\lambda_{\mu}$  expressed in microns. In the experiment described in Chapter III,

$\lambda_{\mu} = 0.527$  and  $L_{\mu} = 80$ , corresponding to an intensity threshold of  $1 \times 10^{16}$  W/cm<sup>2</sup>. The long-scale-length experiment described in Chapter IV had  $\lambda_{\mu} = 0.351$  and  $L_{\mu} = 1500$ , corresponding to an intensity threshold of  $8 \times 10^{14}$  W/cm<sup>2</sup>.

Absolute SRS has a much lower threshold,<sup>58</sup>

$$I_{\text{SRS-A}} = \frac{4 \times 10^{17}}{[L_{\mu}^2 \lambda_{\mu}]^{2/3}} \frac{\text{W}}{\text{cm}^2}, \quad (\text{II-119})$$

which, for the above two cases, is an order of magnitude smaller than the SRS-C threshold. It is therefore possible that only the absolute instability could be excited. Because SRS-A occurs only at  $n_c/4$  in a monotonic density profile, scattered light is emitted only near  $\omega_0/2$ . Enhanced Thomson scattering, in contrast, has no intensity threshold as such, but does require an electron distribution that is non-Maxwellian, such as the BOT model discussed in the previous section with sufficient numbers of hot and superhot electrons.

If it is assumed that the fast-electron bursts move up and down along the direction of the density gradient, it is possible to calculate the resulting enhanced Thomson scattering, as derived in the previous section. Numerical calculations show that the enhanced scattering in an inhomogeneous plasma will occur whenever the electron-plasma wave and the hot-electron pulse are in resonance. Generally, the resonance regions scatter light into two bands: one, a down-scatter band between  $\omega_0$  and  $\omega_0/2$ ; the other an up-scatter band between  $2\omega_0$  and  $\omega_0$ . The two bands are not symmetrical about  $\omega_0$ , nor need they have the same minimum number of fast electrons (i.e., the same threshold) for the enhancement to occur.

The widths of the two bands differ because the wave vectors of the scattered waves are different for the two bands. As was required in Eq. (II-116), the electron-plasma wave phase velocity,  $(\omega/k_x)$ , must fall within some range determined

by the fast and background temperatures. In down-scattering,  $\omega < \omega_0$ , and some range of  $(\omega, k_x^d)$  pairs are resonant. In order for the up-scattering to be in resonance, different wave vectors are required since  $\omega > \omega_0$ . Consequently,  $k_x^u > k_x^d$ . Therefore, the widths of the bands are expected to be different. The shift of these bands from the laser frequency is asymmetric because the electron-plasma wave vectors are different.

If there are two distinct hot temperatures identified in an experiment, a second pair of enhanced scattering bands is expected to be present. However, the minimum number of hot electrons required may vary considerably from band to band, and so not every band need be observed in any given experiment.

The spectral location and width of the bands are also functions of three variables: the angle of incidence of the laser relative to the density gradient, the angle of observation, and the average ionic charge. All these variables have been included in a numerical calculation.<sup>59</sup> The predicted locations of the scattering bands are usually insensitive to the value of  $T_c$  because the phase-matching requirement is determined by  $T_b$ , the effective temperature of the directed pulse of suprathermal electrons. A certain fraction of hot electrons is required to form the "reverse-slope" amplification region that initiates the scattering bands. As this fraction is increased, the width of the band will also increase (the resonance region in Figure II-2 is getting larger) because more suprathermal electrons increases the range of phase velocities that fall on the reverse-slope portion of the electron distribution. The upper phase-velocity limit will not vary appreciably because the "temperature" of the suprathermals is not changing. Therefore, one edge of the scattering band will shift to widen the band as the hot-electron fraction increases, but the other edge will remain fixed.

An example of a simulated spectrum for the conditions of this experiment, including refraction, is shown in Figure II-4, where the enhanced wavelength bands are



$T_c = 1.5 \text{ keV}$      $\lambda_o = 527 \text{ nm}$      $Z = 3$      $\text{tilt} = 45^\circ$

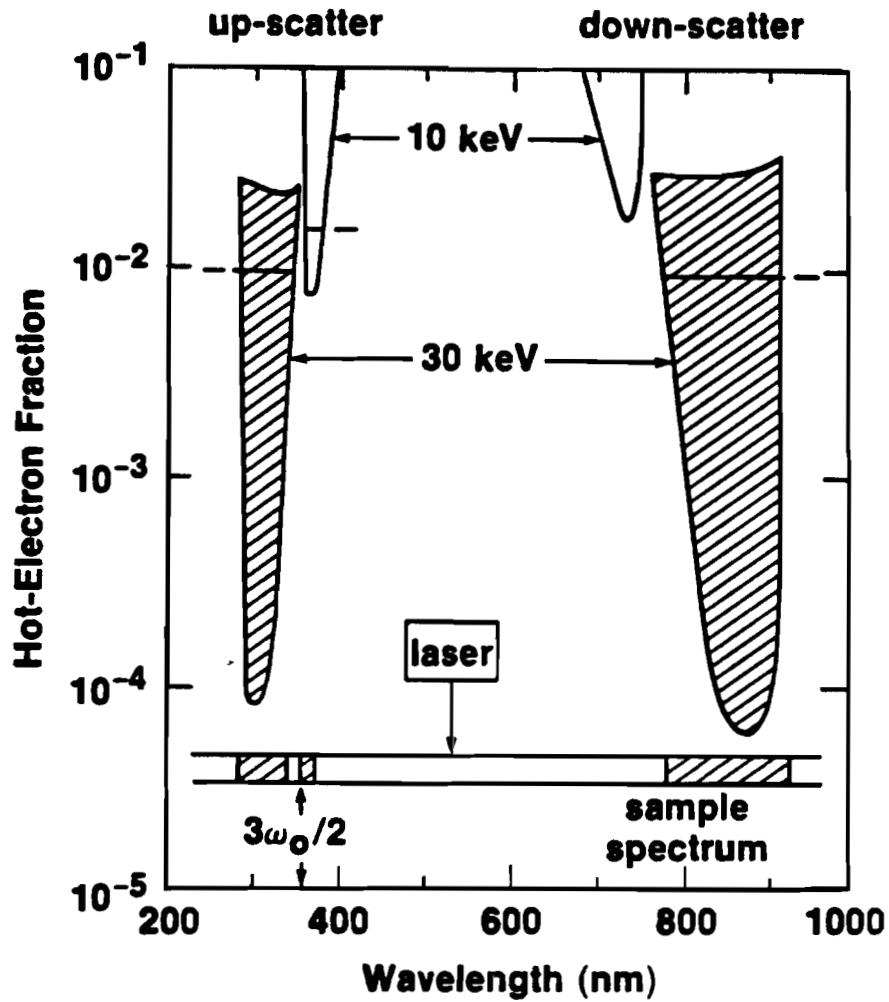


Figure II-4. The scattering bands predicted by ETS theory to radiate at a  $45^\circ$  angle from the laser beam. The target is tilted at  $45^\circ$  from the laser beam and has an ionization state of  $Z = 3.5$ . The electron temperatures were  $T_{sh} = 30$ ,  $T_h = 10$ , and  $T_c = 1.5 \text{ keV}$ .

shown as a function of  $f_b$ , the fraction of directed suprathermal electrons in the pulse relative to the background density. This calculation assumed a tilted target at  $45^\circ$ , a laser wavelength of  $\lambda_0 = 527$  nm, an average ionic charge of  $Z = 3$ , a cold temperature of  $T_c = 1.5$  keV, and a suprathermal temperature of 30 keV which is typical of superhot electrons. There is as yet no reliable theory which will predict the number of fast electrons; hence,  $f_b$  is unknown. Fortunately, the central location of each band is quite insensitive to the value of  $f_b$ . As an example, if the suprathermal-electron fraction is equal to 1%, Figure II-4 then predicts an up-scattered band between 286 and 350 nm and a down-scattered band between 777 and 920 nm. Note that unlike SRS theory, this theory predicts a gap between the long-wavelength limit of the down-scattered feature and the half-harmonic at 1054 nm. Also noteworthy is that the up-scattering feature extends to wavelengths shorter than  $3\omega_0/2$ .

Figure II-4 also shows the additions to the predicted spectrum if another, lower temperature, component is present. An additional pair of bands is produced. As an example, for  $T_b = 10$  keV, typical of hot electrons from resonance absorption in a 527-nm laser-produced plasma, and  $f_b = 8\%$ , there will be up-scattering between 360 and 400 nm, on the long wavelength side of the three-halves, and down-scattering between 690 and 760 nm. A four-peaked spectrum would be observed if a large fraction of the electrons were in both the hot and superhot components.

In producing Figure II-4, it was assumed that the presence of a third temperature component would have no effect on the other two components. In reality, the third component may modify the electron distribution function enough to cause changes in the width of the scattering bands, depending on the relative values of  $T_h$ ,  $T_{sh}$ ,  $f_h$ , and  $f_{sh}$ . As  $T_h$  is increased, the width of the scattering band attributed to *superhot* electrons would first decrease after  $T_h$  reached some significant fraction of  $T_{sh}$

because the negative slope region would be decreased. The width of the scattering band due to hot electrons would increase (as well as shift away from the laser frequency) because the negative slope region would grow larger as the hot "bump" separated from the background distribution. Eventually, the hot "bump" would lie close enough to the superhot "bump" to create one large scattering band. The temperature ranges for this to occur depend on the magnitudes of  $f_h$  and  $f_{sh}$ , the relative local populations of the two distributions, and have not been calculated explicitly.

There are two points in Figure II-4 that will be useful to note when interpreting experimental results. First, the superhot-electron fraction threshold for down-scattering is much lower than that for scattering caused by hot electrons. It is entirely possible that only the superhot down-scattering band will be observed. Second, while the superhot-electron fraction threshold for down-scattering is lower than that for up-scattering, the reverse is true for the hot features. In fact, the hot up-scatter threshold is less than half of that for the hot down-scatter threshold. It is therefore possible that there are enough hot electrons to produce the up-scattering band, but not enough to produce the corresponding down-scattering band.

### **E. Alternative Theory**

Stimulated Raman scattering (SRS) must be considered as an alternative theory to explain the scattered-light spectrum from a laser-produced plasma. At intensities above its threshold, convective stimulated Raman scattering (SRS-C) could produce a down-scattered (Stokes) band that could extend from near  $\omega_0/2$  to the laser frequency,  $\omega_0$ . Under certain geometrical conditions, SRS-C also could produce a weaker up-scattered (anti-Stokes) band.

As has been seen from Eqs. (II-103) through (II-105), the frequency of the SRS-C scattered wave may only occur in the range  $\omega_0/2 < \omega_s < \omega_0$ , although some unexplained scattering below  $\omega_0/2$  has been observed in Novette green experiments at Lawrence Livermore National Laboratory.<sup>54</sup> The frequency of the scattered wave is directly proportional to the plasma density at the point of creation of the scattered light. Because the SRS growth rate is highest near the  $n_c/4$  surface, it is expected that the SRS signal will be most intense at frequencies near  $\omega_0/2$ . Scattered light at frequencies near  $\omega_0$  correspond to scattering from very low density regions. Since this density range is always present, it is expected that scattering near  $\omega_0$  should always be present.

Absolute stimulated Raman scattering (SRS-A) may also provide an explanation of these spectra. The usual SRS-A instability only occurs at  $n_c/4$ , producing scattered light in the frequency region near  $\omega_0/2$ . In recent presentations,<sup>60</sup> the production of SRS-A at discrete "scattering sites" where the electron density has a local minimum or maximum and the background plasma density is less than quarter-critical, has been postulated. This theory allows the production of scattered light at any frequency between  $\omega_0/2$  and  $\omega_0$  because the frequency is directly proportional to the density at the density extremum of the scattering site. Through the production of the anti-Stokes mode, up-scattered light with a frequency between  $\omega_0$  and  $3\omega_0/2$  is accessible; however, scattering at frequencies above  $3\omega_0/2$  is not allowed. No complete theory or conclusive experimental results have been presented.

There are several problems with an SRS-C interpretation of scattered light spectra. The first is that the spectrum does not extend from  $\lambda_0$  to  $2\lambda_0$  as would be expected from the frequency and wave-vector matching conditions. There are two "gaps" in the spectrum, as illustrated in Figure II-5. At higher frequencies, Landau damping is expected to become important and efficiently damp the plasma waves to cut

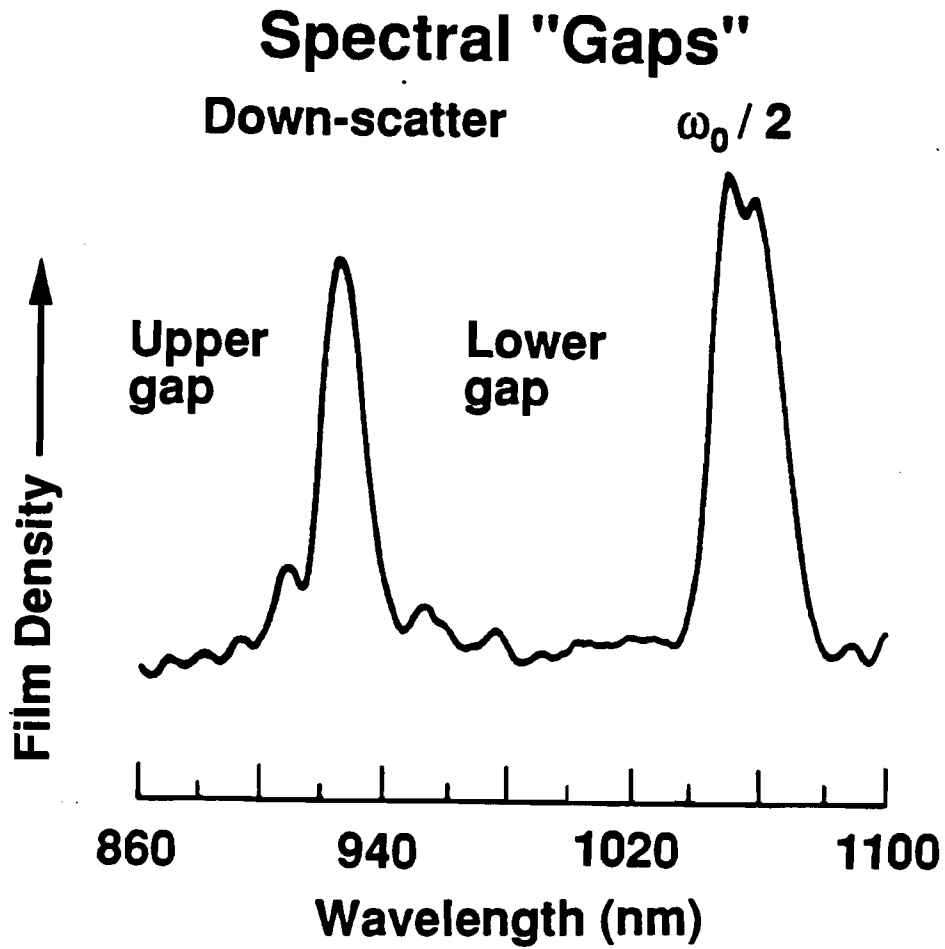


Figure II-5. A typical down-scattered-light spectrum from a 527-nm laser-produced plasma shows the existence of two gaps in the spectrum. The "lower gap" is between the ETS signal and the  $\omega_0/2$  feature whereas the "upper gap" is between the ETS signal and the laser frequency,  $\omega_0$ .

off the scattering. This phenomena has been used as a temperature diagnostic by assuming that the plasma-wave cutoff is at approximately  $k\lambda_D = 0.2$  and then solving for the temperature as a function of the short-wavelength edge of the observed scattering:

$$T_e = \frac{e^2 \lambda_s^2}{25\pi} n . \quad (\text{II-120})$$

This estimate is difficult to confirm experimentally since small shifts of the short-wavelength edge of the scattering band imply large changes in the plasma temperature. Since the most reliable temperature diagnostic, the x-ray continuum spectrometer, measures the time-integrated electron temperature, direct comparison to the rapidly changing temperature is not relevant.

The low-frequency gap has been ascribed to density profile steepening due to ponderomotive forces near  $n_c/4$ , but without direct supporting evidence.<sup>45</sup> If the profile steepening is caused by ion fluctuations<sup>41</sup> producing a ponderomotive force, it is expected that the "steepness" of the density profile, and hence the size of the gap, would increase as the laser intensity is increased. However, the experimental evidence is that the gap decreases as the intensity is increased.<sup>45</sup> The ETS theory naturally predicts this low-frequency gap as the region where plasma waves are no longer in resonance with the hot-electron pulse.

The second problem with SRS-C is that its theoretical threshold is at least an order of magnitude above the experimentally measured threshold of the down-scattered light. Also, the intensity threshold of down-scattering seems to be better correlated with the threshold intensity of the SRS-A instability whose threshold is predicted to be lower than that for SRS-C [Eq. (II-119)].<sup>12,13,29</sup>

In a laser plasma, an anti-Stokes line may be excited by "piggybacking" on a

growing Stokes mode. However, usually only the Stokes line will be observed because the intensity of the anti-Stokes mode is too small. The dispersion relation governing this joint interaction can be shown to be

$$\omega^2 - \omega_{BG}^2 = \frac{\omega_{pe}^2 v_{osc}^2 k^2}{4} \left[ \frac{1}{D(\omega - \omega_0, k - k_0)} + \frac{1}{D(\omega + \omega_0, k + k_0)} \right], \quad (\text{II-121})$$

with  $D(\omega, k) \equiv \omega^2 - c^2 k^2 - \omega_{pe}^2$ .<sup>61</sup> The up-shifted term,  $D(\omega + \omega_0, k + k_0)$ , is non-resonant and can be neglected for back or sidescattering. For instance, the maximum growth rate,  $\gamma_{max}$ , for the Stokes mode occurs when the scattered light is directly backscattered in the direction of the laser<sup>61</sup> and is

$$\gamma_{max} = \frac{k v_{osc}}{4} \left[ \frac{\omega_{pe}^2}{\omega_{BG} (\omega_0 - \omega_{BG})} \right]^{1/2}. \quad (\text{II-122})$$

The oscillatory velocity is defined as

$$v_{osc} = \frac{e E_0}{m_e \omega_0} = 25.6 I^{1/2} \lambda_0 \text{ cm/sec}, \quad (\text{II-123})$$

where the intensity is in  $\text{W/cm}^2$  and the wavelength is expressed in  $\mu\text{m}$ . The plasma wave vector,  $k$ , for maximum growth is

$$k = k_0 + \frac{\omega_0}{c} \sqrt{1 - \frac{2\omega_{pe}}{\omega_0}}. \quad (\text{II-124})$$

For forward scattering, both terms are nearly resonant when the density is very low,<sup>62</sup>

$$|\omega_{pe}^2 - k_{BG}^2 c^2| \ll 2\omega_0 \gamma_{max}. \quad (\text{II-125})$$

For very low densities, the maximum growth rate becomes

$$\gamma_{max} = \omega_{pe}^2 v_{osc} / (c\omega_0 \sqrt{8}), \quad (\text{II-126})$$

and is valid for  $10^{-4} < n/n_c < 0.05$ .<sup>62</sup> This is the growth rate for the electron-plasma wave and consequently, the growth rate for both of the scattered light waves. The exact dispersion relation has been solved numerically for both forward and backscattering.<sup>62</sup> For a low background electron temperature ( $T_c = 1$  keV), the growth rate for backscattering is several times that for forward scattering until the density origin of the scattering is near  $n_c/4$ . The growth rates are equal at quarter-critical because the scattered light wave has zero wave number. At high temperatures ( $T_c = 10$  keV), the growth rates are nearly equal for all densities.

A set of forward scattering measurements has been performed by Turner *et al.* at Lawrence Livermore National Laboratory using the Novette laser system.<sup>50</sup> The incident-laser wavelength was chosen as  $0.53 \mu\text{m}$  to simplify data acquisition. Both up- and down-shifted scattering in the forward direction was observed. It was also observed that the down-scattered signal was 35 times more intense than the up-scattered light. The observed spectrum, when viewed as a function of inferred electron-plasma-wave frequency,  $\omega_{\text{epw}} = \pm (\omega_s - \omega_0)$ , showed that both scattering bands originated in the same density range since  $\omega_{\text{epw}}^2/\omega_0^2 = n/n_c$ . The Stokes and anti-Stokes modes must be produced at the same density since they are the result of the pump-laser wave mixing with the same plasma wave. This is in contrast with backward and forward scattering where the two processes are separate and produced as the result of the pump wave mixing with different plasma waves at different densities. This experiment probably measured scattering that was the result of SRS-C, since the laser intensity was above the instability threshold and both the Stokes and anti-Stokes modes of the Raman scattering were excited. However, the restriction of the down-scatter to a particular finite wavelength band probably results from growth on ETS enhanced noise.



These observations are not in contradiction with the predicted enhanced Thomson scattering spectrum. Measurements were not made in the spectral band where the ETS up-scattering band is predicted to occur. For example, the predicted up-scattering band, for the measured superhot temperature of  $\approx 130$  keV, lies at a shorter wavelength than the observed peak, in a region that was not experimentally observed. The wavelength position of the down-scattering band is in agreement with the ETS theory. Therefore, Turner's results do not contradict ETS theory.<sup>59</sup>

A conclusive proof that these alternative theories are inappropriate is the presence and position of the up-scattered frequency band. Even though SRS-C mixing may produce up-scattered light, the anti-Stokes mode is only resonant for propagation in the forward direction. Thus, observations in the backward direction of up-scattered light will rule out the possibility of anti-Stokes generation. There is even more conclusive proof, however. From the matching conditions, it is obvious that the scattered light from the Stokes mode of SRS is in the interval  $\omega_0 < \omega_s < \omega_0/2$ . Since the scattering into the anti-Stokes mode is symmetric in frequency, this implies that the anti-Stokes scattered light must be in the interval  $3\omega_0/2 < \omega_s < \omega_0$ . Therefore, enhanced scattered light from frequencies above  $3\omega_0/2$  cannot come from either convective or absolute Raman scattering and can only be a product of enhanced Thomson scattering.

## F. Summary

What is termed “enhanced Thomson scattering” (ETS) in this dissertation is really ordinary Raman scattering whose scattering level at the electron line is enhanced by the presence of externally generated large-amplitude electron-plasma waves. The waves are amplified by the presence of superhot or hot electrons created at the quarter-critical and critical densities, respectively. This result is obtained by Simon's generalization<sup>12</sup> of Perkins and Salpeter's theory<sup>14</sup> to an unstable and nonuniform plasma and includes the effects of a small nonisotropic electron-distribution component superimposed on a Maxwellian background plasma. The major result of their work, greatly enhanced scattering in the two electron-line features, is retained.

The major assumption of this theory is that enhanced scattering bands will occur whenever the denominator of the power spectrum,  $I(\mathbf{k}, \omega)$  [Eq. (II-90)], becomes negative. Note that no attempt has been made to predict the intensity of the scattering or to obtain a threshold other than in terms of the fraction of hot or superhot electrons. Also required is at least a two-temperature electron distribution, but no crucial details of how the hot-electrons are generated have been assumed. Although it is assumed that the hot electrons have a velocity spread determined by the background velocity distribution, this has been shown, via computations, to have little effect on the scattered light.<sup>63</sup> The effect of the incident laser light on the plasma (by increasing the oscillation velocity,  $v_{osc}$ ) has been examined by Boyd *et. al.*<sup>58</sup> It was shown that the down-scattered band may be broadened by higher values of  $v_{osc}$ , and that when  $v_{osc}$  is above the SRS threshold, both ETS and SRS may be present.<sup>58</sup>

Other theories that attempt to explain observed scattered light spectra were briefly discussed. The production of SRS-A at “scattering sites” that lie at densities below  $n_c/4$  may be able to produce both up- and down-scattered light, but only in the

## Chapter III: Enhanced Thomson Scattering Experiments at 0.53 $\mu\text{m}$

An experiment was devised to test the predictions of the enhanced Thomson scattering (ETS) theory<sup>12,13</sup> using the single-beam Glass Development Laser (GDL) system<sup>64,65</sup> at the Laboratory for Laser Energetics. A single-beam laser-plasma interaction experiment is a simple and straightforward test of the ETS theory. For example, the use of a single beam eliminates the ambiguity in the definition of the scattering angle that is present when multiple-beam illumination is used.

Using the GDL system also allowed a choice of irradiation wavelengths, either 0.35  $\mu\text{m}$  or 0.53  $\mu\text{m}$ . While the ETS theory is equally applicable in either case, choosing the longer wavelength simplified the experiment considerably. The primary test of the theory is the observation of up-scattered emission bands in the frequency range  $2\omega_0 < \omega_u < \omega_0$ , where  $\omega_u$  and  $\omega_0$  are, respectively, the frequencies of the up-scattered band and of the laser. These features had not been systematically studied before this experiment. If GDL were operated at 0.35  $\mu\text{m}$ , this up-scattered band would lie in the far ultraviolet and its observation would require the use of special optics and detectors. These problems were avoided when the laser wavelength was 0.53  $\mu\text{m}$ . The longer wavelength does make down-scattering measurements more difficult because the scattering band (of frequency  $\omega_d$ ), which is always in the range  $\omega_0/2 < \omega_d < \omega_0$ , is now in the near-infrared region. Special detectors are needed to observe radiation at wavelengths greater than 900 nm. This was less difficult than the far-ultraviolet measurements needed for 0.35  $\mu\text{m}$  experiments.

In this chapter, a brief discussion of the GDL system and the instruments used to diagnose the experiment is given. More detailed descriptions are given in

interval  $\omega_0/2 < \omega_s < 3\omega_0/2$ . No conclusive supporting experiments or detailed theoretical details are yet available on this theory. The SRS-C model was found to be unable to explain particulars of the down-scattered bands, the existence of up-scattered bands in the backward direction, and was also unable to correctly predict the experimentally measured intensity threshold.

Appendix A. A discussion of illumination uniformity (intensity hot spots), which was found to have a large effect on the laser-plasma interaction, is included. Scattered light spectra were collected by two 1/4-m spectrometers, giving almost complete coverage of the optical spectrum from  $\omega_0/2$  to  $2\omega_0$ . The electron temperatures were determined by measuring the x-ray continuum emitted by the target.

The results of several variations of this experiment are then described. Parameters that were changed included the angle of the target, the observation angles of the diagnostics, and the use of a streak camera to produce time-resolved down-scattered spectra in some situations. In the discussion, the data is compared with the ETS predictions and the failure of alternative theories to explain these data is explored. Finally, the results of this series of experiments are summarized.

## A. Experiment

A series of experiments using the Glass Development Laser (GDL)<sup>64,65</sup> system at the Laboratory for Laser Energetics was conducted to observe the up- and down-scattering bands. GDL is a single-beam Nd:glass system that, for this series of experiments, delivered up to 200 J at 1.054  $\mu\text{m}$ . Frequency doubling produced on-target energies of up to 60 J at 527 nm. The pulses were Gaussian in time with a typical pulse width of 600 ps after frequency conversion, although some experiments were done with 1-ns pulses. The beam was focused onto 50- $\mu\text{m}$ -thick CH targets by an  $f/3.6$  lens. The x-ray spot size at 10% of the maximum intensity, as measured by an aluminum- and beryllium-filtered pinhole camera, was 120  $\mu\text{m}$  at best focus. Assuming that the laser spot is also this size implies an average on-target intensity of  $8 \times 10^{14} \text{ W/cm}^2$ .

The actual on-target energy at any point in the interaction region may vary considerably from the average value due to hot spots in the laser beam. A typical equivalent-target-plane image (ETP) is shown in Figure III-1. The hot spots may be due to damage in the laser amplifier chain or turbulence in the beam path. Besides creating a poor far-field distribution themselves, these nonuniformities also lead to phase errors at the input of the conversion cells, which may yield substantial spatial differences in conversion efficiency, exacerbating problems at the focus of the final GDL lens. Peak-to-valley variations of 100% are not uncommon in these distributions. Especially troublesome is filamentation,<sup>66</sup> where hot spots of the order of a few microns in size may lead to increased levels of Raman scattering. No attempts were made to smooth the laser beam using distributed phase plates,<sup>2</sup> beam tubes, or other technical fixes. The variable on-target-energy distribution could cause the production of suprathermal electrons to vary from one shot to the next.

Because the scattered-light spectrum from laser-produced plasmas has strong emission at even and odd half-harmonics of the fundamental laser frequency, precautions were taken to limit the amount of third-harmonic and fundamental energy that reached the target. In particular, potential problems were third-harmonic light at 351 nm that coincided with  $3\omega_0/2$  emission when the incident wavelength was 527 nm, and resonance absorption of the 1054-nm laser energy. The residual 1054-nm light intensity was reduced by the use of an IR-absorber plate, dichroic mirrors, and by the chromatic shift of the focusing lens, resulting in  $I_{1054 \text{ nm}} = 10^{-9} I_{527 \text{ nm}}$ .

Third-harmonic light was produced when the first crystal in the conversion cell was used to produce green light. Some of the green light would mix with the residual red light to produce small amounts of 351-nm light even though the second crystal was detuned from maximum efficiency. The amount of 351-nm energy produced in this

# GDL ETP

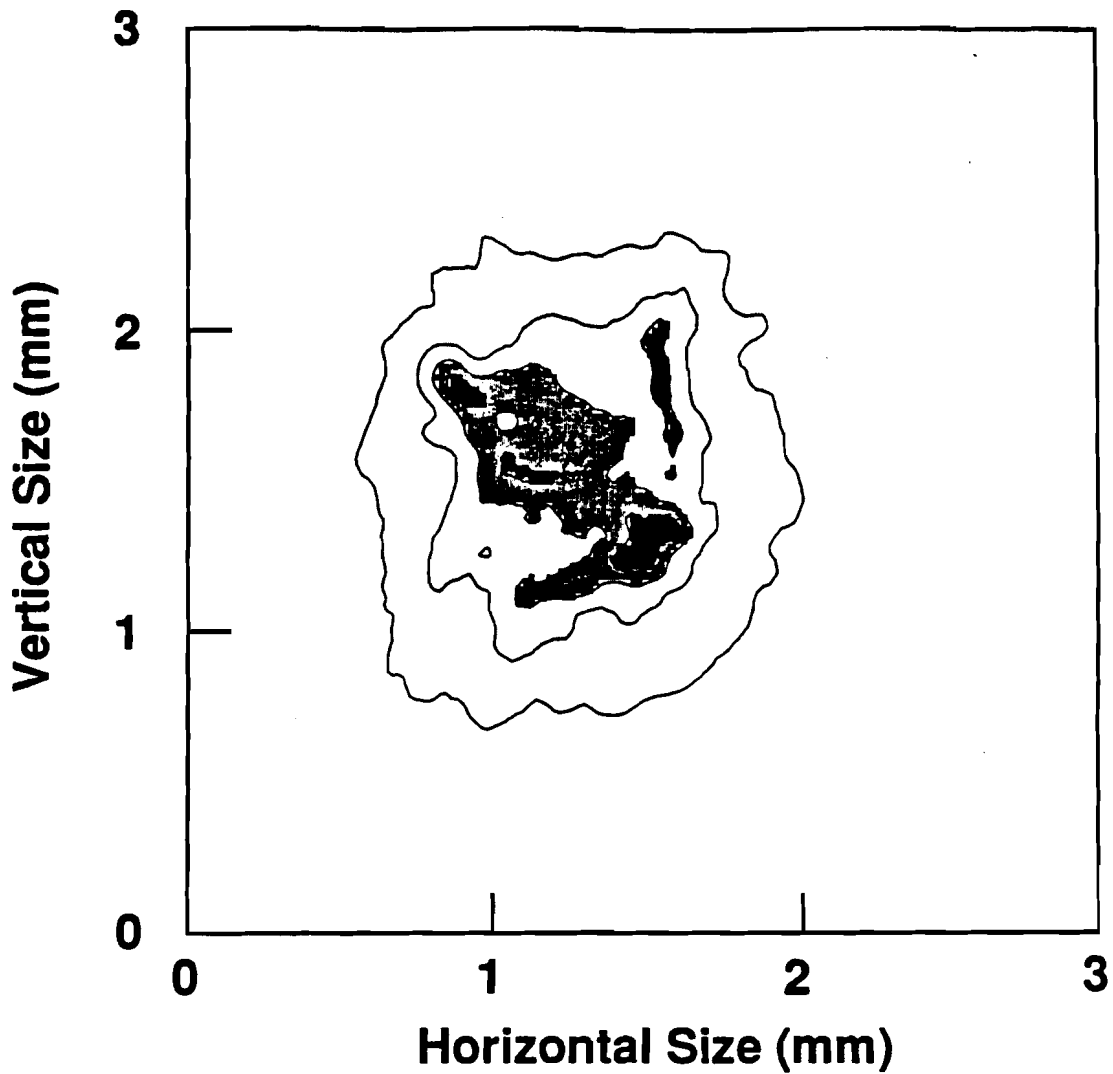


Figure III-1. Equivalent-target-plane photograph of the GDL green laser beam showing "hot spots" that could be generation zones of suprathermal electrons. The contours are at 25, 50, 75, and 95% of the maximum film density.

manner was approximately 1 J. Attenuation of this energy was made by the dichroic turning mirror and the focusing lens. The chromatic shift of the lens contributed to decreasing the blue-intensity that struck the target. Because the 351-nm light does not produce hot electrons from resonance absorption as strongly as longer wavelength lasers do,<sup>43</sup> the effects of the very low intensity 351-nm interaction were negligible. However, stray 351-nm light was apparent on the up-scattering spectra that were measured. During later experiments, the blue light was eliminated by using the second crystal in the conversion cell to produce green light. No further mixing of the light could take place and so only the 527-nm light, with some residual fundamental light, was produced.

An accurate test of the ETS theory requires measurement of three quantities: the spectral positions of the up- and down-scattering bands, and the "temperature" of the three electron components. Several different target and diagnostic orientations were used to simplify data acquisition, but they also served to measure the angular variation of the scattered light bands.

Scattered light was collected by two  $f/13$  spherical aluminum mirrors, each subtending a solid angle of 0.028 sr, and imaged onto the entrance slits of two 0.25 m spectrometers. The first (UV) spectrometer, which incorporated a cross Czerny-Turner design with a 275-mm focal length and used a 600-groove/mm grating blazed at 300 nm, was usually tuned to observe the spectrum between 250 and 425 nm in order to view the up-scattered feature; the spectrum was recorded on Kodak 2495 film, with a resolution of better than 1 nm. The second (IR) spectrometer, which was used to view the down-scatter at wavelengths longer than 600 nm, was a quarter-meter Ebert monochromator equipped with a 170-groove/mm grating blazed at 500 nm. When used to view the time-integrated down-scatter, the signal was recorded on Kodak 4143 High



Speed IR film. The spectral range was limited on the long-wavelength side to 925 nm by the fall-off in film response. The short-wavelength side was limited to 570 nm by the use of sharp-cut long-pass filters to reduce stray 527-nm light.

Three different target/observation geometries were used. The first, Figure III-2(a), had the laser normally incident onto the target and the mirrors were placed at  $135^\circ$  from the forward direction. In this case, the two spectrometers were sampling the same observation angle. The second geometry [Figure III-2(b)] had the target tilted at  $45^\circ$ . The collection mirrors were at the same angles with respect to the laser so that the down-scattered spectrum was collected from the direction normal to the target and the up-scattered spectrum was observed along the target face ( $90^\circ$  sidescatter). The third geometry [Figure III-2(c)] employed a similarly tilted target, but only one collection mirror was used, sampling along the target normal. The scattered light was directed onto the down-scatter spectrometer. A portion of this light was split off by an uncoated microscope slide that acted as a 4%-per-surface beam splitter. Only the front surface reflectance was directed onto the up-scatter spectrometer.

The use of an aluminized 10% beam splitter in place of the uncoated glass reduced the down-scatter signal below detectable levels, implying that the scattered light was polarized. Direct scattering processes, such as enhanced Thomson scattering and Raman scattering, will retain a high degree of polarization.<sup>45</sup> Secondary emission, such as mode conversion, will not be as polarized.

The IR spectra was also time-resolved for all three geometries (Figure III-3). The output of the IR spectrometer was focused onto a streak camera slit by a pair of lenses: first, a cylindrical field lens with a 400-mm focal length used to collimate the spectrometer output, and second, a convex lens with a 43-mm focal length. The streak camera and spectrometer slits were crossed to give both temporal and spectral

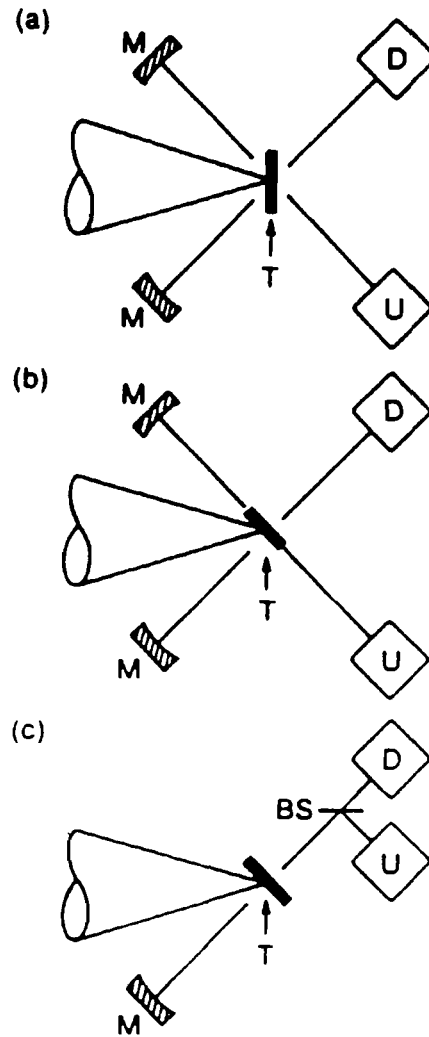


Figure III-2. Three detector/target geometries were used in the experiment. The scattered light is collected by two aluminum mirrors and focused onto the spectrometer slits with an effective f-number of 13. In (a), both the up- and down-scattering signals are observed at  $135^\circ$  from the direction of laser propagation. In (b), the target was tilted at  $45^\circ$  to the laser with the observation angles unchanged. In (c), signals were sampled in the direction of the tilted target normal. The mirrors are labeled by M, the up-scattering (UV) spectrometer by U, the down-scattering (IR) spectrometer by D, the beam splitter by BS, and the target by T.

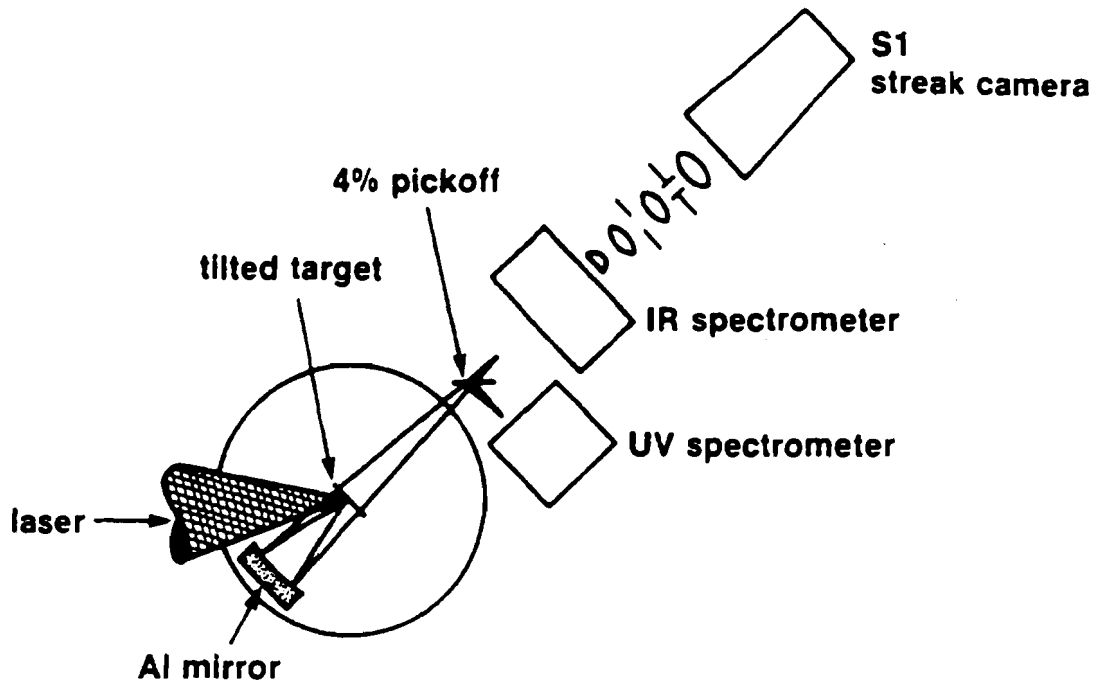


Figure III-3. Schematic layout for measuring the time-resolved down-scattering spectra. The optics between the streak camera slit and the photocathode were wavelength corrected to reduce chromatic distortion. The up-scattered signal was split off from the down-scattered by an uncoated glass slide.

resolution. The optics between the streak camera slit and the photocathode were corrected so that the effects of chromatic shifts were reduced.

An Imacon 675 streak camera, equipped with an S-1 tube whose nominal response peaked at 750 nm and fell off rapidly to either side, becoming 10 times less sensitive at 1.05  $\mu\text{m}$ , was used. The S-1 tube was very old and its long-wavelength sensitivity had changed, so that at 1  $\mu\text{m}$  the tube response was very poor. Streak data was taken at a nominal sweep speed of 100 ps/mm. Due to the finite size of the photocathode, the spectral window was limited to 450 nm with a resolution of 10 nm.

The dispersion of the spectrometer/streak camera combination was determined by directing the output of two HeNe lasers, operating at wavelengths of 628 and 543.5 nm, respectively, onto the spectrometer slit. The grating was set so that the first-order red and second-order green and red lines could be seen on the streak camera image intensifier phosphor when in focus mode. For an absolute wavelength fiducial, the IR absorber plate was removed from the incident laser beam, the lens was defocused, and low energy ( $\ll 1\text{-J}$ ) irradiances of gold targets, tilted at  $22.5^\circ$ , were taken to record the unconverted fundamental laser line. The temporal dispersion was calculated by measuring the known IR-pulse width. The data was recorded on Kodak Tri-X film, which was push processed to an equivalent ASA of at least 4,000.

To determine the electron temperature, the x-ray continuum from the target was measured and a two- or three-Maxwellian electron distribution was fit to it.<sup>43,67</sup> The x-ray detectors consisted of nine PIN diodes and six scintillator-photomultiplier tube units filtered with various K-edge filters. Caution is advised when interpreting the results of this diagnostic. The model upon which this diagnostic is based<sup>68</sup> assumes that the electrons have a multi-Maxwellian distribution, however, the detector array is not sensitive enough to test whether this assumption is valid. There is some

experimental evidence that the electrons are emitted in a nearly monoenergetic beam,<sup>42</sup> and that the x-ray continuum generated by a beam would be very similar to that generated by a Maxwellian population<sup>59</sup> so that the actual temperatures deduced would not change appreciably. In this dissertation, the standard, multi-Maxwellian results will be used.

Two other caveats should be noted. The first is that the x-ray continuum instrument collects the time- and space-integrated signal; no information about the exact electron temperatures at any point in space or time is gained. The second caveat is that the method used to define the energy window of each detector, K-edge filtering, is an inherently wide-bandwidth method. That is, the filters define a rather narrow band at their K-edge, but the filter is essentially transparent to x rays with a much higher energy. This high-energy window is only cut off by the detector's inability to measure such higher-energy x rays. Therefore, the signal at a particular energy may be measured by several different detectors. This must be taken into consideration in the data reduction routine<sup>43,67</sup> by finding a self-consistent fit, assuming the multi-Maxwellian distribution and given the measured signal.

In this experiment, the best results were obtained assuming a two-temperature model with cold and superhot temperature components. The former is characteristic of the dense plasma near  $n_c$ , while the latter is characteristic of electrons generated by nonlinear processes involving plasma waves at or below  $n_c/4$ . A third, or hot component, which is characteristic of interaction phenomena near  $n_c$  (resonance absorption and/or the parametric decay instability) was not observed because its x-ray signal was too weak. A typical reduction of the experimental data is shown in Figure III-4. The large scatter is caused by uncertainties in the energy window of each detector. It should be emphasized that this temperature measurement is independent of

## Electron Spectrum: Shot 12038

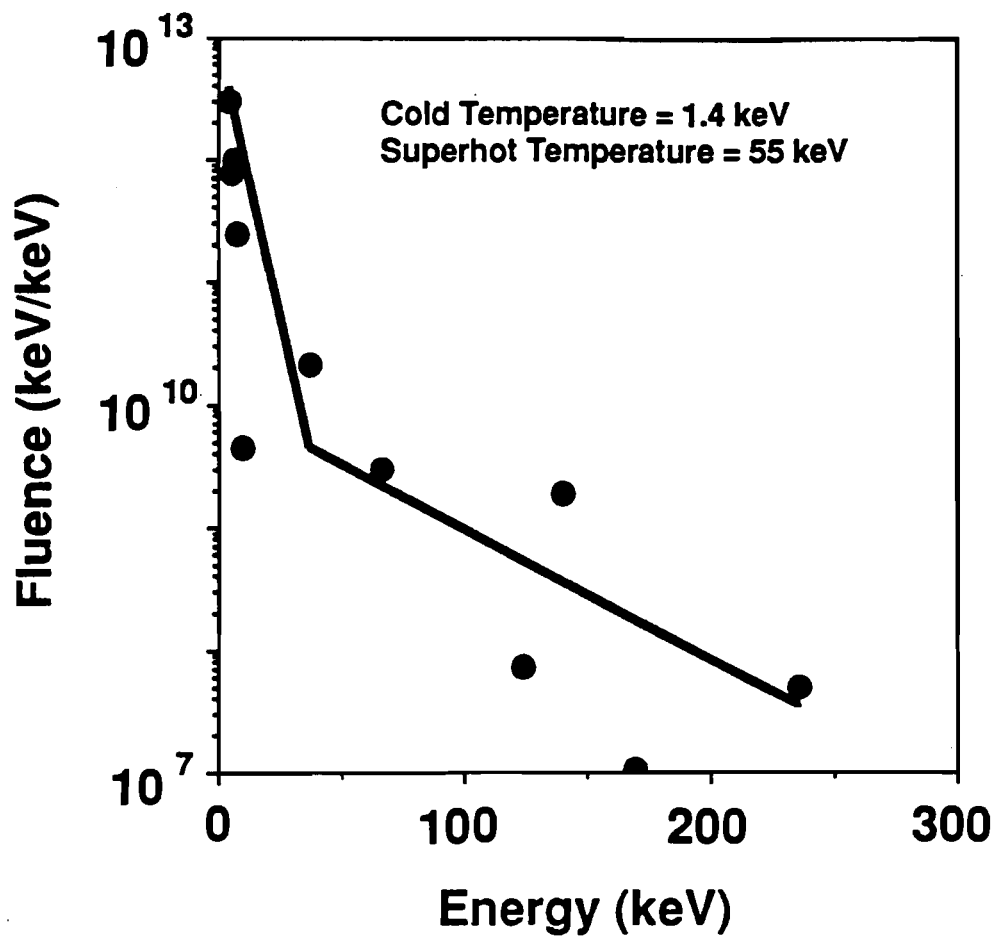


Figure III-4. A typical fit for the x-ray continuum diagnostic.

scattered light measurements.

## B. Results

The results of the time-integrated experiments using the geometry of Figure III-2(a) are reported first. The observation angles were both  $135^\circ$ , so the observations are affected by refraction, especially the down-scatter measurement. Refraction of scattered light waves originating at different densities is included in the enhanced Thomson scattering calculations. Figure III-5 shows three typical spectra. As the incident intensity was increased from  $7 \times 10^{13}$  to  $4 \times 10^{15}$  W/cm<sup>2</sup> (which would correspond to raising the superhot-electron temperature), the long-wavelength shoulder increases in intensity and its long-wavelength cutoff increases. The long-wavelength sensitivity of this data is limited because of the extremely sharp cutoff, 925 nm, of the Kodak 4143 film used. A discussion of the various films used in these experiments is contained in Appendix B. Up-scattering spectra from this illumination geometry are shown in Figure III-6.

From the presence of the double-peaked  $3\omega_0/2$  feature, a signature of the two plasmon decay instability, on all of the up-scattering data taken, it may be inferred that superhot electrons were present. For example, in Figure III-6, stray 351-nm-laser light has obscured one peak of the three-halves feature, but the presence of the total feature is evident. Also apparent in Figure III-6 are two up-scattering bands: one at a shorter wavelength than the  $3\omega_0/2$  signal and one at longer wavelengths. Since the amount of 351-nm energy on target was very small ( $\ll 1$  J), it had no effect on the interaction. In later experiments (Figures III-11 and III-12), the residual 351-nm light was completely eliminated. The two up-scattering features are distinctly separated from the three-halves

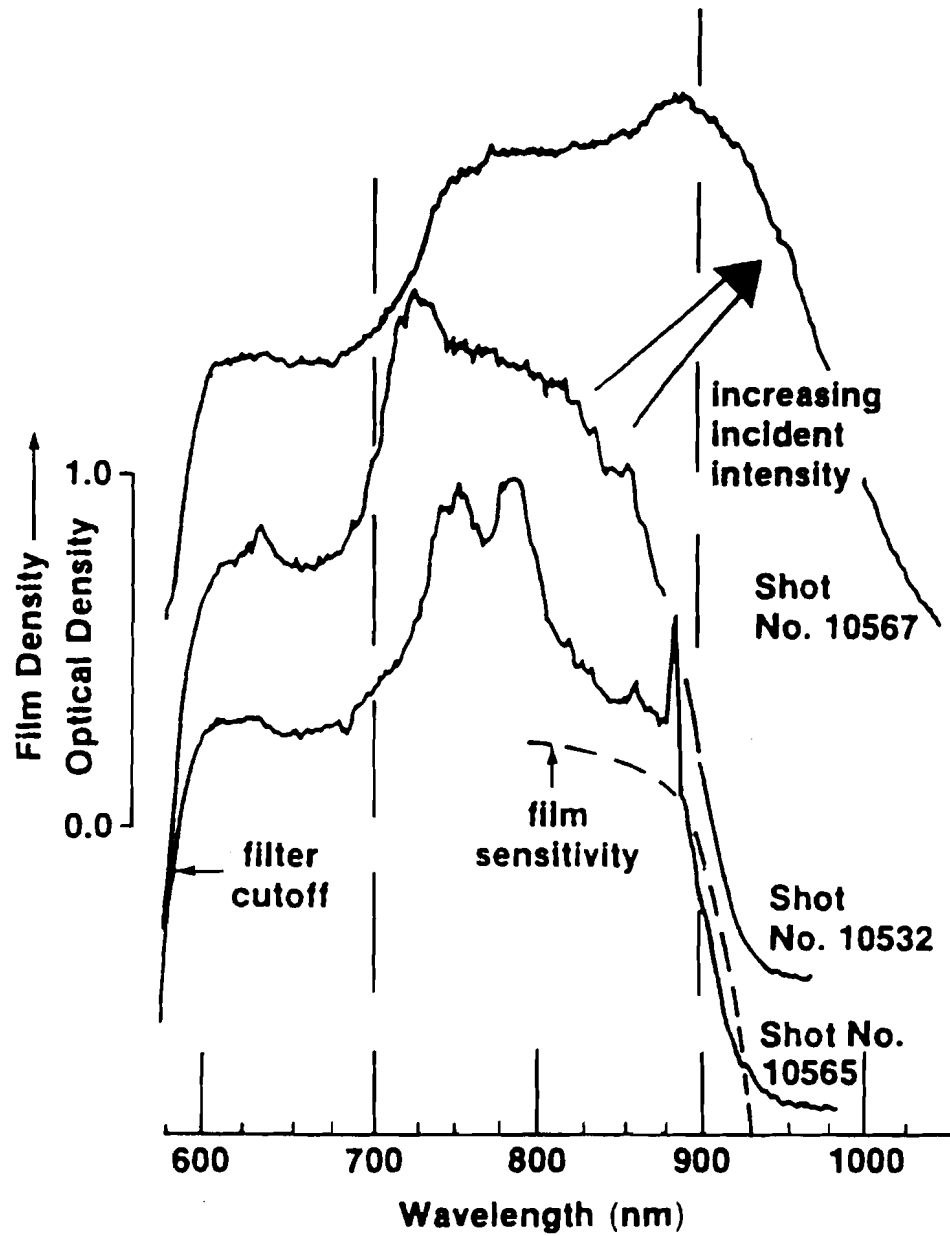


Figure III-5. Time-integrated down-scattering spectra arranged in order of increasing incident intensity. The spectral window was limited to  $570 < \lambda < 925$  nm by cutoff filters at 570 nm and by the film sensitivity at 925 nm.



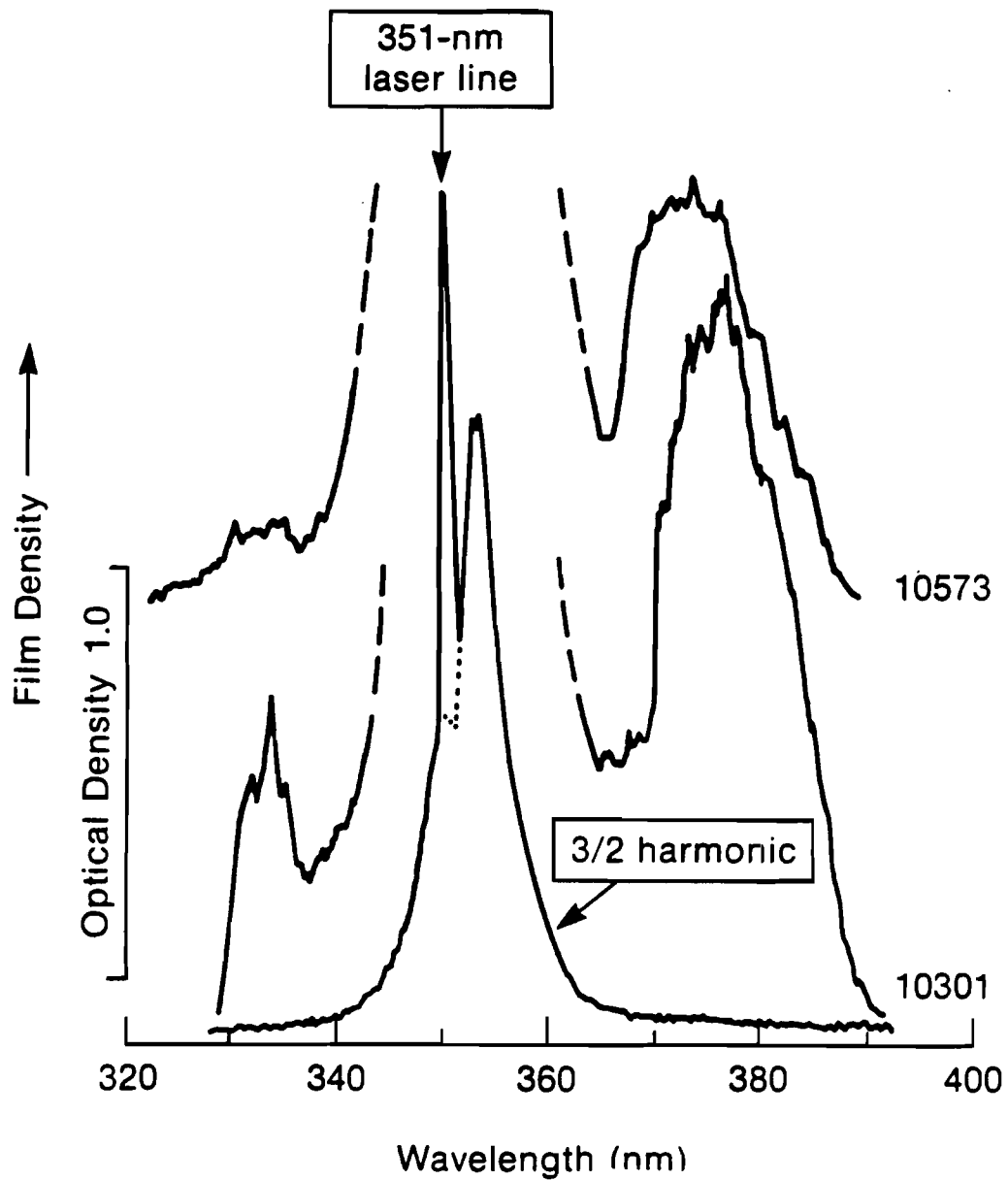


Figure III-6. Up-scattering spectra showing the  $3\omega_0/2$  signal and two ETS features that arise from a hot component of the electron temperature distribution at 8 to 10 keV and a superhot component at 25 to 30 keV.

spectrum, one to either side. Because of experimental problems in this geometry, no down-scattering measurements were taken on the shots on which the up-scattering was measured (Figure III-6). However, Figure III-5 shows that the down-scattering consistently appears in the same spectral range. If it is assumed that the spectra presented in these two figures are typical and that the gross placement of these bands is reproducible, they can be fit using the enhanced Thomson scattering theory, as shown in Figure III-7. Estimates of the electron temperatures had to be made since no x-ray temperature measurements were made for these irradiances. The hot and superhot temperatures were estimated to be 7 and 30 keV, respectively, which are consistent with later measurements. By choosing suitable hot-electron fractions, the observed spectra of two up-scattered peaks straddling the three-halves feature and a down-scattered feature near 700 nm can be self-consistently reproduced. The fourth predicted band, above 900 nm, was not observed due to the lack of film sensitivity, except for one irradiance (number 10567 in Figure III-5) that was extremely intense and overexposed the film.

Using the same geometry [Figure III-2(a)], the down-scattering signal was time-resolved, as shown in Figure III-8. The "time-integrated" signal, calculated by averaging the streaked spectra over time at each wavelength, shows the down-scattering observed at 900 nm and the familiar double-peaked  $\omega_0/2$  feature. By carefully inspecting the time-resolved portion of Figure III-8, it is evident that the down-scattering band extends from 900 to 980 nm, in good agreement with Figure III-7. The majority of the scattered-light intensity, however, is in a band that is less than 40 nm wide. Due to instrumental restrictions, no data below 800 nm was taken for this series of experiments, and no attempt was made to correct the spectra for the frequency response of the detector assembly. The time-resolved picture shows that the  $\omega_0/2$

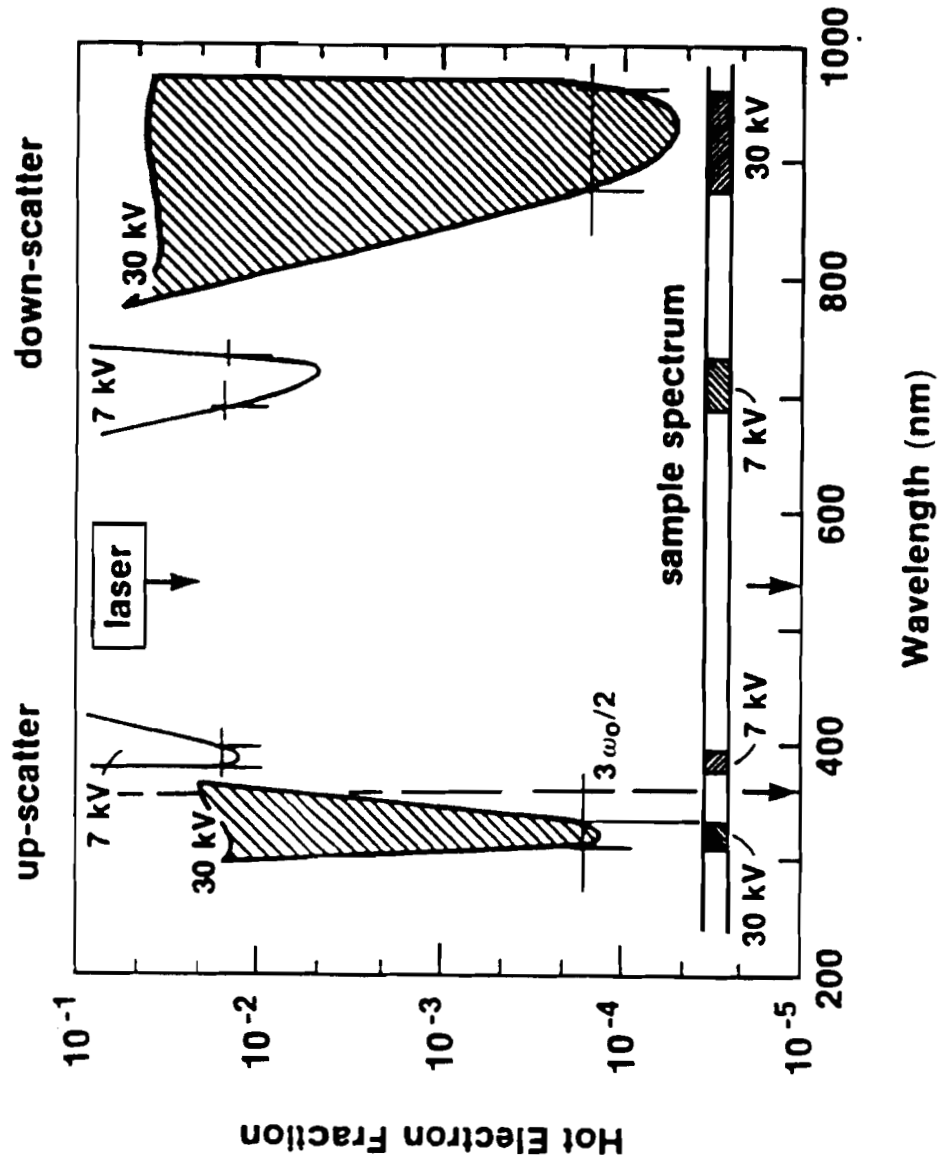
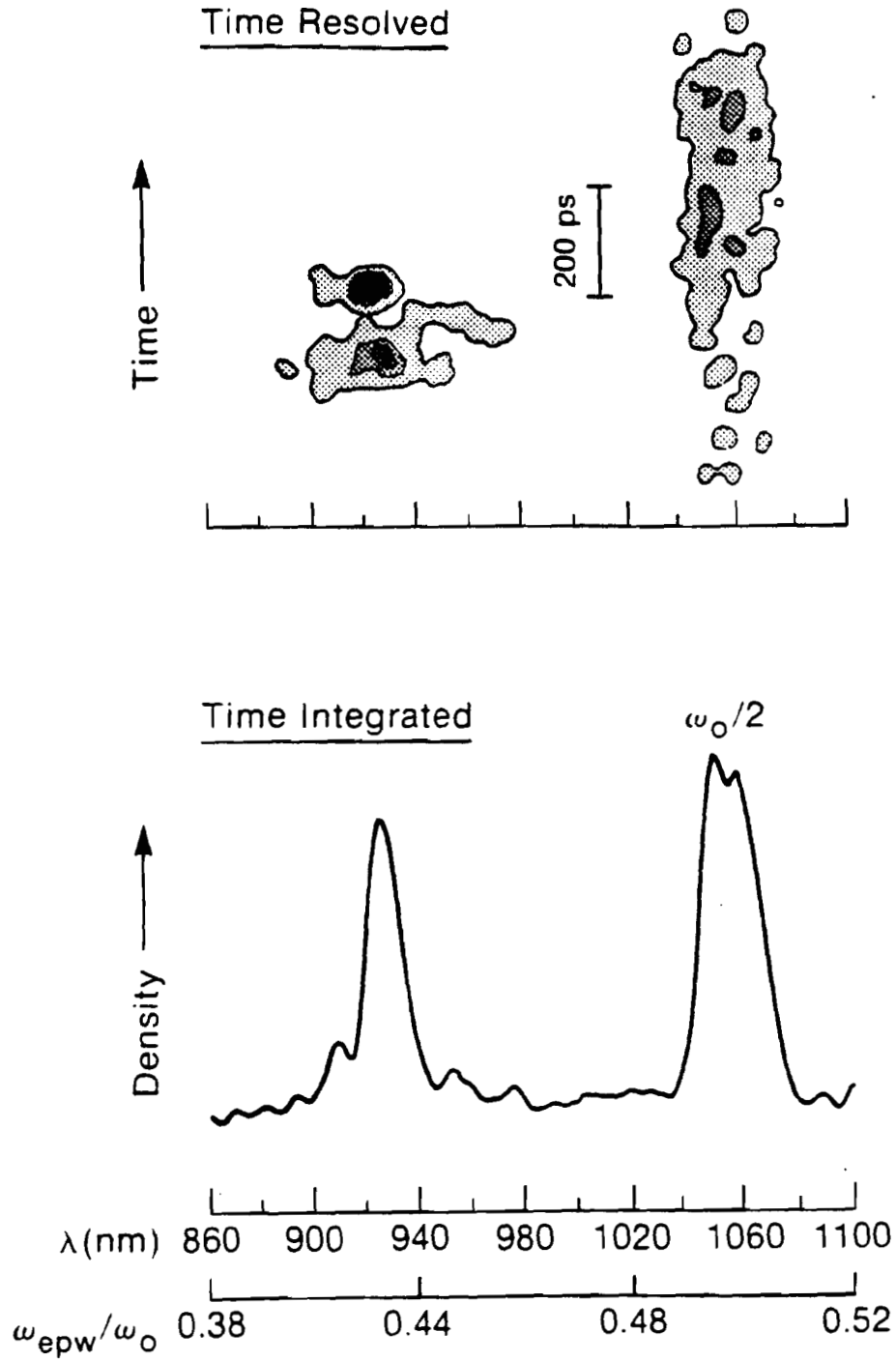


Figure III-7. Predicted ETS spectral bands for electron temperature components of 1, 7, and 30 keV. The angle of observation is  $45^\circ$ ; the target is normal to the laser and has  $Z = 3$ . Refraction of the outgoing ETS light is taken into account using a planar plasma blow-off geometry.



**Figure III-8.** Time-resolved down-scattering spectra. The average intensity was  $1 \times 10^{15} \text{ W/cm}^2$  in a 1-ns pulse. Note that the  $\omega_0/2$  signal turns on before the ETS signal.

signal turns on well before the ETS signal, as expected if TPD creates the  $\omega_0/2$  signal and the superfast electrons that seed the ETS signal. The down-scattering is of very short duration—less than 200 ps—and turns itself on and off at least twice. In most of the experiments using this geometry, the  $\omega_0/2$  feature was not observed; in many of the irradiances, however, the down-scattering was evident and had the same sort of temporal history as shown in this figure.

The half-harmonic signal was not consistently observed for three reasons. First, the  $\omega_0/2$  emission was strongly peaked in the direction of the density gradient, which was not the same as the direction of observation. Second, whatever  $\omega_0/2$  signal was emitted in the observed direction would be strongly refracted. Finally, since an old S-1 streak tube was used, its sensitivity to 1- $\mu\text{m}$  light was very low.

The experiments using the geometry described by Figure III-2(b) were less illuminating. No up-scatter signal was observed at all, primarily because the observations were at  $90^\circ$  from the density gradient. The ETS theory predicts up-scattering signals in this geometry only for  $T_{sh} > 60$  keV and then only for extremely large hot-electron fractions (of the order of 10%). The down-scattering data was similar to the following, since the down-scattering geometries were the same.

A series of experiments was conducted using the geometry depicted in Figure III-2(c). In this geometry, simultaneous observations were made of the up- and down-scattering in the same direction, along the target normal, which, to a good approximation, may be assumed to be the direction of the density gradient. Two down-scattered spectra are presented in Figure III-9. On both, the large  $\omega_0/2$  signal can be seen because refraction has been minimized by the choice of target orientation. The absence of the  $\omega_0/2$  splitting is attributed to saturation of the streak camera photocathode and the S-1 aging problem already discussed. The position of the

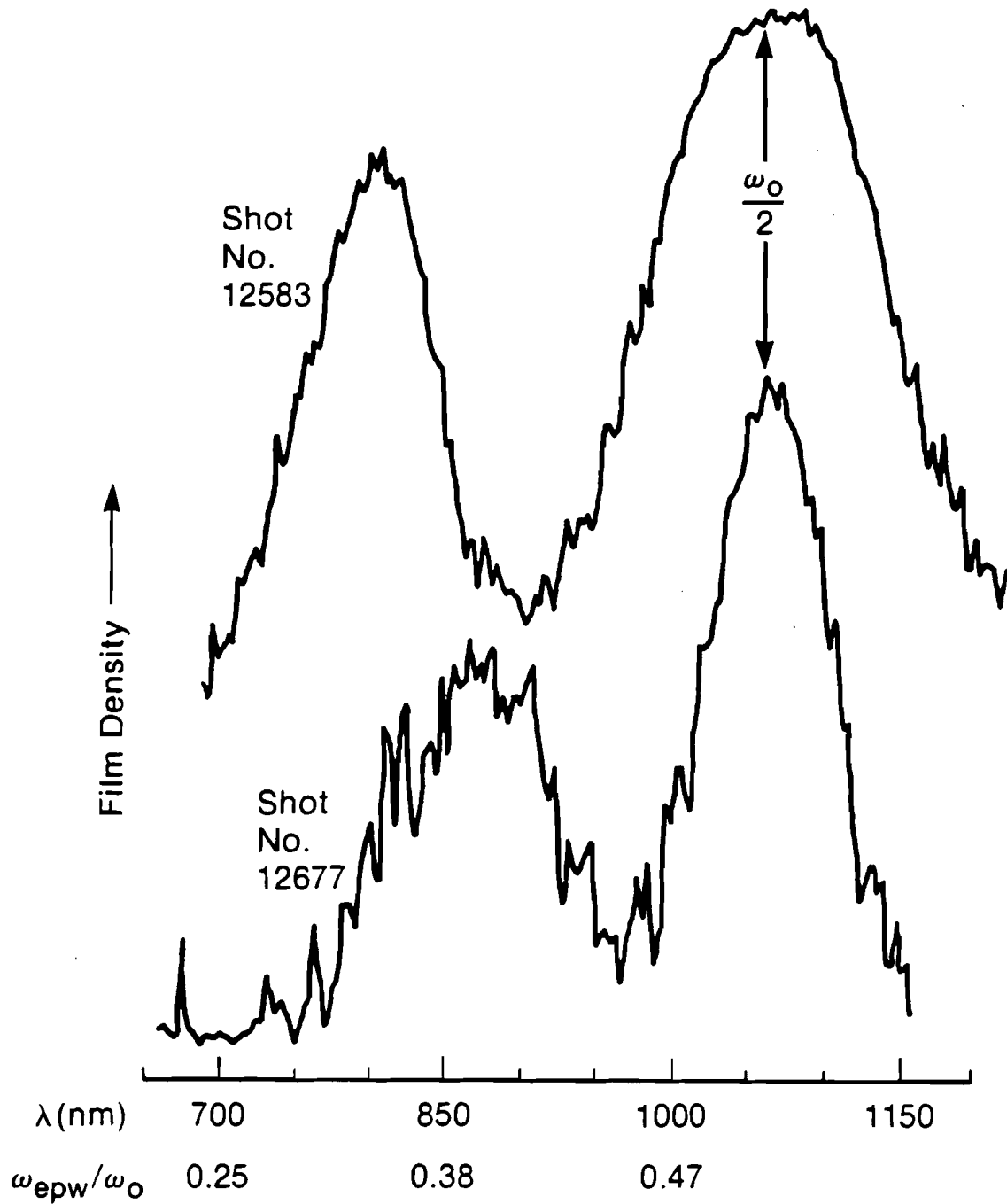


Figure III-9. Down-scattered spectra for the same average incident intensity and measured electron temperature. The variations in the position of the bands is attributed to varying hot spots in the incident laser.

down-scattering peak is different for these two shots, even though the average intensities ( $8 \times 10^{14} \text{ W/cm}^2$ ) and measured superhot-electron temperatures are the same.

These differences are attributed to hot spots in the on-target energy distribution, which varies from irradiance to irradiance due to air turbulence in the laser-beam path. The 50-nm shift between the two down-scattered spectra in Figure III-9 is consistent with a superhot-electron temperature change of less than 10 keV, well within the experimental uncertainty of the electron-temperature diagnostic. Although not observed on the same shots as Figure III-9, a 10-keV temperature change would correspond to a 10- to 20-nm wavelength shift of the up-scattered band. The poor dynamic range of the recording film (see Appendix B) would make a shift of this magnitude difficult to measure because the full-width of the band is not detected. A shift of the wavelength corresponding to the peak scattered intensity is not a conclusive signature of a shift of the entire band because there are, as yet, no theoretical predictions of the detailed spectral shape of each band. The hot spots dominate the interaction process described here, especially in terms of the superhot-electron production and consequently the enhanced Thomson scattering signal. The uncertainty in the superhot-electron temperatures is greater than the variation in temperature needed to explain the observed spectra.

The temporal history of this irradiance, as shown in Figure III-10, is similar to Figure III-8, showing that the same process is being observed. The ETS signal is of shorter duration (200 ps) than the  $\omega_p/2$  signal (700 ps). The half-harmonic signal turns on first and the down-scattering occurs near its peak.

An up-scattering spectrum taken in this same geometry (Figure III-11) shows the two peaks associated with ETS. The shorter-wavelength peak, identified with

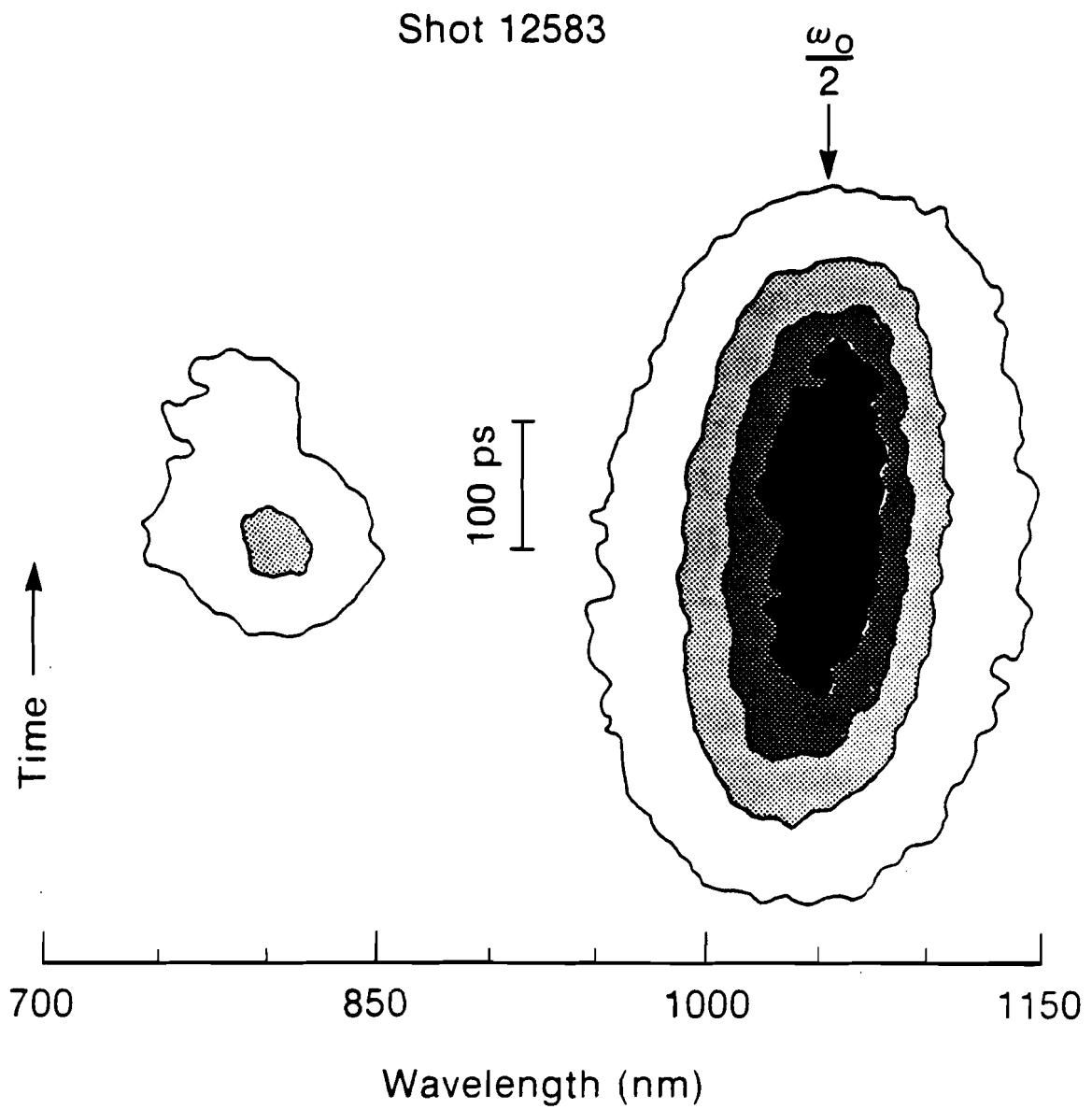


Figure III-10. Typical time evolution of the down-scattering spectra, which begins near the peak of the  $\omega_0/2$  emission and lasts for about 200 ps. The contours are at 10, 40, 70, and 90% of peak intensity.



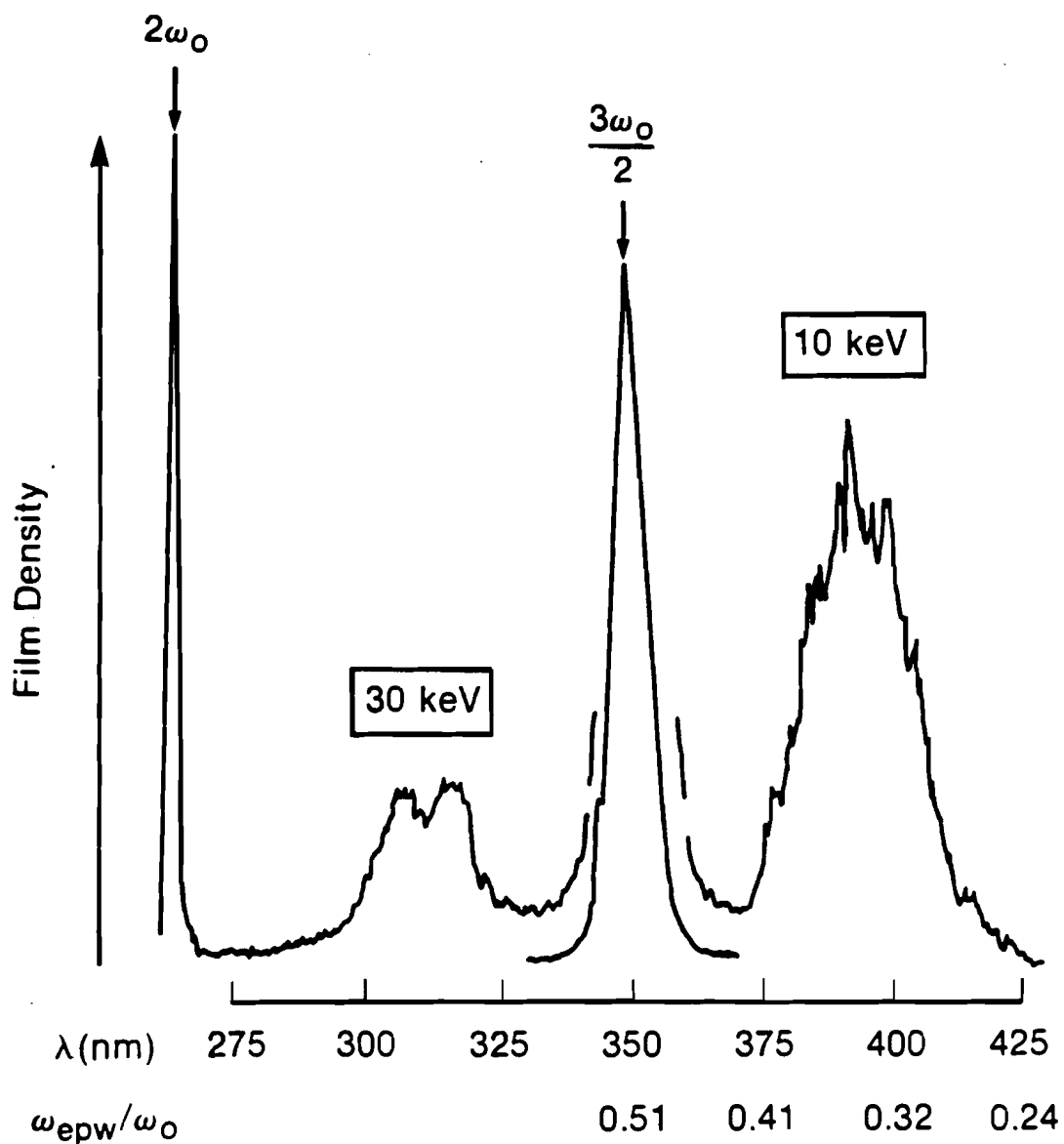


Figure III-11. Up-scattering spectrum observed along the density gradient for the geometry of Figure III-2(a). The two up-scattering features on either side of the  $3\omega_0/2$  peak reflect two electron temperature components with  $T_h = 10$  keV and  $T_{sh} = 30$  keV.

superhot electrons, occurs between  $3\omega_0/2$  and  $2\omega_0$ . The longer-wavelength peak, due to hot electrons, occurs near 400 nm. The latter has been observed regularly in these experiments, while the former was only rarely visible. The absence of this peak is due presumably to an insufficient number of superfast electrons to produce this band, even though there were enough superfast electrons to produce a measurable x-ray signal.

A complete description for one particular irradiance is presented in Figure III-12. This irradiance had a measured average intensity of  $7 \times 10^{14}$  W/cm<sup>2</sup> and a measured superhot-electron temperature of 17 keV. A better theoretical fit was found using a superhot-temperature of 30 keV, which is reasonable considering the uncertainties in the temperature diagnostic. A superhot-electron fraction of 1% was found by comparing the measured down-scatter band with Figure III-13. This predicts an up-scatter band between 290 and 350 nm, which corresponds very well with the measured peak. Since there was no direct measurement of the hot-electron temperature, a temperature of 10 keV was assumed and the second up-scatter band, at a wavelength longer than 351 nm, was fit with a hot-electron fraction of 1%. This value is below the threshold for down-scattering, which is consistent with the observation of only a single down-scattering band (from superhot electrons). Therefore, a complete set of data can be self-consistently explained using the ETS theory.

### C. Discussion

The enhanced Thomson scattering theory describes the results very well for those irradiances in which a nearly complete set of experimentally measured parameters could be obtained. However, in other instances one or more of the predicted peaks was missing, especially the shorter-wavelength down-scattering band which is associated

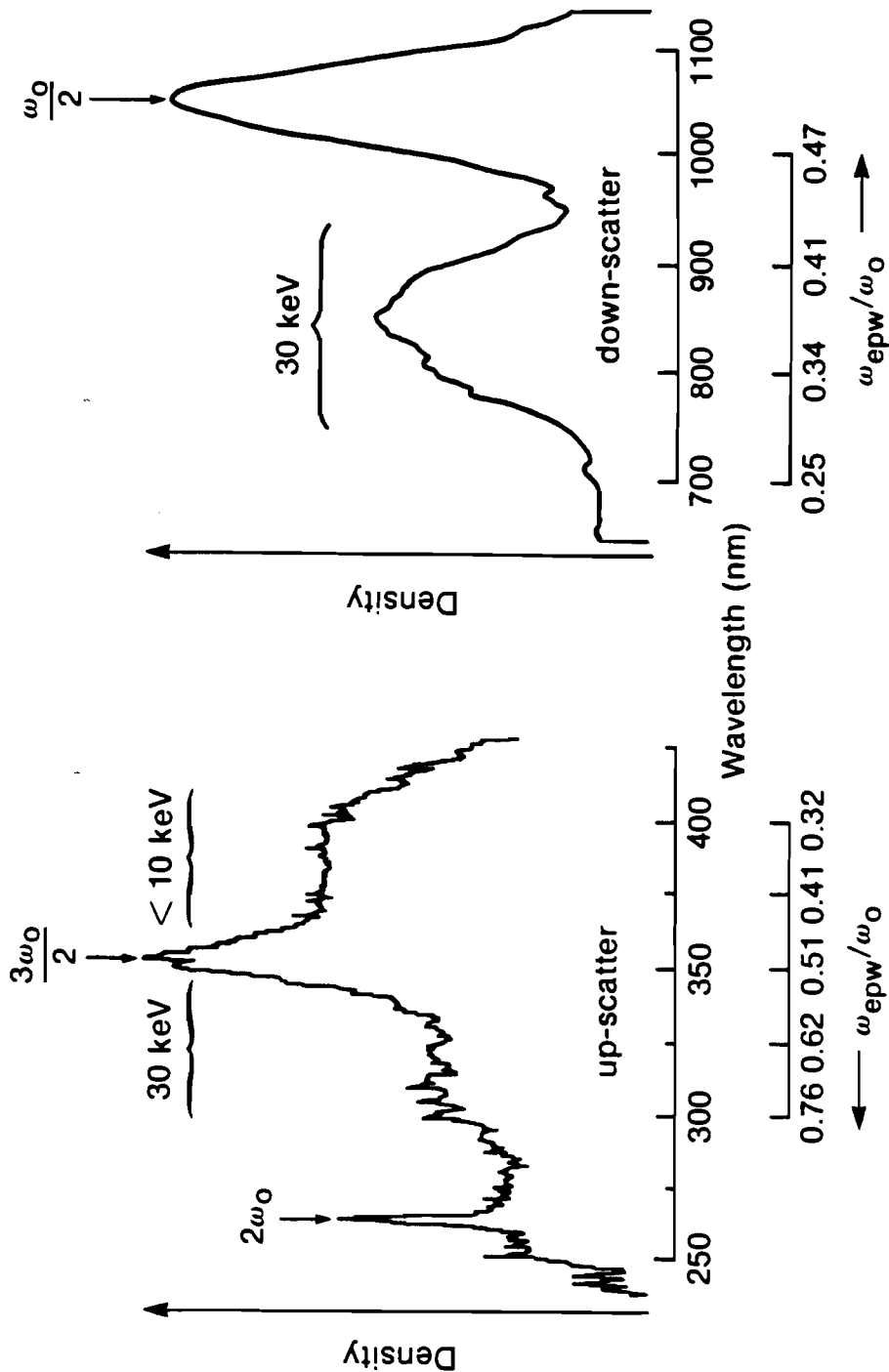


Figure III-12. Simultaneous up- and down-scattering spectra. The measured electron temperatures for this irradiance were  $T_c = 1.0$  and  $T_{sh} = 17$  keV. No hot x-ray component was observed for this irradiance by the x-ray temperature diagnostic, presumably due to insufficient signal emitted by this component relative to the other temperature components. The incident intensity was  $6 \times 10^{14}$  W/cm<sup>2</sup> in a 600-ps pulse.

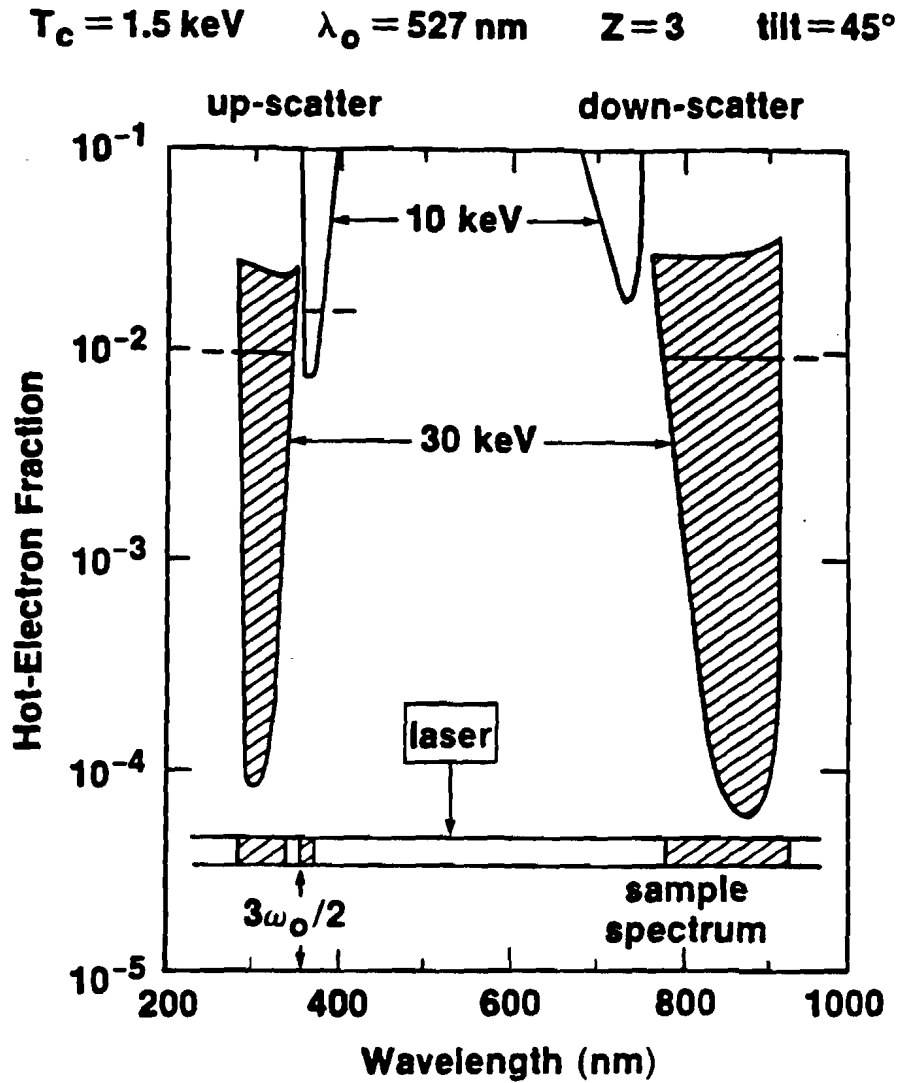


Figure III-13. Predicted enhanced Thomson scattering bands as observed in the direction normal to the target, assuming a three component temperature distribution with  $T_c = 1.5$ ,  $T_h = 10$ , and  $T_{sh} = 30$  keV. The target is tilted at  $45^\circ$  and has  $Z = 3$ . The laser wavelength is 527 nm. The sample spectrum is for a hot-electron fraction of 1% and a superhot-electron fraction of 8%.

with the hot (but not the superhot) electrons. This may be due to the hot-electron fraction not exceeding the threshold needed for enhanced scattering. At other times, the up-scattering band associated with the superhot electrons was also absent, presumably for similar reasons. The lack of sufficient numbers of hot or superhot electrons may be connected to the lack of hot spots in the laser-beam intensity pattern where the thresholds of suprathermal electron-generating instabilities may be more easily satisfied. Since only a limited amount of energy was available, the enhancement of the electron-plasma waves necessary to produce detectable scattering could only be reached in hot spots of the laser beam where the peak intensity could be many times the average intensity. It can be inferred from these measurements that the random distribution of hot spots, presumably due to air turbulence, is responsible for the infrequent appearance of the short-wavelength up-scatter band. The shift in the down-scatter bands is consistent with small changes of the superhot-electron temperature while the position of the up-scattering band is consistent with either approach.

Convective stimulated Raman scattering (SRS-C)<sup>62</sup> could be invoked to explain the existence of some of the scattered features that were observed. As discussed in Chapter II, this interaction takes place in the plasma corona at densities below quarter-critical. According to this theory, the signature is a scattering band that should extend from the half-harmonic of the laser up to a higher frequency, where it is cut off by Landau damping (i.e., near  $k\lambda_D \approx 0.2$ ). Density steepening at the quarter-critical surface must be invoked to explain the "gap" which appears between the down-scattering band and the  $\omega_0/2$  feature. In addition, the theoretical threshold for SRS-C is usually not exceeded in the intensity region where down-scattering has been seen.<sup>13</sup> The SRS-C threshold is not reached in these experiments, even for 8:1 hot spots, which are more intense than those thought to exist in the GDL beam. Stimulated

Raman scattering may occur in filaments at intensities below the SRS threshold,<sup>66</sup> but the multi-peaked spectrum, characteristic of this process, was not observed.

Stokes mixing has been suggested as an explanation for the existence of both up- and down-scattering bands<sup>50</sup> because the conditions for the SRS instability also allow coupling to a fourth anti-Stokes EM wave at  $\omega_s' = \omega_0 + \omega_{epw}$ . Normally, the amplitude of this wave is small since it is non-resonant. At low plasma densities, and for scattering in the forward direction, the degree of off-resonance is reduced, and an appreciable level can be reached. Note, however, that the frequency of this wave lies above the laser frequency by the same amount as the down-scattered wave is below it, and cannot exceed  $3\omega_0/2$ . Since the dispersion relation for the up-scattered EM wave will not be satisfied at the density where the instability occurs, some propagation of the plasma wave toward a different density will have to be invoked so that the scattered wave will be observable.

The observations cannot be explained by Stokes mixing since (a) the scattering bands were not symmetric (see Figure III-12 where a scale in terms of  $\omega_{epw}/\omega_0$  has been added for convenience), (b) spectral features above the three-halves harmonic were observed (Figures III-6 and III-11) (a region inaccessible to Stokes mixing), and (c) the observations in the backscatter direction are incompatible with the resonant condition for up-scattered light since the plasmon wave vector would be too large.

#### D. Summary

A series of experiments was conducted to observe the scattered light spectrum from a 527-nm laser-produced plasma. Three features were observed: one was down-scattered from the laser frequency and two were up-scattered, one on either side

of the three-halves feature. Using several different irradiation and observation geometries, the down-scattered spectra was temporally resolved. In addition, the continuum x-ray spectra was independently measured and corresponding electron temperatures were determined. Good agreement with the enhanced Thomson scattering model was found if it was assumed that the electron velocity distribution can be described by three components: a cold Maxwellian background with  $T_c \approx 1.5$  keV, a hot directed beam (moving both up and down the density gradient) created as a by-product of resonance absorption or the parametric decay instability at  $n_c$  with " $T_h$ "  $< 10$  keV, and a superhot directed beam (again, moving up and down the density gradient) created by either the two plasmon decay instability or the absolute SRS instability at  $n_c/4$  with " $T_{sh}$ "  $> 15$  keV. The presence of hot electrons from resonance absorption could be inferred from the scattered light spectrum even though the x-ray diagnostic was not sensitive enough to detect them. The appearance of hot spots of greater than average intensity in the laser beam had to be invoked in order to explain shot-to-shot variations in the spectral position of the down-scattered band. These variations were not observed in the up-scattered spectrum, possibly due to the poor dynamic range of the recording film used. It was also shown that convective stimulated Raman scattering, or the anti-Stokes component of SRS, does not provide an adequate explanation of the observed spectra.

## Chapter IV: Long-Scale-Length Experiments

There are many differences between the single-beam GDL system and the multi-beam systems envisaged for commercial ICF power plants. The three principal differences in the laser-driver are the wavelength, energy, and pulse duration. The laser wavelength must be less than  $0.53 \mu\text{m}$  to avoid the creation of “fast,” or “hot” electrons that preheat the fusion fuel and prevent efficient compression. The energy must be high to implode the large fuel pellets to be used in power plants, and the pulse duration must be long to reduce the fluence, or intensity per unit area, on the optical elements of the laser system.

A long laser pulse incident on a large target will produce a large plasma, with a scale length,  $L$  ( $\equiv n/[\partial n/\partial x]$ ), of about 10,000 laser wavelengths. The simulation of an intense “interaction” beam with a long-scale-length plasma was the goal of an experimental series conducted on the Nova laser system at Lawrence Livermore National Laboratory. A complete set of diagnostics was available to test the enhanced Thomson scattering theory in a long-scale-length plasma, more typical of a reactor-type interaction than were the experiments on GDL. The diagnostics were time-resolved optical spectrometers, one tuned to the spectra between  $\omega_0$  and  $\omega_0/2$ , and one to measure the up-scattering spectra. Electron-temperature measurements were also made.

This chapter describes those experiments, beginning with a brief description of the Nova laser system (more detail follows in Appendix C) and the method used to produce a long-scale-length plasma. Also, the diagnostics deployed in this experiment are briefly discussed (with more detailed descriptions in Appendix C). Results from the three primary diagnostics are then presented and the spectra from “interaction” shots



and “null” shots (where the “interaction” beam is not fired) are compared. The ETS theory is shown to be in agreement with the experiments while alternate explanations fail to be adequate descriptions. Finally, the key results of these experiments are summarized.

## A. Experiment

The Nova laser system is the most powerful in the world. Located at Lawrence Livermore National Laboratory, Nova was designed to “address critical issues for evaluating the feasibility of inertial confinement fusion ... and to perform a wide range of high energy density plasma physics experiments.”<sup>69</sup> The ten-beam laser has a master oscillator power amplifier structure operating at a wavelength of 1.054  $\mu\text{m}$ . Several different oscillators are used to produce pulses that vary in duration (100 ps to several ns) and temporal shape (Gaussian, square, or “picket fence”). The amplifier chain consists of many stages of rod and disk amplifiers; the final disk amplifier is 46 cm in diameter. Each beam is then expanded to 74 cm and frequency doubled (to 0.53  $\mu\text{m}$ ) or tripled (to 0.35  $\mu\text{m}$ ) before being focused onto the target with  $f/4$  lenses to a minimum spot diameter of 100  $\mu\text{m}$ . The maximum energy of each beam is 15 kJ. The ten beams are divided into “West” and “East” clusters of five beams each. One cluster enters the target chamber from each side, with the five beams equally spaced around a cone with an opening angle of 100°. The two cones are rotated with respect to each other so that no two beams are directly counter propagating.

Beam timing is adjusted with optical-trombone delay lines. There is one for each cluster and then another for each beam. Relative timing changes are verified with two streak cameras equipped with CCD cameras for real-time monitoring. Each streak

camera monitors the five beams of a cluster, a fiducial for absolute synchronization, and a comb generator used for temporal dispersion calibration. A third streak camera monitors the master oscillator pulse, a fiducial, and a comb generator.

When these experiments were performed, the maximum amount of 1.054- $\mu\text{m}$  energy was limited to 80 kJ by platinum inclusions in the disk-amplifier glass. Consequently, the maximum third-harmonic, on-target energy was 20 kJ in a 2-ns-long square pulse. Because of the long cooling time of the disk amplifiers at the end of the amplifier chain, the repetition rate of the entire system was limited to two full-system shots and one partial-system shot per twelve-hour workday.

The plan of the experiments was to use nine of the Nova beams as low intensity, "heating" beams to create a long-scale-length plasma and to then use the tenth beam as a time-delayed, high-intensity, "interaction" beam. Specifically, the goal was to create a plasma with an on-axis scale length of 5,000 laser wavelengths at one-tenth critical at the beginning of the interaction beam pulse. This goal was a compromise between the desire to simulate a reactor plasma that will have a scale length of 10,000  $\lambda_0$  and limits imposed by the maximum amount of delay available in each beam line. The scale length was estimated using the similarity solutions of the ideal hydrodynamic equations as derived by London and Rosen<sup>70</sup> with the experimental parameters of laser intensity, pulse duration, target thickness, and target composition as initial conditions. No experimental data was taken to confirm this estimate.

The optical delays were set as shown in Figure IV-1. The west cluster reached the target first, with all five beams timed to arrive simultaneously. Four of the east beams were fired after a delay of 1.3 ns. The fifth, or interaction beam, was further delayed to arrive at the target 2.7 ns after the west beams. The timing was verified by comparing the shift between the fiducial and the leading edge of the pulse from each

## Nova System Timing

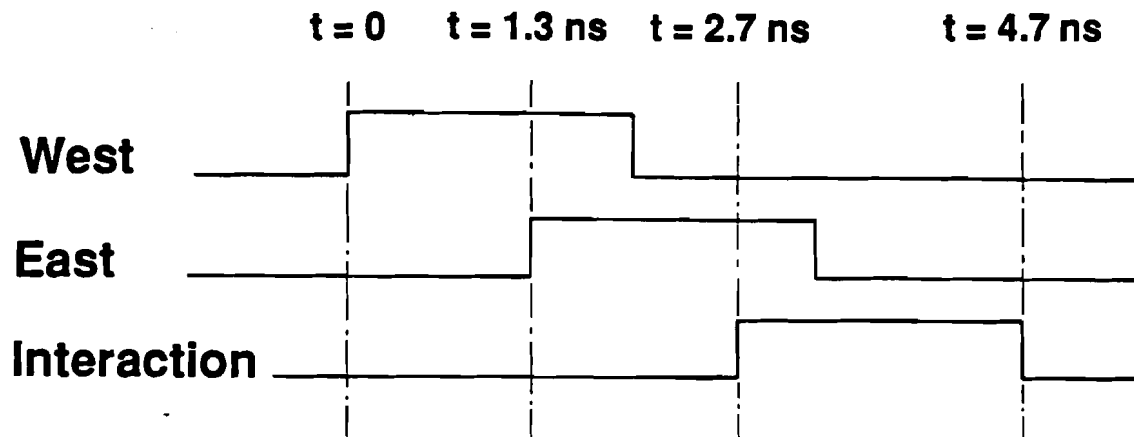


Figure IV-1. The cluster and beam timing offsets were designed to produce a long-scale-length plasma. The square laser pulse was 2 ns wide with 100-ps rising and falling edges.

beam from a long-scale-length shot with the shift from an implosion shot. The implosion shot was intended to have each beam arrive at the target simultaneously, but the accuracy of the timing on this reference shot was not known.

All of the beams were focused ahead of the target so that each beam was diverging at the target plane. Because a lower intensity was desired from the heating beams, they were purposefully defocused to give a spot size of 650  $\mu\text{m}$ . The interaction beam was more tightly focused to a 250- $\mu\text{m}$  spot size. The intensity in the overlap region was approximated by simply summing the intensity of each beam at the target plane. The target was placed perpendicular to the axis of the two cones so that each beam (including the interaction beam) was at a 50° angle to the target normal, as shown in Figure IV-2.

The 0.351-nm on-target intensity was  $1 \times 10^{15}$  W/cm<sup>2</sup> on the west side of the target. Since there were only four heating beams on the east side, the intensity was  $8 \times 10^{14}$  W/cm<sup>2</sup>. The more tightly focused interaction beam had an intensity of  $1.6 \times 10^{15}$  W/cm<sup>2</sup>.

The targets were thin CH foils that were stretched between two wires. The first target tried was 12  $\mu\text{m}$  thick. The short-wavelength edge of the down-scattered spectrum showed decreasing and then increasing densities of the scattering sites. These inconsistencies were not understood and caused a switch to 15- $\mu\text{m}$ -thick targets, which eliminated the inconsistencies and gave a longer scale-length plasma. Plastic foils were used because a low-density laser plasma will expand faster, thereby giving a longer scale length. Also, reactor targets are projected to have a plastic outer layer.<sup>71</sup>

The main diagnostics for this experiment were SOS-I and SOS-II. (The acronym stands for Streaked Optical Spectrometer.) Each SOS was a 0.22-m spectrometer with the spectra time resolved by an optical streak camera of Livermore

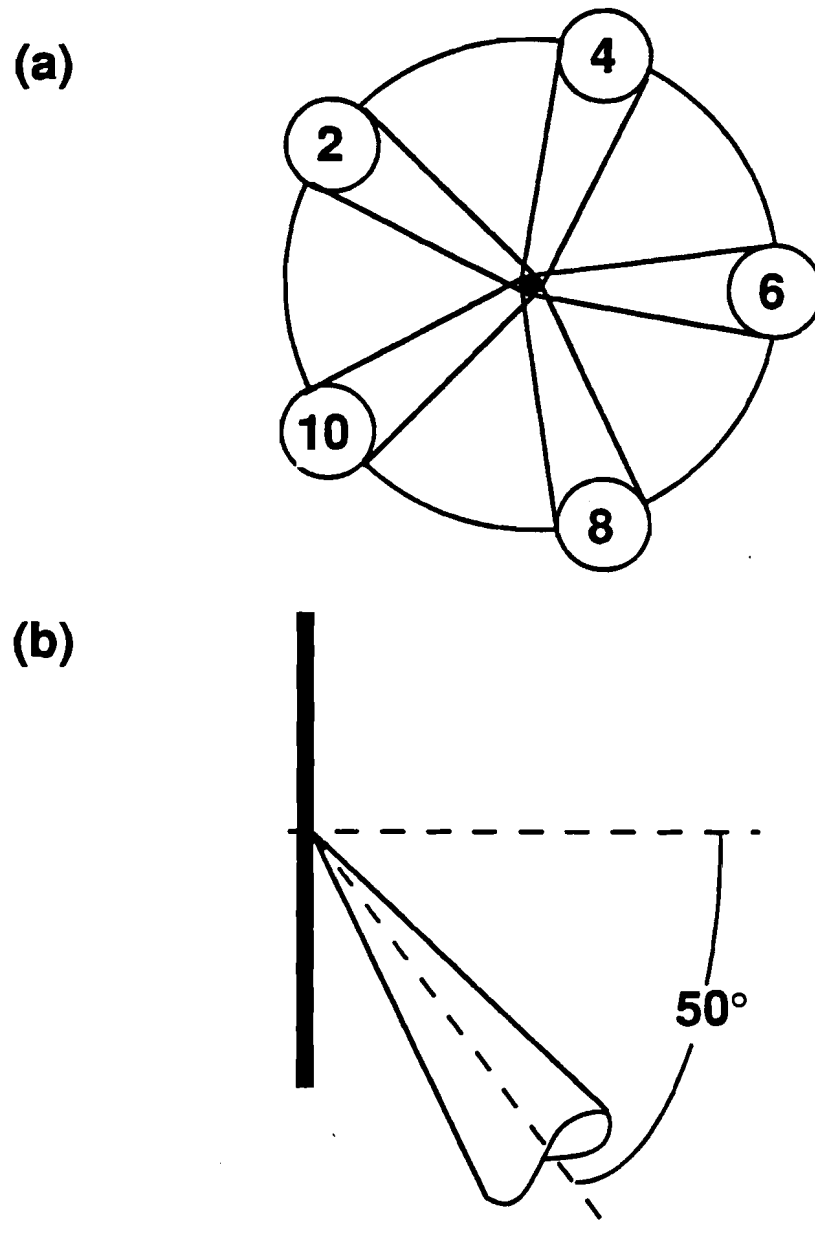


Figure IV-2. The heating beams struck the target from both sides. The beams were each  $50^\circ$  from the target normal.

design. Each camera had a time resolution of approximately 100 ps.<sup>72</sup> The spectrometers were on the east side of the chamber, each at an angle of 25° from the target normal and 27° from the interaction beam (i.e., 27° from the backscattered direction). Thus, each spectrometer (Figure IV-3) was out of the plane determined by the target normal and the interaction beam, but the two were symmetrically located. The two spectrometers did not have a common absolute temporal reference, but a reasonable approximation about their relative timing was made by assuming that the up-scattering began when the east beams were fired. This led to consistent temporal histories for both spectra.

SOS-II was designated the up-scattering spectrometer and was set to observe spectra around the three-halves harmonic wavelength of 234 nm. The 1200-grooves/mm grating, blazed at 250 nm, was chosen to give peak light transmission efficiency and good resolution while retaining a large enough spectral field of view (65 nm) to contain the up-scattering and three-halves features within it.

The down-scattering spectrometer, SOS-I, had a much larger spectral field of view to observe the spectra from less than 400 nm to more than 700 nm ( $\omega_0/2$ ).

The third major diagnostic was a filter-fluorescer electron x-ray continuum spectrometer (FFLEX).<sup>73</sup> This diagnostic consisted of ten K-edge-filtered diodes and PMT's and another ten filter-fluorescer channels. Located on the opposite side of the target normal from the interaction beam, FFLEX measured an approximation to the cold and superhot-electron temperatures. Although a filter-fluorescer detector has a much narrower energy bandwidth than a K-edge filter, interpretation of FFLEX data is subject to the same caveats that are attached to the GDL electron x-ray continuum measurements that have already been discussed in Chapter III.

Other diagnostics were also deployed. Although these measurements will not

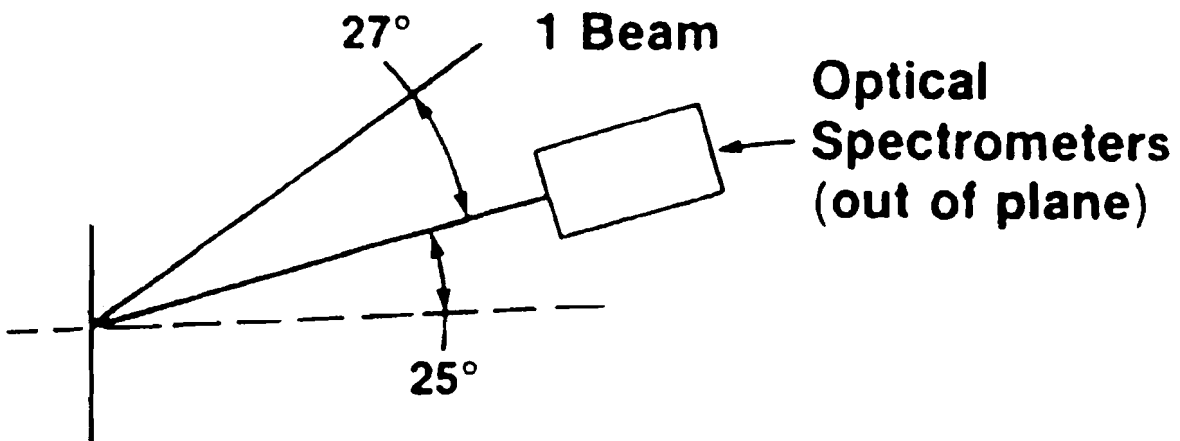


Figure IV-3. The scattered light was collected by two 1/4-m spectrometers and time-resolved by streak cameras. These were  $27^\circ$  from the interaction beam and  $18^\circ$  out of the plane defined by the interaction beam and the target normal.

be quoted in this dissertation, they served as a qualitative check on the understanding of the plasma expansion and subsequent development. For instance, the results of the 22X device, a Wolter x-ray microscope with a streak camera output, could be qualitatively modelled by LASNEX,<sup>74</sup> the standard Livermore hydrodynamics computer code.

A pair of instruments gave the time history of several discrete bands of optical and x-ray emission. OP-XRAY was a three-channel x-ray spectrometer with pass bands at 0.7, 1.5, and 2.5 keV. OX-OPT measured the time-resolved emission from four channels:  $\omega_0/2$ ,  $\omega_0$ ,  $3\omega_0/2$ , and the 400- to 600-nm band (with residual, unconverted, 0.53- $\mu\text{m}$  radiation blocked with a filter). The last channel was meant to measure the temporal behavior of the light scattered by SRS.

The SOP, or streaked optical pyrometer, was instead used as a  $3\omega_0/2$  time-resolved, one-dimensional imager by replacement of the usual wavelength defining filter stack with a  $3\omega_0/2$  bandpass filter. Since  $3\omega_0/2$  emission is a signature of the  $n_c/4$  surface,<sup>75</sup> this gave a time history of the expansion and burn-through of the quarter-critical surface which is where superhot electrons are generated by two plasmon decay.

Two other diagnostics were also important: SOS-IV and the EBM's. SOS-IV measured the Brillouin backscattered light from the interaction beam as well as from one other angle. The EBM's, or energy balance modules,<sup>76</sup> were photodiodes that separately measured the time-integrated energy reflected at the fundamental (351 nm) and in the SRS band. There were approximately forty pairs of diodes arrayed around the chamber, covering all angles except direct backscatter into the interaction beam. The total amount of Raman-scattered light was estimated by calculating the solid angle of each photodiode and then assigning the signal from each diode a weight that



corresponded to the solid angle between that diode and the nearest neighboring diodes.<sup>77</sup>

In order to find the amount of Raman light generated by the interaction beam only, two kinds of shots were attempted. The first was the usual interaction shot. The second was termed a "null" shot because the interaction beam was not propagated to the target. In all other respects, the shots were identical. By subtracting the Raman energy generated by a null shot from that generated by an interaction shot, the Raman light created by the interaction of the interaction beam with a long-scale-length plasma was measured. The fraction of Raman scattered light was found to be approximately 10% to 20% of the energy in the interaction beam,<sup>78</sup> not much higher than for short-scale-length interactions. This is an important piece of evidence for the feasibility of inertial confinement fusion.

The shots for which a useable and complete set of data has been compiled are listed in Table IV-1. Problems with diagnostics, and especially with beam timing, are the reasons for the low yield of useable shots.

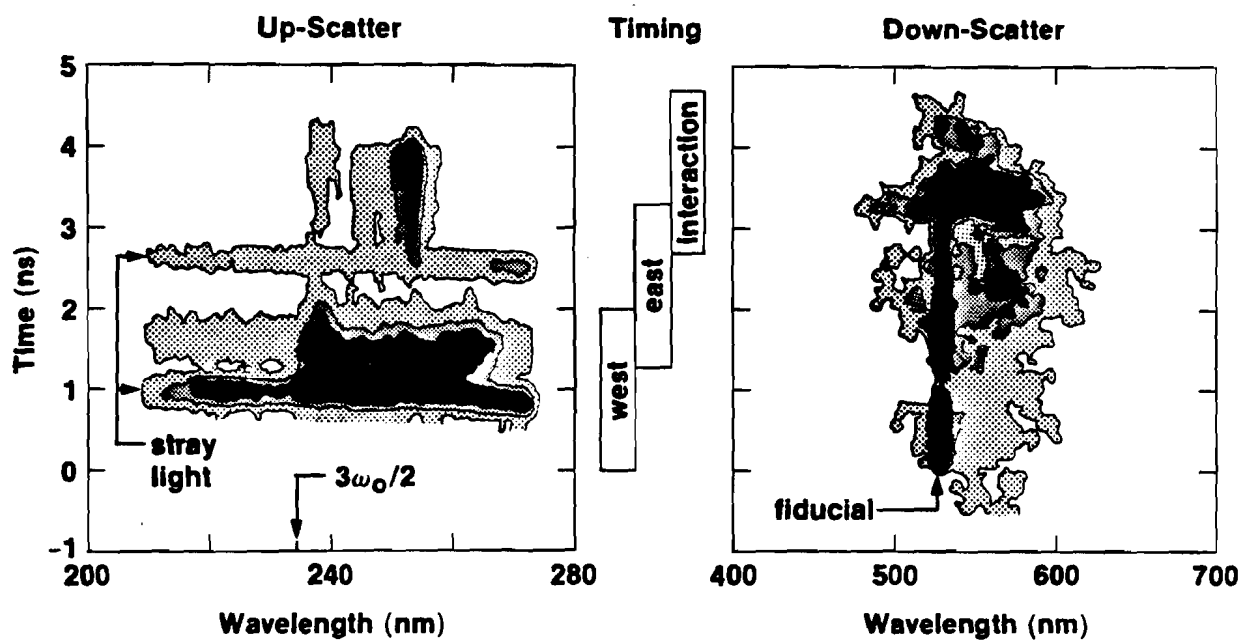
## **B. Results**

The primary result of this chapter is shown in Figure IV-4. In it, the temporal and spectral histories of the up-scattering and down-scattering from the same interaction shot are shown. The important result of this figure is that the temporal histories of the up- and down-scattering bands are well-correlated with each other and with the high-intensity interaction beam. Both streaked spectra are complex and deserve a detailed discussion, beginning with the up-scattered spectra.

First, the stray light bands must be ignored. This light was eliminated in later

**Table IV-1: Long-Scale-Length Shots at LLNL**

Shot Number	18012007	18012904	18020407
Type of Shot	Null	Interaction	Null
Number of Beams	9	10	8
<b>Relative Timing (ns)</b>			
West	0.0	0.0	0.0
East	1.3	1.3	1.3
Interaction		2.8	
<b>351-nm Energy (kJ)</b>			
West	7.1	9.9	9.3
East	5.9	7.3	7.3
Interaction	0.0	2.1	0.0
Total	13.0	19.4	16.6
<b>Intensity (<math>\times 10^{14}</math> W/cm<sup>2</sup>)</b>			
West	7.7	10.7	10.0
East	6.4	7.8	7.9
Interaction	0.0	15.6	0.0
<b>Electron Temperatures (keV)</b>			
Cold Temperature	2.5	2.8	2.7
Superhot Temperature	25	26	21



E4607

Figure IV-4. Time-resolved spectra from the interaction shot. The relative timing of the clusters is shown in the center. The stray-light bands in the up-scatter spectrum should be disregarded. The up-scatter intensity contours are at 1, 5, and 10% of the maximum intensity while the down-scattering contours are at 5, 10, and 15% of maximum.

shots. Then, the correlation between the timing of the laser and the appearance of intense scattering bands should be noted. Initially, no scattering is seen when the west beams are fired because the target has not yet burned-through. (SAGE calculations show that the target burns through at approximately 2 ns.<sup>79</sup>) When the east cluster turns on, broad-band scattering is immediately seen because the diagnostics are on the same side of the target as the east cluster. This is enhanced Thomson scattering. This scattering lasts for less than 1 ns because the plasma is rapidly evolving. The plasma becomes underdense at approximately the same time that this burst of scattering ends. Another pulse of ETS light is seen when the interaction beam, also on the same side of the target as the diagnostics, turns on. The scattered light does not last throughout the duration of the interaction beam because by that time, the plasma has essentially disappeared.

The presence of  $3\omega_0/2$  scattering in these streak photographs indirectly shows the presence of superhot electrons. Scattering at  $3\omega_0/2$  is primarily caused by the nonlinear coupling between an incident laser photon (at  $\omega_0$ ) and a plasmon of frequency  $\omega_0/2$ . Higher order processes, such as a three-plasmon interaction, or a  $2\omega_0$  photon coupling with a plasmon, are also possible, but are considerably weaker.<sup>75</sup> No matter which of the processes is invoked, mixing with  $\omega_0/2$  plasmons is required. The source of these plasmons can only be the two plasmon decay instability. The TPD instability is expected to be present because its threshold is low, much less than the threshold for SRS-A or SRS-C,<sup>57</sup>

$$I_{\text{TPD}} = \frac{2 \times 10^{16} T_e(\text{keV})}{\lambda_\mu L_\mu} \quad (\text{IV-1})$$

The threshold intensity is  $I_{\text{TPD}} \approx 10^{14} \text{ W/cm}^2$  for the conditions of this plasma with  $T_e \approx 2.6 \text{ keV}$ , which is much less than the intensity of any of the laser beams. If the

electron temperature were lower, the threshold would also fall (e.g. if  $T_e = 1$  keV then  $I_{\text{TPD}} = 4 \times 10^{13}$  W/cm<sup>2</sup>). Thus, the TPD instability is easily excited in a long-scale-length plasma produced by a 351-nm laser. The presence of  $3\omega_0/2$  scattering is a confirmation of this and also that a quarter-critical density surface exists since TPD can only occur in the vicinity of  $n_c/4$ .

Superhot electrons are produced by either SRS-A at the peak of a parabolic density profile,<sup>49</sup> (the profile here) or by SRS-A or TPD at the quarter-critical surface. Three-halves emission shows that TPD is excited and is therefore producing superhot electrons. The presence of the three-halves scattering is evident in Figure IV-4. It begins as soon as the east beams turn on and does not end until almost the end of the interaction pulse (Figure IV-5). The growth, saturation, and decay of the up-scattering signal follows the changes in the level of  $3\omega_0/2$  scattering very closely. In particular, there is no up-scattering after the  $3\omega_0/2$  signal ends; that is, the scattering ends when the superhot-electron production ends.

The location of the quarter-critical surface is also important. SAGE simulations, Figure IV-6, show that the foil burns through, on-axis, approximately 2 ns into the shot and that the peak plasma density, on-axis, falls below quarter-critical very quickly after that (in a few hundred picoseconds). The same qualitative features are reproduced with the hydrodynamic similarity solution of London and Rosen.<sup>70</sup> The quarter-critical surface must then be off-axis, and be a part of the cold finger of non-ablated material shown at the top of Figure IV-7. The actual Nova beams are focused with  $f/4$  lenses while the SAGE simulations were performed with an  $f/1$  beam representing each cluster of five beams. It is not expected that these simulations will exactly model the interaction, but they do serve as a general guide. LASNEX simulations also show the colder, denser material near the beam. Although the part of

## Up-Scattering and $3\omega_0/2$ Temporal Histories

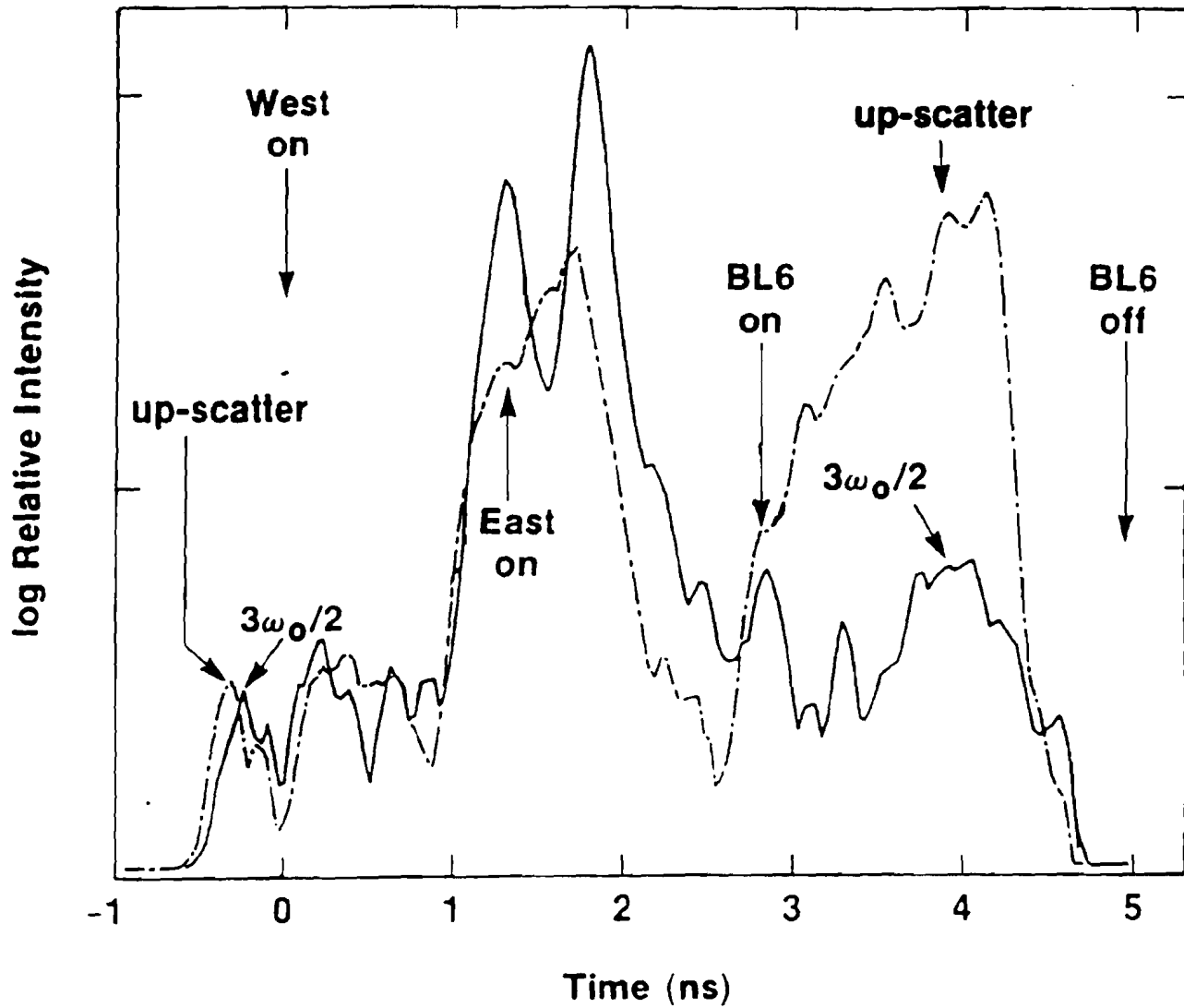


Figure IV-5. Temporal lineouts show the good correlation between the up-scattering band and  $3\omega_0/2$  radiation.

## Maximum Electron Density

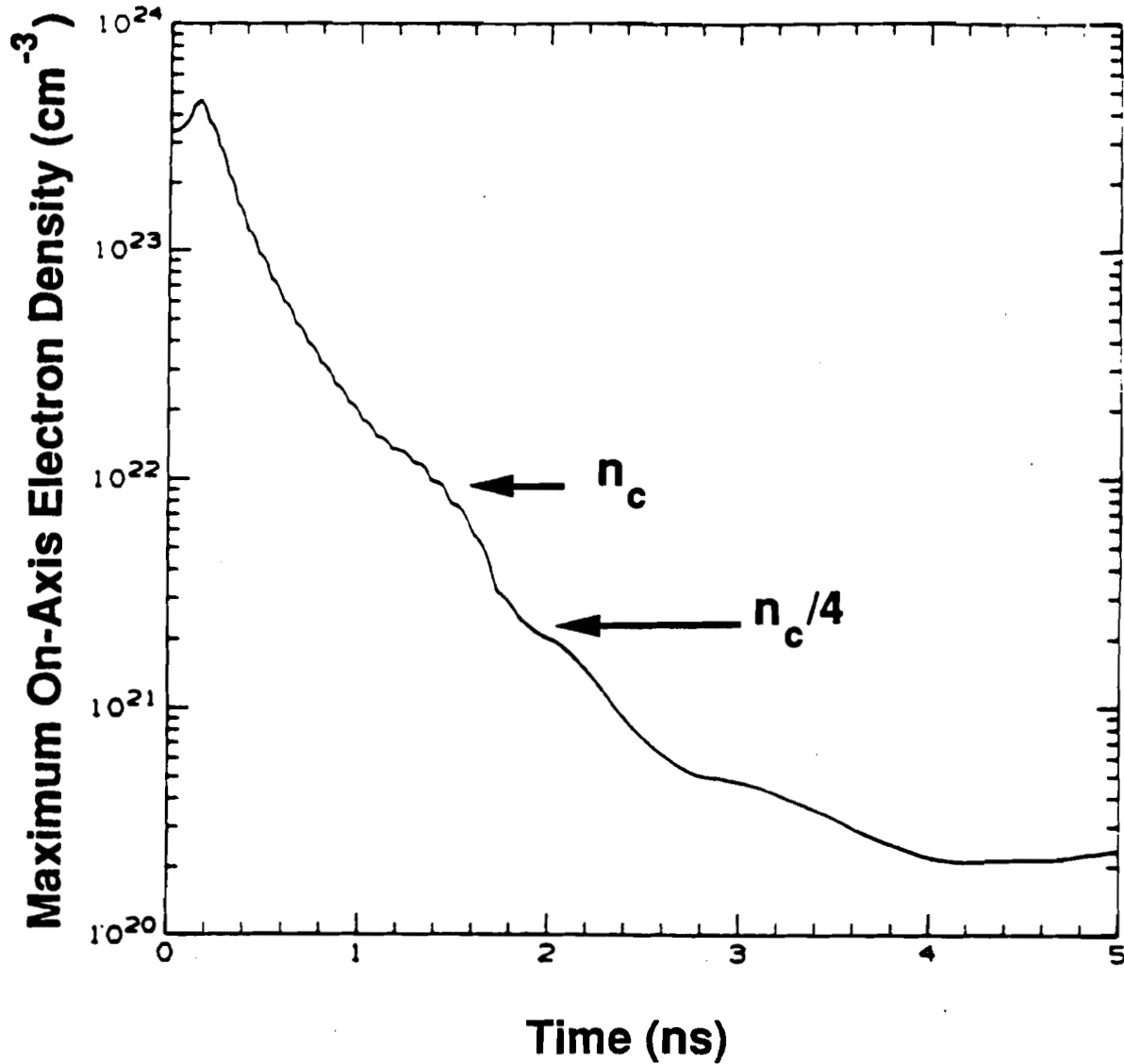


Figure IV-6. SAGE calculations show that, on-axis, the target burns-through in less than 2 ns and that, on-axis, the quarter-critical surface disappears a few hundred picoseconds after that.

## Isodensity Contours at 2.7 ns

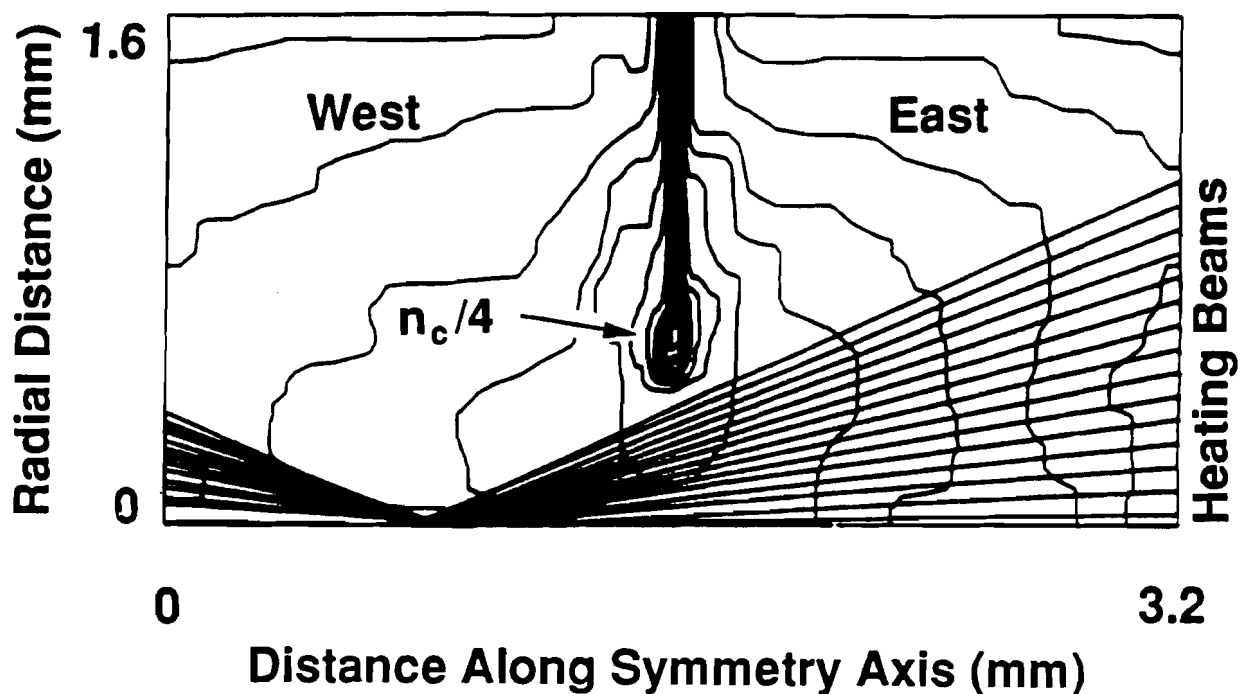


Figure IV-7. Although the target burns through quite early, at the time of the interaction pulse, higher density areas remain off-axis. The isodensity contours represent changes of a factor of 2 of the density. The lowest contour represents a density of  $0.002n_c$ .



the Nova beam containing most of the beam energy misses these denser regions, the beam has very large wings<sup>80</sup> that may have enough energy to produce the  $3\omega_0/2$  light and the superhot electrons.

The time-resolved down-scattering is also shown in Figure IV-4. Correlation with the up-scattering spectrum is readily seen. The fiducial is 527-nm light that has not been converted in the tripling crystals, reflected by the target support stalk. The fiducial from the west beams is seen first, before any signal is seen in the up-scattering spectrometer. This is because the up-scattering signal, which originates on the far side of the target, is masked from the spectrometer until the target burns-through. On the other hand, the fiducial light is reflected from the target support frame, from either above or to the side of the target, and is not blocked by the target. The turn-on of the east and interaction beams is easily seen.

The correlation between the up-scattered band at 254 nm and the down-scattered band at 569 nm is shown in Figure IV-8. The relative timing between the two spectra is estimated to be within 100 ps. Scattering of stray green light from the target support structure gave the absolute calibration of the down-scattering to the sequence of laser pulses. The absolute timing of the up-scattered spectra was estimated from the onset of the stray light from the interaction beam and checked against the observation of ETS with the commencement of the east beam irradiation.

There seem to be two peaks in the down-scattering spectrum that are correlated with the up-scattering due to the interaction pulse. Although there is a relative minimum in the up-scattering corresponding to the minimum between the two down-scattering peaks, there are no laser or plasma parameters that are changing at that time. There does not seem to be any down-scattering above the noise level when the east-cluster irradiation begins.

## Up- and Down-Scattering Correlation

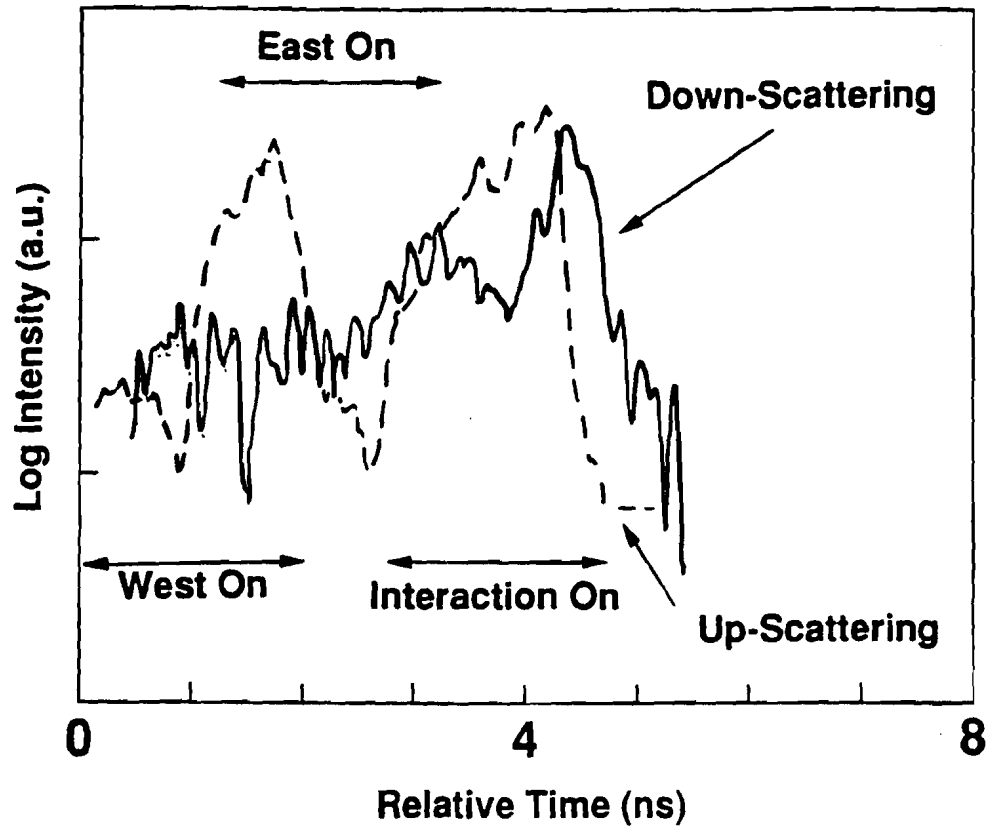
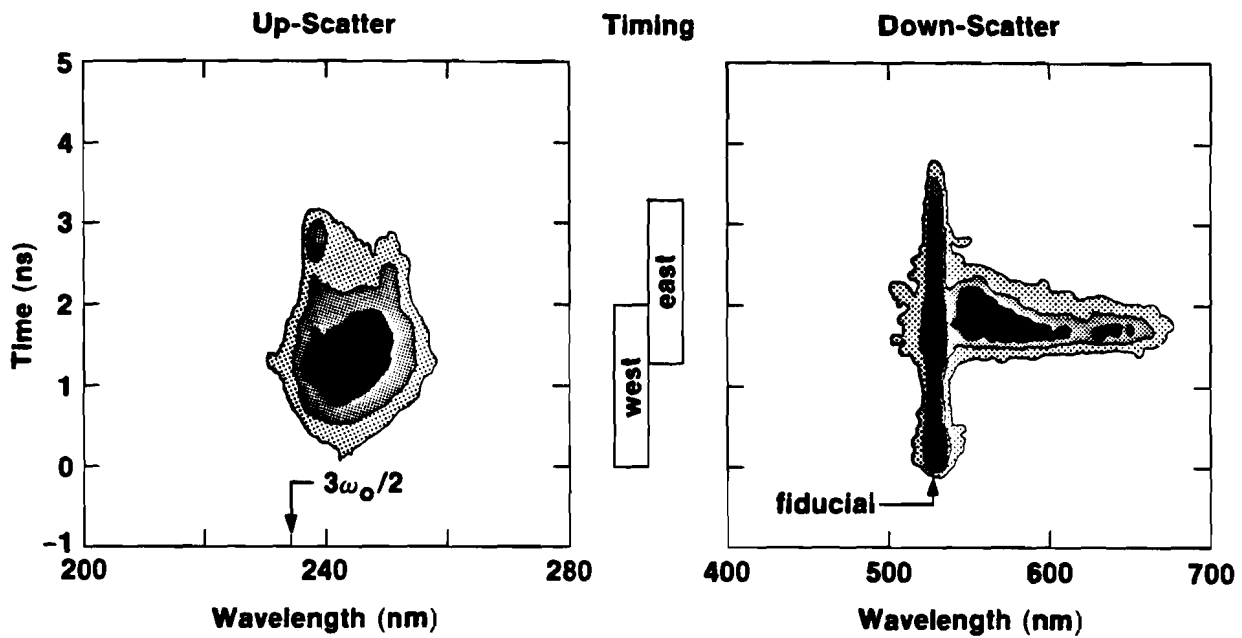


Figure IV-8. The down-scattering at 569 nm and the up-scattering at 254 nm are well-correlated in time, and both immediately grow when the interaction beam turns on.



E4606

Figure IV-9. Time-resolved spectra from a null shot where the interaction beam was not used. Intensity contour levels are at 1, 5, and 10% of the maximum intensity.

The interaction shot can be contrasted with a null shot, Figure IV-9, where the interaction pulse was not fired. The second null shot was similar to the one presented in Figure IV-9. These spectra, being taken later in the experimental campaign, have much less stray light and are easier to interpret. The down-scattering shows only a single burst when the east beams are fired. The down-scattering temporal history of the interaction and null shots are the same until the interaction beam is fired. The up-scattering also appears similar. The three-halves feature is still in existence from near the beginning of the pulse throughout the duration of the heating beam's pulse. The ETS signal at longer wavelengths than the three-halves, however, lasts slightly longer than on the interaction shot. The temporal history of the up-scattering in the null shot is shown to be similar to the interaction shot in Figure IV-10. The up-scattering in the two shots begins at the same time, reach comparable intensity levels, and the rise and fall times are similar. There is no more up-scattering after the last heating beam turns off. These two shots show that while the interaction beam creates distinct ETS up- and down-scattered bands, the initial heating beams also create ETS scattering bands.

The electron temperatures inferred by FFLEX are included in Table IV-1. All shots were reasonably fit with two temperatures; an example is shown as Figure IV-11. The cold-electron temperatures, due to collisional absorption of the laser light, varied between 2.5 and 2.8 keV. The superhot temperature, from processes at the quarter-critical surface, varied between 21 and 30 keV. Generally, the interaction shots seem to have had higher superhot temperatures, but all of the measurements are subject to uncertainties. The cold temperatures could vary more because only two detector channels (5-7 and 7-9 keV) determined the cold temperature.

Although the best fits were with two temperatures, several shots were initially

## Up-Scattering and Null Temporal Histories

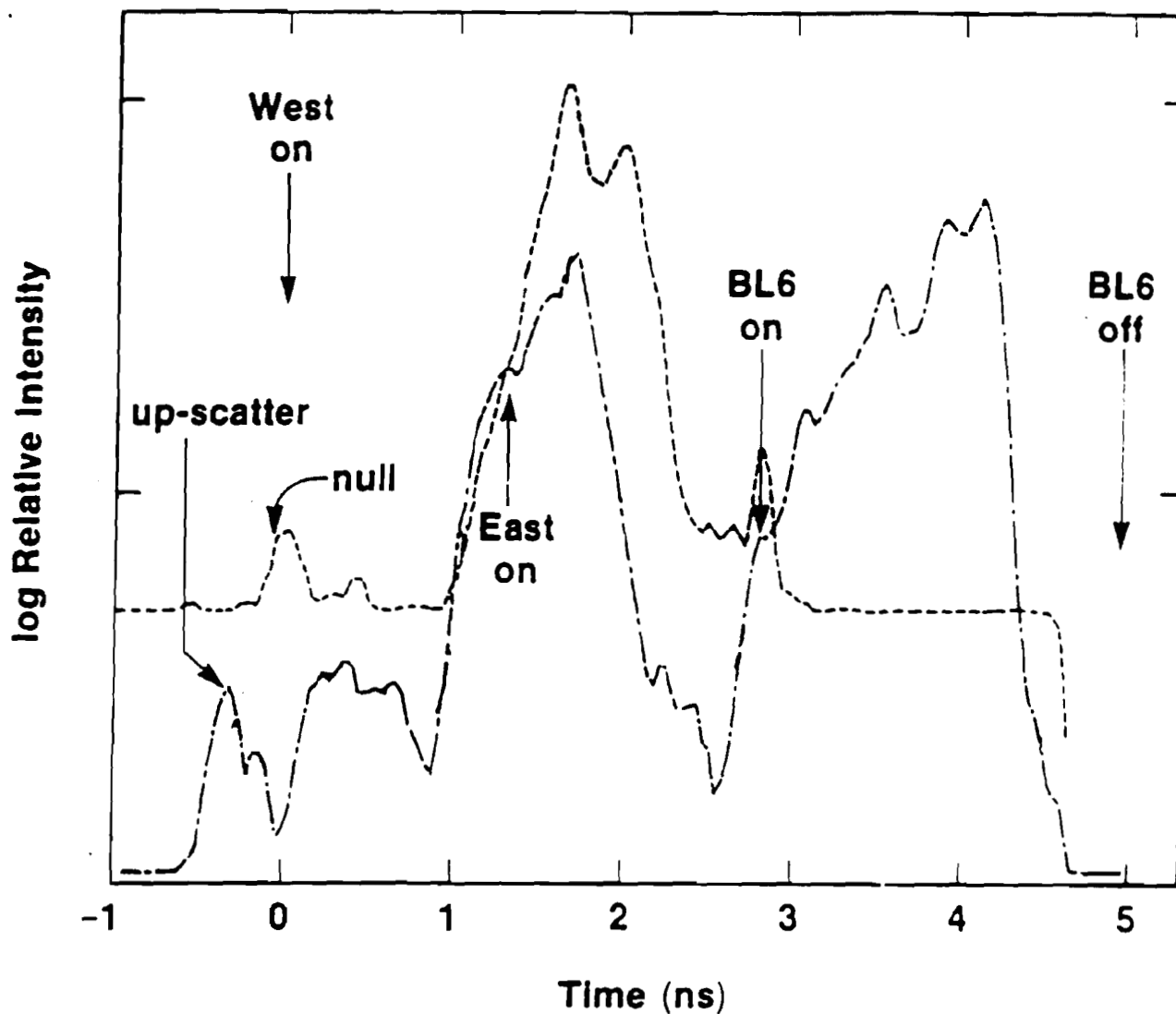


Figure IV-10. Temporal lineouts of up-scattering at the same wavelength, 254 nm, from the null and interaction shots show the reproducibility of the heating phase of the shot and highlight the scattering caused by the interaction beam.

## FFLEX Spectrum: Shot 18012904

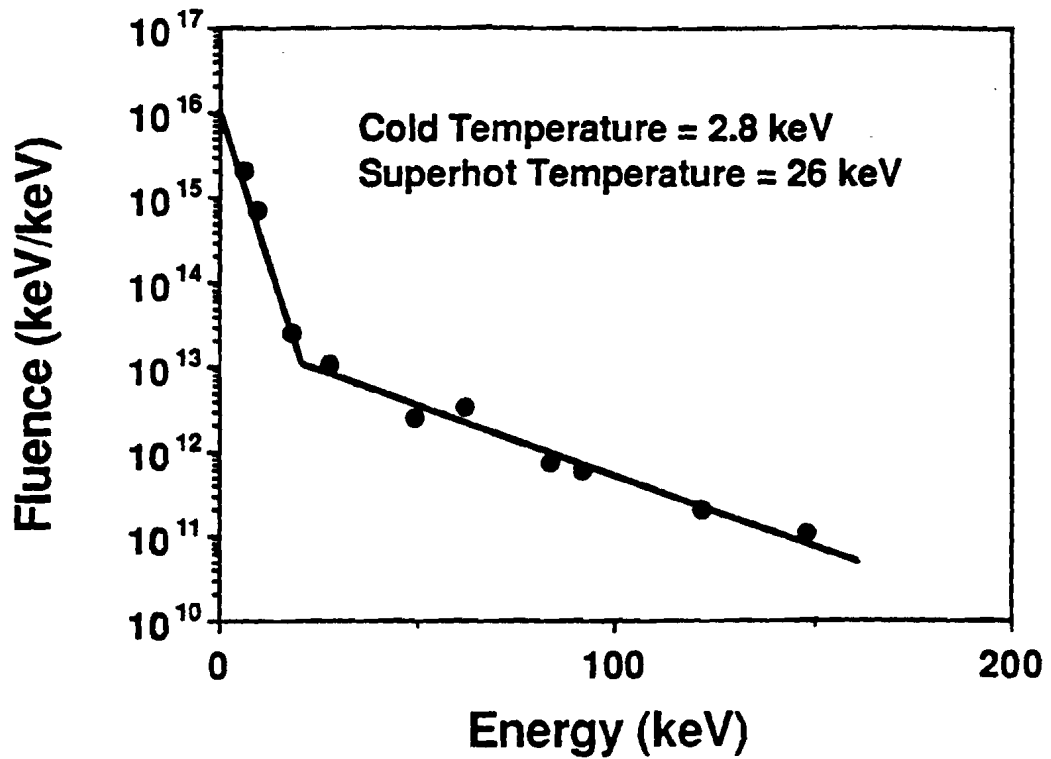


Figure IV-11. The time-integrated electron temperatures for the interaction shot were deduced by fitting a bi-Maxwellian distribution to the x-ray continuum energy measurements.

fit with three temperatures — a hot-electron temperature was included. When these were recalculated for two temperatures, no apparent degradation in the fit was seen. A two temperature fit is more plausible since it is expected that the level of resonance absorption, the source of the hot electrons, is greatly reduced in 351-nm-laser irradiation as opposed to 527-nm-laser irradiation.<sup>43</sup>

### C. Discussion

As was shown in the previous section, the differences between the interaction and null shots were as expected. Both the measured superhot- and cold-electron temperatures were slightly higher for the interaction shot. Both the up- and down-scattered spectra were also similar until the time when the interaction beam fired. For the null shot, Figure IV-9, the interaction ended, but for the interaction shot, Figure IV-4, both three-halves harmonic and enhanced Thomson scattering were evident until near the end of the interaction pulse. Both of the down-scattering spectra showed a burst of light when the east cluster fired, correlated in time with the appearance of an up-scattered ETS band. The null shot shows just this one down-scattered feature, but the interaction shot shows another down-scattered band when the interaction beam is fired.

The location of these scattering bands will now be compared to the theory developed in Chapter II. A spectrum of the interaction shot at 3.6 ns is presented in Figure IV-12. Note that the wavelength scales are different and that the relative intensity scales each have different arbitrary units. The up-scattering spectrum shows a large, narrow peak at approximately 254 nm. The peak is much more intense than the  $3\omega_0/2$  signal. The down-scattering is a very broad, intense scattering band between

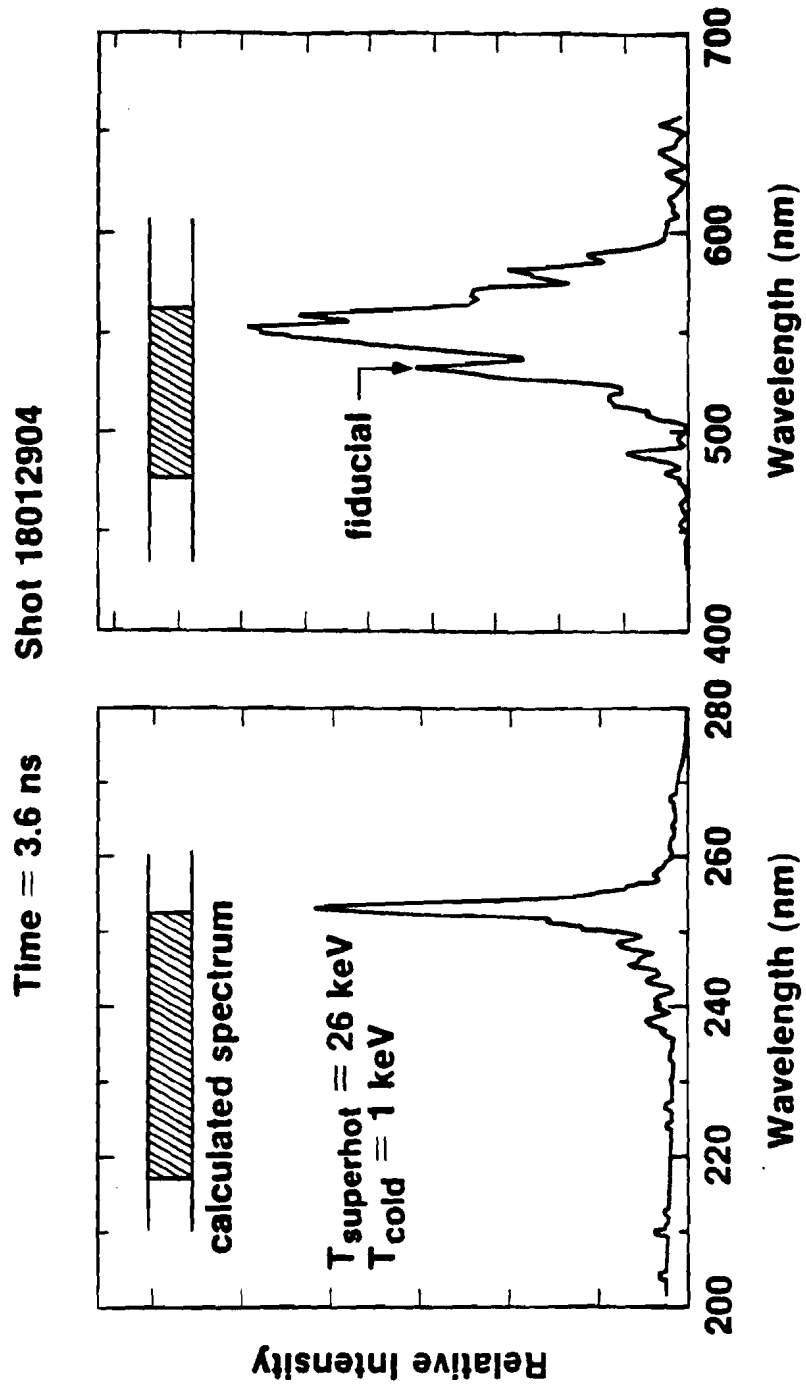


Figure IV-12. A spectral lineout taken during the interaction-beam pulse shows a narrow up-scattered band and a rather wide down-scatter band.



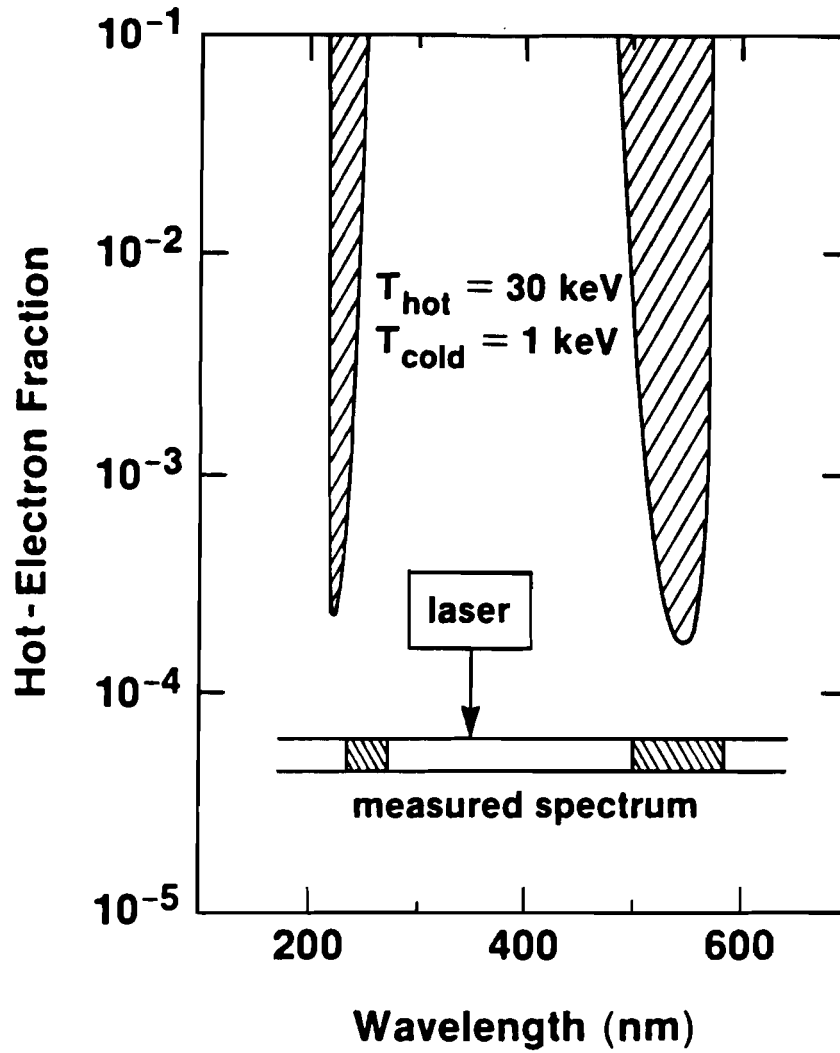


Figure IV-13. The ETS predictions for the interaction shot show that a hot-electron fraction of  $\approx 10^{-3}$  is a good fit to the spectrum of Figure IV-12.

approximately 500 and 600 nm. It is consistent with the ETS theory that the up-scattering band is much narrower than the down-scattering band.

The predicted enhanced scattering bands are shown in Figure IV-13. With a hot-electron fraction of  $f_h = 10^{-3}$ , the fit is in reasonably good agreement with the measured spectrum. Theory predicts an up-scattering band at a slightly shorter wavelength than was observed. This could be due to a more complicated refraction than was modelled in the calculation. The cold-electron temperature that gave the best fit to the data, 1 keV, was not the same as the measured value of 2.8 keV. The cold temperature is much lower because FFLEX is a time-integrated (over the entire interaction) as well as a spatially-averaged measurement and varies depending on irradiation energy and electron density, as well as many other factors. The cold-electron temperature varies throughout the plasma corona at any given time. The suprathermal electrons, however, are expected to have approximately the same temperature throughout the corona. The real temperatures of interest are the time-averaged temperatures averaged over only a relatively short interval immediately before the time of interest. SAGE calculations, Figure IV-14, show that at 3.6 ns into the interaction, the electron temperatures are much lower than the FFLEX measurement. Off-axis, where the quarter-critical-density surface is, the temperature is about 1 keV. In the rest of the interaction region, the temperature is between 0.5 and 1.5 keV, a small enough range to have little effect on the ETS fit.

In ETS, the incident laser light scatters from plasma waves enhanced by the presence of bursts of suprathermal electrons. The plasma waves that are enhanced have a phase velocity equal to the velocity of the electron burst. Therefore, the scattered light should be symmetric in electron-plasma-wave phase-velocity space. In particular, the scattered light should be symmetric in the phase velocity that is calculated by only

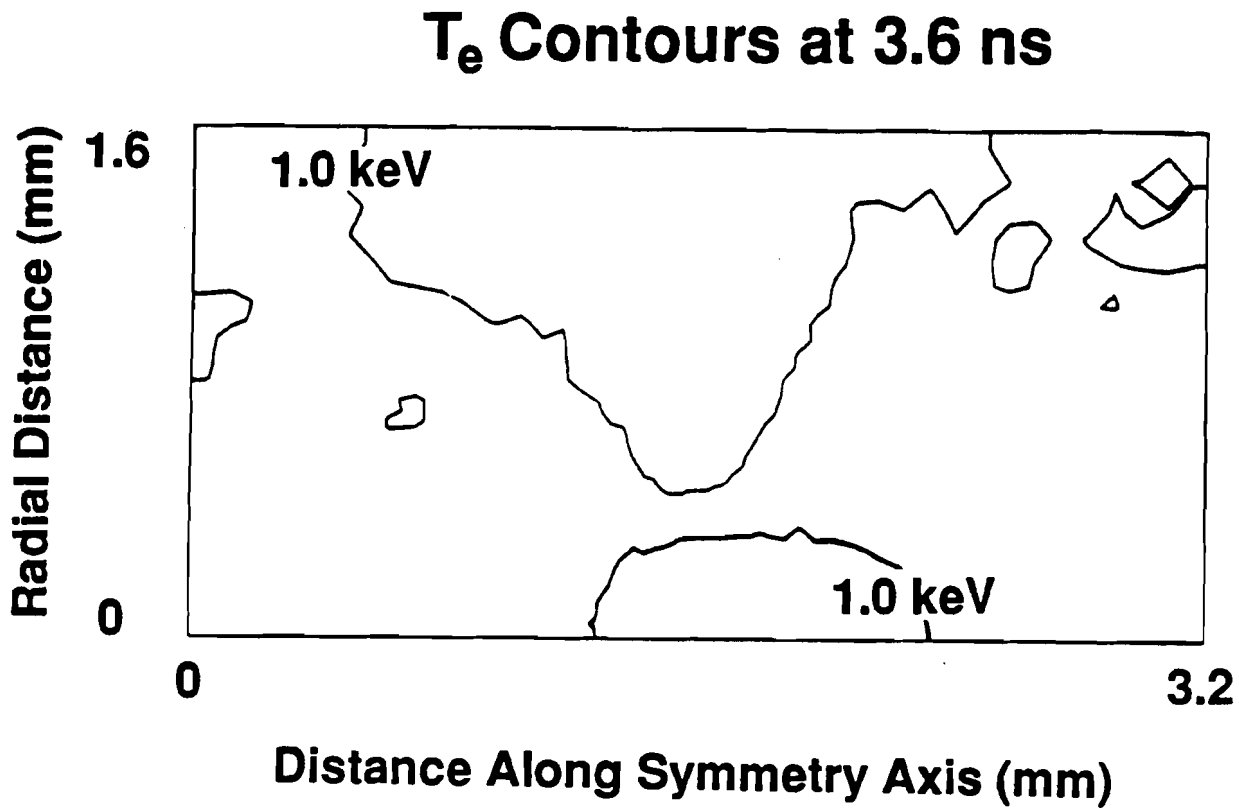


Figure IV-14. SAGE calculations show that the bulk electron temperature of the plasma is approximately 1 keV during the interaction pulse. The target was initially at the center of the horizontal axis and was assumed to be of infinite extent vertically. The interaction beam is incident from the right-hand side of the simulation frame.

considering the component of  $k_{epw}$  that is along the density gradient;

$$v_{\phi} = \frac{\omega_{epw}}{(k_{epw})_x} \quad (IV-2)$$

Even though the frequency-matching conditions,

$$\omega_s = \omega_0 \pm \omega_{epw} \quad (IV-3)$$

are symmetric in frequency shift (the + sign refers to up-scattering), the only scattering that will be enhanced is that which has the correct phase velocity. The frequency shift of the scattered light will not be symmetric if the up- and down-scattering spectra are measured at the same angle with respect to the laser direction. The following argument shows this. The measured frequency of the up-scattered light is, by definition, greater than the down-scattered light. This means that the up-scattered wave vector, and consequently the electron-plasma wave vector, will also be larger. The up- and down-scattering spectra are thus sampling different plasma waves. However, because it is assumed that the electrons have been emitted in monoenergetic, unidirectional bursts, the phase velocities of the electron-plasma waves must still be the same. This also means that the electron-plasma-wave frequencies will differ, so that, from Eq. (IV-3), the scattered light will not be symmetric in scattered light frequency. For the same reason, the scattering will not be symmetric in electron-plasma wave vector space.

Direct comparison to the ETS theory can be made in phase-velocity space. Figure IV-15 plots the scattered-light intensity as a function of phase velocity for the data presented in Figure IV-12. Overlaid are the ETS-predicted bands calculated for a hot temperature of 26 keV. It is readily apparent that the majority of the down-scattered light is fit by the ETS theory. There is some additional scattering from high-phase-velocity plasma waves (long-wavelength scattered light). This extra scattered light may be at the noise level of the streak camera, or it may be the result of

# Phase-Velocity Symmetry of Up- and Down-Scattering

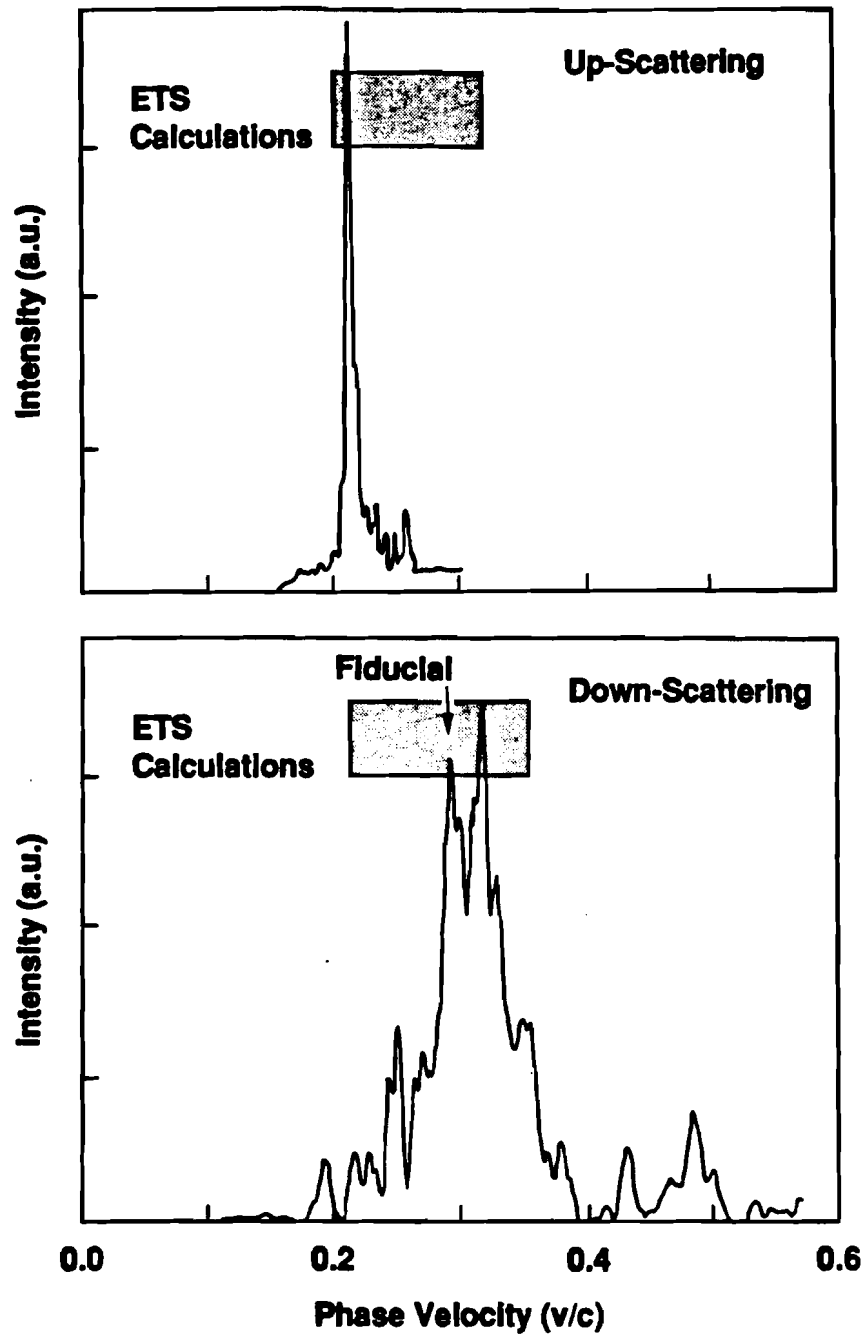


Figure IV-15. Direct comparison to ETS theory may be made in phase-velocity space. The spectra are plotted in terms of the absolute value of the electron-plasma-wave phase velocity in the direction of the density gradient. The theory is in good agreement with the measurements.

some other plasma process.

The up-scattered light is also reproduced by the theory. The low-phase-velocity (long-wavelength) cutoff is accurately reproduced, but the high-phase-velocity cutoff is not. A consistent feature of almost all of the spectra examined is that when the down-scattering peak is correctly fit in terms of the electron temperatures and the hot-electron fraction, the up-scattering band does not extend to wavelengths as short as predicted. This is a counter-intuitive result because up-scattered light (in this geometry) originates from electron-plasma waves that are propagating out of the plasma. Suprathermal electrons are assumed to be emitted in this same direction and then reflected by sheaths at low electron densities. Because the electrons must lose some energy as they traverse the plasma, it is reasonable to assume that the electrons flowing towards lower density would have a higher energy (velocity) than those that have been reflected once. This means that the phase velocities of the plasma waves contributing to up-scattering should be higher than those directed into the plasma that contribute to down-scattering. From this argument, the scattered light is expected to be asymmetrical with the phase velocity shift corresponding to the energy loss of the electrons. The spectra shown in Figure IV-15 show that just the reverse shift was measured. There must be some cutoff mechanism that will self-consistently reproduce the observed spectra.

Because the bulk of this plasma is below  $n_c/4$ , it may be possible that no scattering is seen from higher phase velocities because there is too little plasma at the appropriate density. This conjecture requires an examination of the density at the origin of the scattering. Figure IV-16 once again reproduces the spectra of Figure IV-12, but this time in terms of the density required to satisfy the frequency- and wave-matching conditions. The down-scattered light comes from electron densities between 0.03 and

## Density at Origin of Scattering

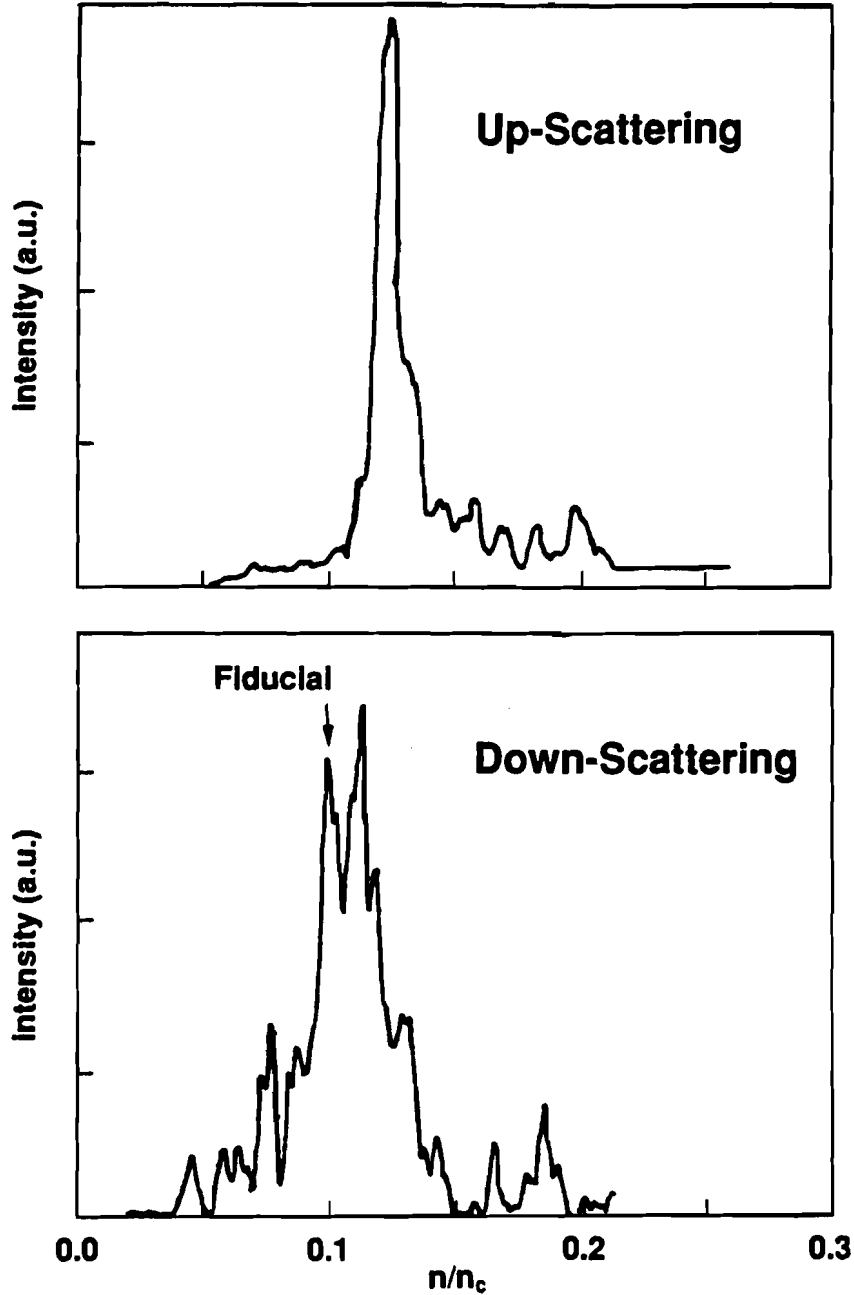


Figure IV-16. Both up- and down-scattering originated at densities below quarter-critical. The bands did not, however, originate at the same density.

0.2  $n_c$ . The lower frequency of the down-scattered light requires a smaller  $k_{epw}$ , which in turn, requires a smaller plasma frequency. The up-scattered light occurs at much higher densities, between 0.1 and 0.22  $n_c$ . Again, this is required to satisfy the matching conditions. It should be noted here that both up- and down-scattering can occur at many other densities than those presented in Figure IV-16. It is the placement of the optical diagnostics that restricts the scattering to the density ranges observed. Also, while the two spectra were not collected by the same diagnostic, the two spectrometers were symmetrically placed with respect to the interaction beam and the target normal.

A sharp plasma-density cutoff at 0.2  $n_c$  would explain the up-scattered spectrum because higher phase velocities come from denser plasma for both up- and down-scattering. For the observed spectra to match ETS predictions, it would be necessary to observe up-scattering from densities greater than 0.3  $n_c$ , while no scattering was observed from densities greater than about 0.2  $n_c$ . A sharp plasma-density cutoff would not be a factor in the down-scattered spectrum. It has already been inferred from the existence of  $3\omega_0/2$  emission that a quarter-critical density surface exists in the plasma. However, by comparing a Nova beam intensity profile<sup>80</sup> to the density distribution predicted by a SAGE simulation, Figure IV-7, it is apparent that the threshold for the two plasmon decay instability, which is the mechanism that occurs only at  $n_c/4$  and produces  $3\omega_0/2$  emission, is only marginally satisfied. This is especially true after the east and west clusters turn off, as is shown in Figure IV-5 by the drop in  $3\omega_0/2$  emission. The majority of the laser energy encounters plasma that is much less dense than  $n_c/4$ . The most intense scattering (see Figure IV-16) occurs at densities near  $n_c/10$ . This is consistent with the experimental design goal of producing a large plasma whose peak on-axis density, during the interaction pulse, was  $n_c/10$ .



Higher densities are assumed to be produced only near the remains of the "cold finger" of target material that extends into the low density region. Because the ETS theory, in its present form, does not make any predictions of the spectral shape or level of scattering, it is possible that the laser intensity at the  $n_c/4$  surface may be high enough to excite the TPD instability, but still be low enough that enhanced Thomson scattering will not be observable.

As discussed in Chapter II, stimulated Raman scattering has been suggested as an alternative theory to explain the complicated spectra that were observed. The up-scattered light would be the anti-Stokes line of SRS. Because both the Stokes and anti-Stokes lines are produced by the pump wave mixing with the same electron-plasma wave, the two modes will be scattered in different directions as a consequence of momentum conservation. An ideal test for this mechanism would observe the scattered light at two different angles so that the same electron-plasma wave satisfies both matching conditions. If SRS were the cause of both scattering bands, the scattered light would be symmetric in frequency shift from the laser frequency. Unfortunately, it was not possible to perform this test. Figure IV-17 shows that the up-scattered light was the result of scattering from plasma waves that had a significantly larger wave number than did those plasma waves leading to the observed down-scatter signal. The electron-plasma-wave frequencies deduced from the spectra of Figure IV-12, as suggested in Reference 50, are reproduced in Figure IV-18. Although the frequency up-scattered peak lies within the frequency range of the down-scattering band, the shape and size of the two bands are different. The up-scattered band, as predicted by ETS theory, is much narrower than the down-scattered band. Figure IV-16 shows that the electron densities observed are different for the two bands, or equivalently, the plasma frequencies at the origin of the scattering are different. The frequency of the

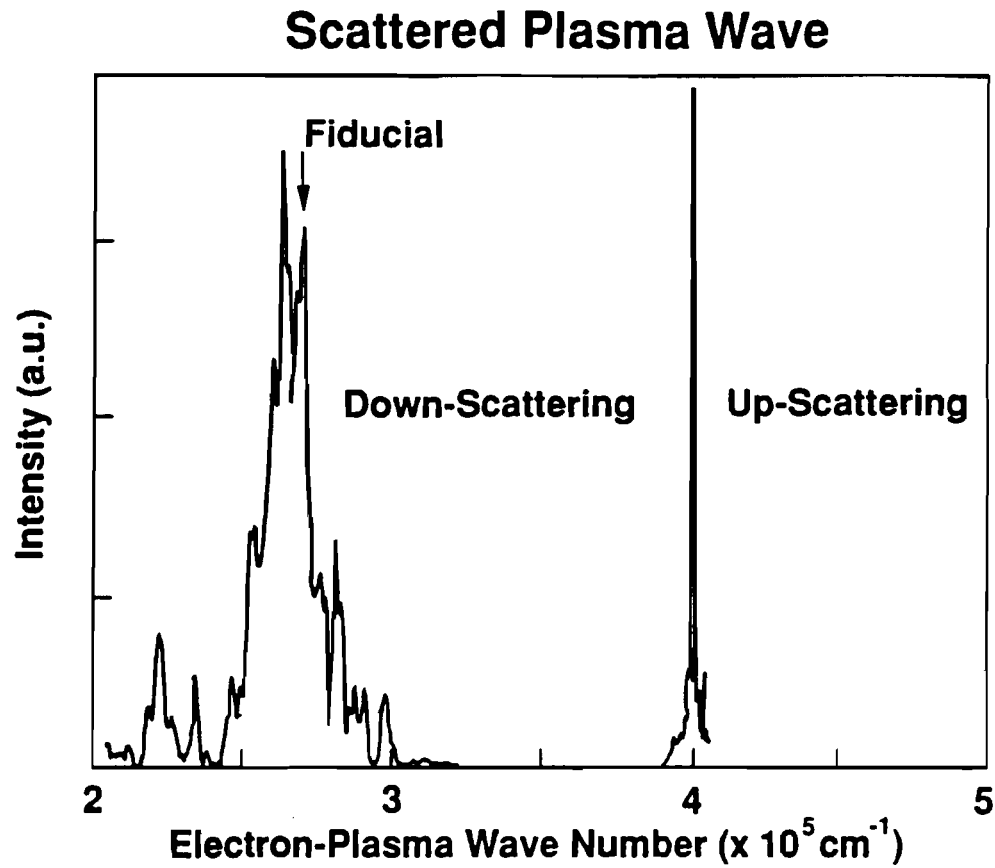


Figure IV-17. The up-scattering and down-scattering bands are scattered by different plasma waves.

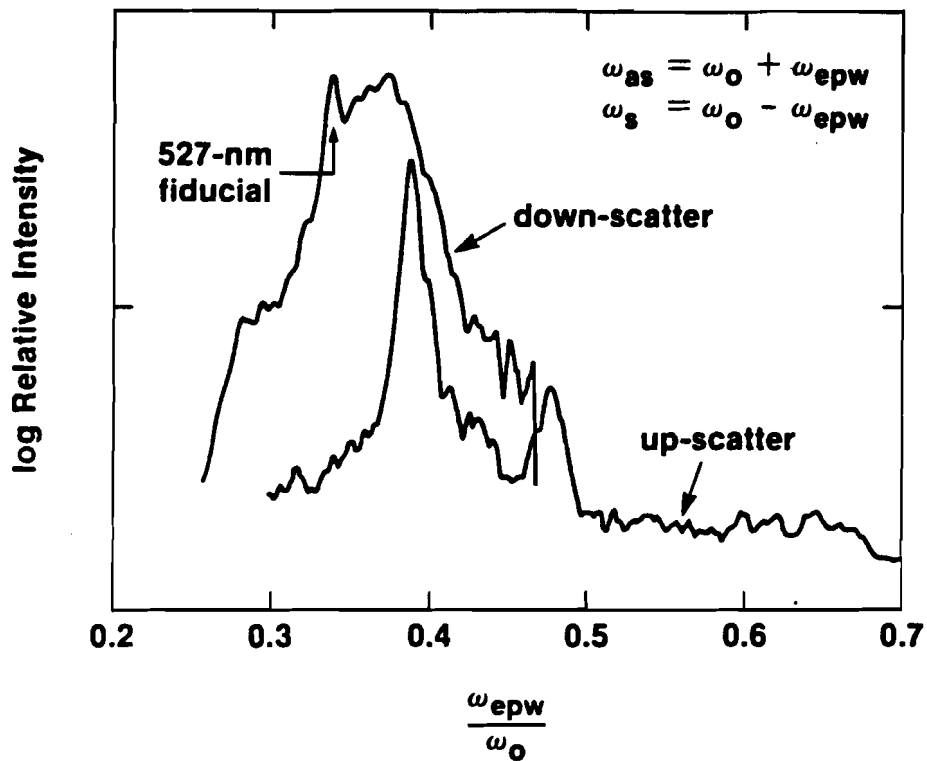


Figure IV-18. The electron-plasma-wave frequencies implied by the relation  $\omega_s = \omega_0 \pm \omega_{epw}$  show that these spectra are difficult to explain in terms of Stokes mixing. The spectra is the same as is in Figure IV-12.

electron-plasma wave is approximately equal to the plasma frequency at the origin of the scattering because the thermal correction term,  $3v_T^2 k_{epw}^2$ , is small. Nothing can be determined from these plots about Stokes/anti-Stokes generation in the plasma. It is unlikely that this type of emission was seen, however, because the production of frequency up-scattered light is usually limited to the forward direction where the small value of the electron-plasma wave vector makes the anti-Stokes mode resonant. The backwards anti-Stokes mode is not produced because the large electron-plasma wave vector is non-resonant for this direction.

The enhanced Thomson scattering during the interaction beam pulse varies in intensity (Figures IV-5, IV-8, IV-10) and in spectral width as shown in Figure IV-19. The band begins as a narrow, low-intensity signal, increases in width and in intensity as more hot electrons are generated and enhance the plasma waves, and ends as a very intense band that is somewhat narrower. The evolution of the width of the band, although very small, may give an indication of the temporal evolution of the background electron temperature. Figure IV-19 shows that the spectral width of the band may be roughly correlated with a changing cold temperature. The width of the down-scattered band also increased and then decreased, although the magnitudes of the spectral widths were not reproduced as well by the ETS predictions.

The width of the band varies because at low cold-electron temperatures, the reverse-slope resonance region is very small. As the background temperature is increased, the enhancement region gets larger until the bump-on-tail portion of the electron distribution function begins to overlap the background distribution. At still higher temperatures, the resonance region completely disappears. Many assumptions are built into the curve presented in Figure IV-19. For example, it was assumed that the hot-electron fraction and the hot-electron temperature remained constant throughout

## Variation in Width of Up-Scattering

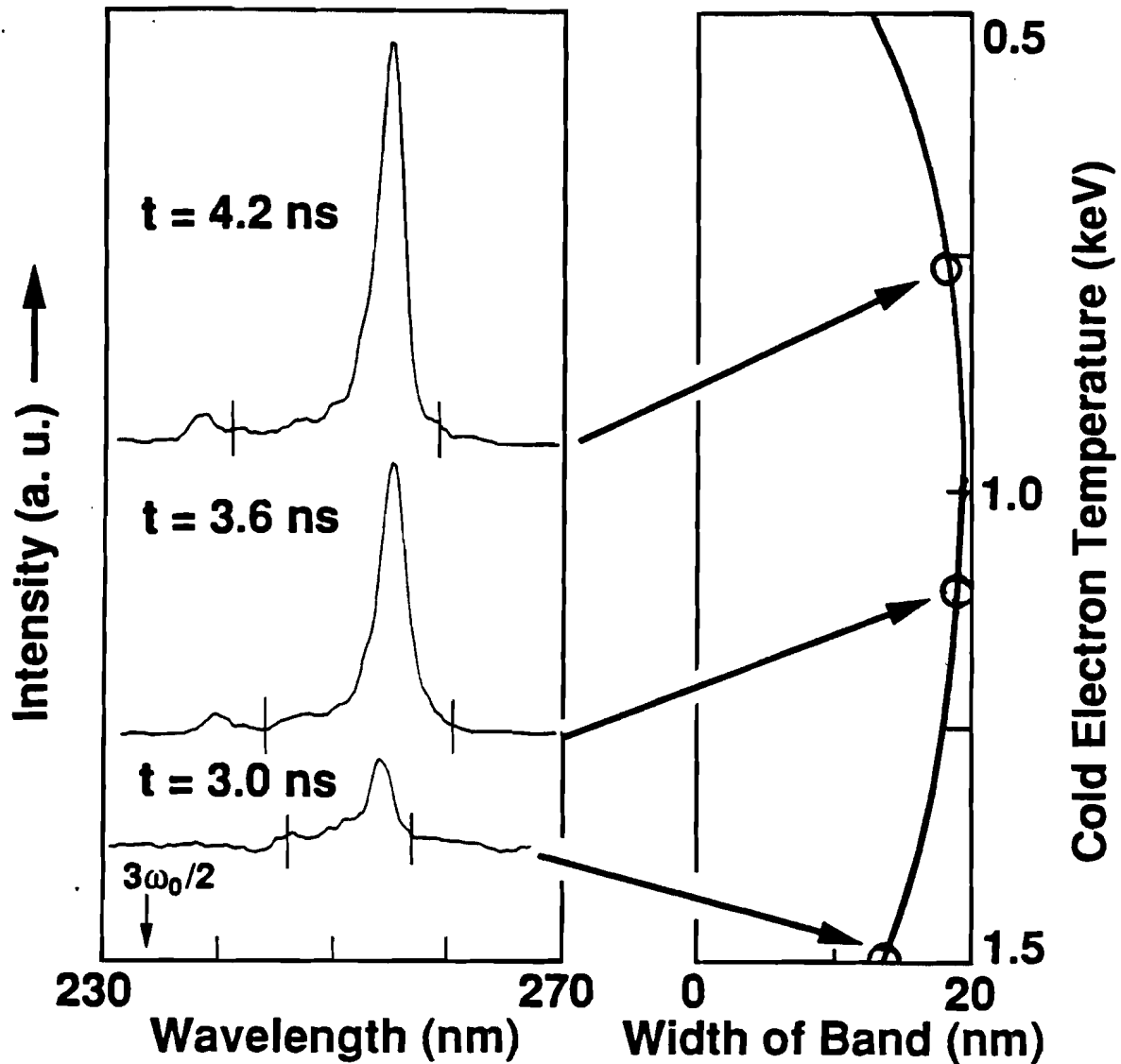


Figure IV-19. The up-scattering broadens and narrows in time, reflecting the cooling of the background plasma.

the pulse. These are clearly unrealistic. Another problem is that the ETS theory does not really predict the edge of the enhanced scattering region very well. The actual width of the band may be limited by the detection threshold of the diagnostic. This type of analysis should only be used as a guide to the physics occurring in the plasma, rather than as a detailed temperature diagnostic.

The early pulse of up-scattered light that occurs in the interaction shot (Figure IV-20) when the east cluster fires is also explained by the ETS theory. The up-scattering consists of a wide shoulder above the  $3\omega_0/2$  radiation that is an order of magnitude more intense than the scattering below  $3\omega_0/2$ . At the same time, the down-scattering consists of a wide, low-intensity shoulder between approximately 500 and 600 nm. The interaction pulse has not yet fired, but the other nine beams are still on. Each of these beams contributes to the scattering. Scattering from the west beams is not considered because geometrical effects would place the scattering well outside the observed wavelength range. The remaining four beams of the east cluster are separated from the diagnostics by angles between 39 and 74 degrees. Under the same temperature conditions, the predicted scattering band from each beam is essentially the same. The high-phase-velocity edge is fixed by the hot-electron temperature and is the same for each beam. The low-phase-velocity edge varies over a range of 11 nm for the down-scattering and 6 nm for the up-scattering. A typical calculated set of bands is shown in Figure IV-20. As has already been seen in the scattering resulting from the interaction beam, the bands calculated from the measured electron temperatures ( $T_{sh} = 26$  and  $T_c = 2.6$  keV) overestimate the amount of short-wavelength up-scattering and underestimate the amount of long-wavelength down-scattering. The measured width of the down-scattering is also larger than expected. Although the details of the observations are not reproduced exactly by the ETS theory, the approximate spectral

## East Cluster Enhanced Scattering

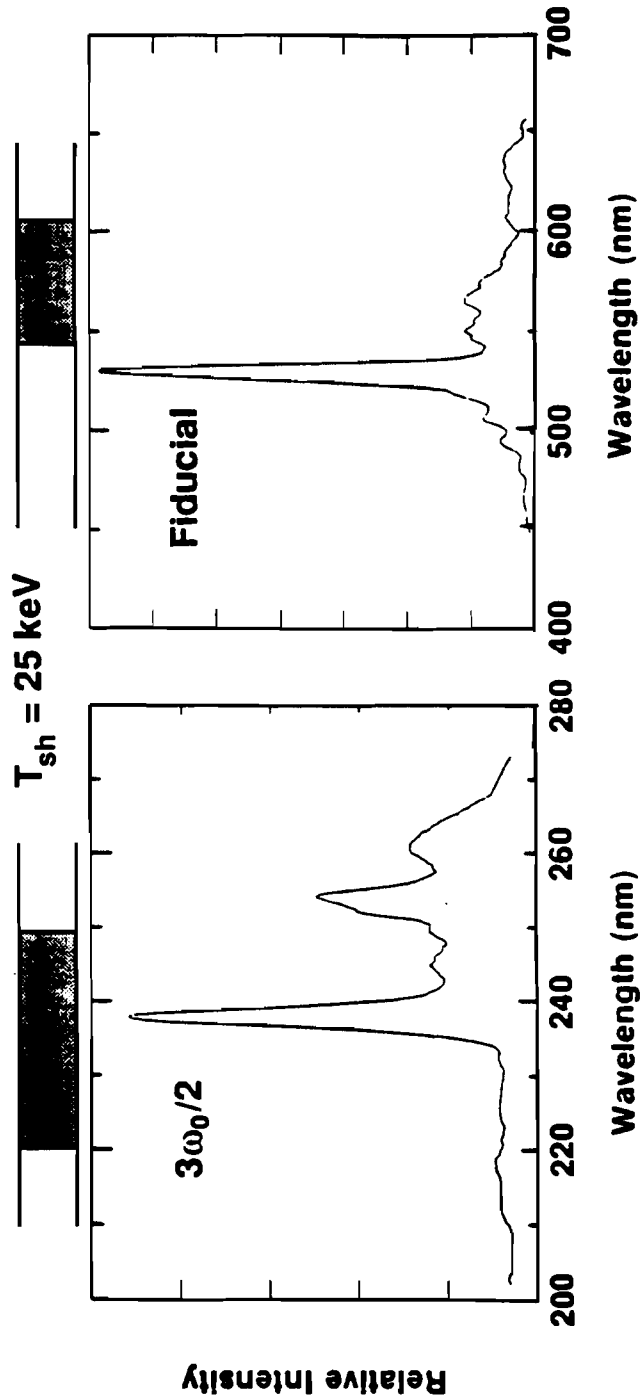


Figure IV-20. The pulse of light that occurs in the interaction shot is modelled by ETS. Shown are the predictions for the measured temperatures with  $T_c = 2.6 \text{ keV}$ . In this case, the fit is insensitive to exactly which of the four east beams is being scattered. The interaction beam has not yet been fired.

positions of the observed scattering is in agreement with the theory.

The scattering from the null shot (Figures IV-9 and IV-21) is more difficult to interpret. A single down-scattered band is emitted when the east beams first irradiate the target. It is not seen earlier because the west beams are on the other side of the target from the detectors. It turns off because the plasma density has fallen below  $n_c/4$  and there is no source of suprathermal electrons. The down-scattering extends to longer wavelengths than in the interaction shot. The up-scattered emission begins almost as soon as the west irradiation begins and does not end until the east beams have ended. The spectral position is also slightly different; here, the band extends from the three-halves feature to 255 nm. Thus, both bands are shifted to higher phase velocities than in the interaction shot, even though the measured superhot-electron temperature was lower for the null shot and the laser parameters were the same.

The up-scattered band cannot be explained by enhanced Thomson scattering emanating from a west beam because only beamline 1 is predicted to produce any up-scatter, and then at wavelengths well above those that were observed. Unlike the interaction shot, scattering from the east beams would reproduce the up-scattering spectrum quite well. The full extent of the down-scattering, however, would not be reproduced. Stimulated Raman scattering may be an alternative explanation for this spectrum.

#### **D. Summary**

In conclusion, the enhanced Thomson scattering bands from an ultra-long-scale-length plasma were observed. The spectral position of these bands is in agreement with theory. Three-halves harmonic emission from the plasma, which



## Null Shot Enhanced Scattering

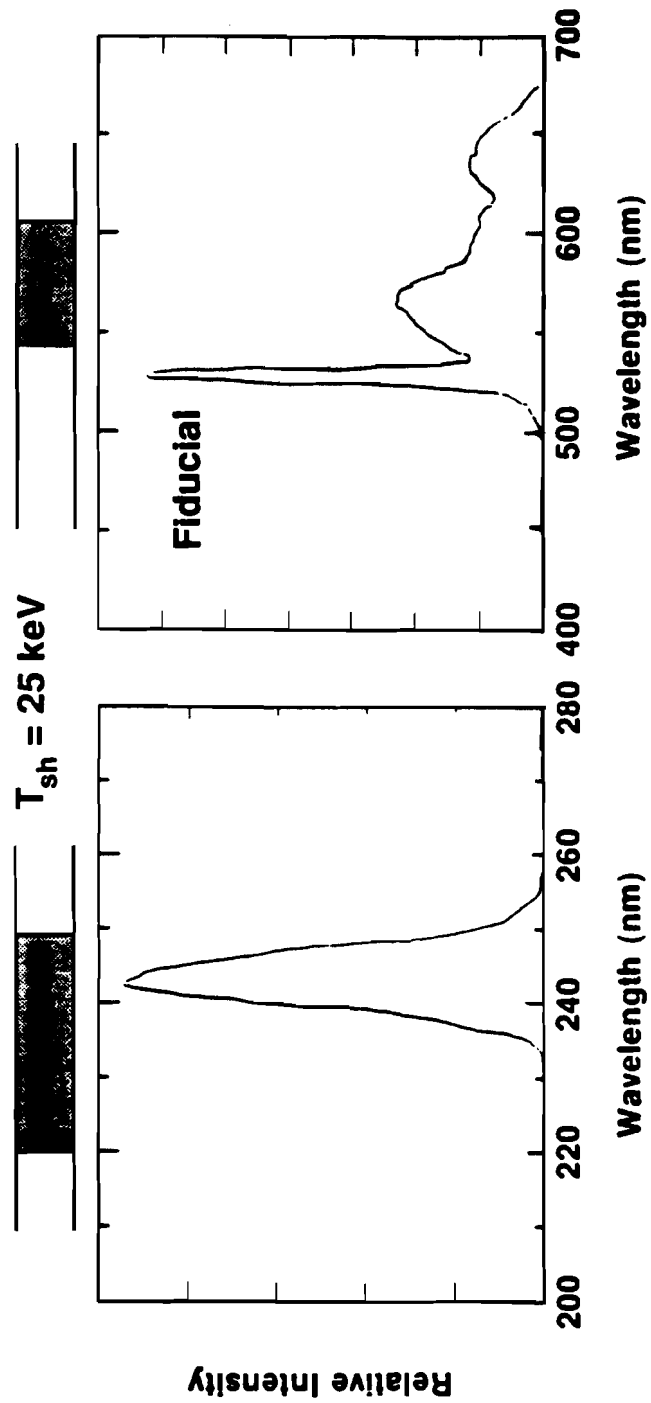


Figure IV-21. Scattering from the null shot during east beam irradiation.

implies the presence of superhot electrons, was also observed throughout the duration of the interaction. The ETS up-scattering emission disappeared when the  $3\omega_0/2$  emission ended. Null shots were also taken and showed that the interaction beam was creating ETS and  $3\omega_0/2$  signals. Earlier in the interaction, ETS from just the heating beams could be seen in both the interaction and null shots. Time-integrated electron-temperature measurements were made and were found to overestimate the instantaneous cold-electron temperature, as compared to SAGE calculations, late in the interaction. Poor agreement was found between the observed spectra and the predictions of either an absolute or a convective stimulated Raman scattering mechanism. The anti-Stokes line of either process was not identified.

## Chapter V: Single-Beam Experiments at 0.35 $\mu\text{m}$

In conjunction with the long-scale-length interaction campaign carried out at Lawrence Livermore National Laboratory, three single-beam shots were made to test a diagnostic of the stimulated Brillouin instability. The three primary ETS diagnostics (up- and down-scattering spectrometers and electron temperature diagnostic) were able to “piggyback” on these shots. This allowed a direct comparison to the GDL experiment with five important differences. First, the laser wavelength was shorter (351 nm) which meant that there would be no “hot” electrons, only “superhot” ones, because the level of resonance absorption is reduced. Second, the on-target energy was much higher (2.3 kJ) which would produce more Thomson scattered light. Third, the higher intensity produced hotter suprathermal electrons. Fourth, the plasma scale length was longer because the targets were much thinner. Fifth, and finally, a complete set of diagnostics was used allowing both up- and down-scattering to be temporally resolved.

In the rest of this chapter, the experimental parameters are defined and the spectra from the three target shots are presented. The ETS theory is then shown to successfully model the data. In addition, emission from stimulated Raman scattering was observed and the distinction between scattering from ETS and from SRS is made. This chapter concludes by summarizing the evidence for ETS in single-beam, 0.35- $\mu\text{m}$ -laser plasmas.

## A. Experiment

Three target shots comprised this experiment. Two of the targets were 3- $\mu\text{m}$ -thick pieces of mylar ( $Z=3.5$ ) and the third was a 6- $\mu\text{m}$ -thick gold target. The experiment was performed using a single beam of the Nova laser system. This was the beamline that was used as the interaction beam in the experiments described in the previous chapter. The pulse length was 1 ns in a square pulse. The laser-spot size was 250  $\mu\text{m}$ , which implied an on-target intensity of approximately  $4.8 \times 10^{15} \text{ W/cm}^2$ . The planar targets were oriented normally to the laser beam. The same diagnostics that were employed in the long-scale-length experiments were used. Namely, FFLEX for electron temperatures and two spectrally-resolved optical streak cameras at  $27^\circ$  from the target normal were used.

## B. Results

Although ostensibly identical shots, the two 3- $\mu\text{m}$ -thick plastic foil shots produced very different scattered-light spectra. The first, shot 18012208, shows three-halves harmonic emission from the start of the laser pulse that lasts about 300 ps (Figure V-1). This is consistent with SAGE simulations<sup>79</sup> that show burn-through at 225 ps (the  $n_c/4$  surface burns-through at 300 ps, on-axis) and LILAC simulations<sup>81</sup> that show burn-through between 250 and 300 ps. At 254 nm, a wavelength where enhanced Thomson scattering was previously observed, the scattered light was less than 5% as intense as that at  $3\omega_0/2$ . The peak of this scattering also occurred later than the three-halves peak. This is consistent with the supposition that superhot electrons created at the quarter-critical density are responsible for enhanced scattering. The peak of the down-scattering occurred 200 ps after the up-scattering peak.

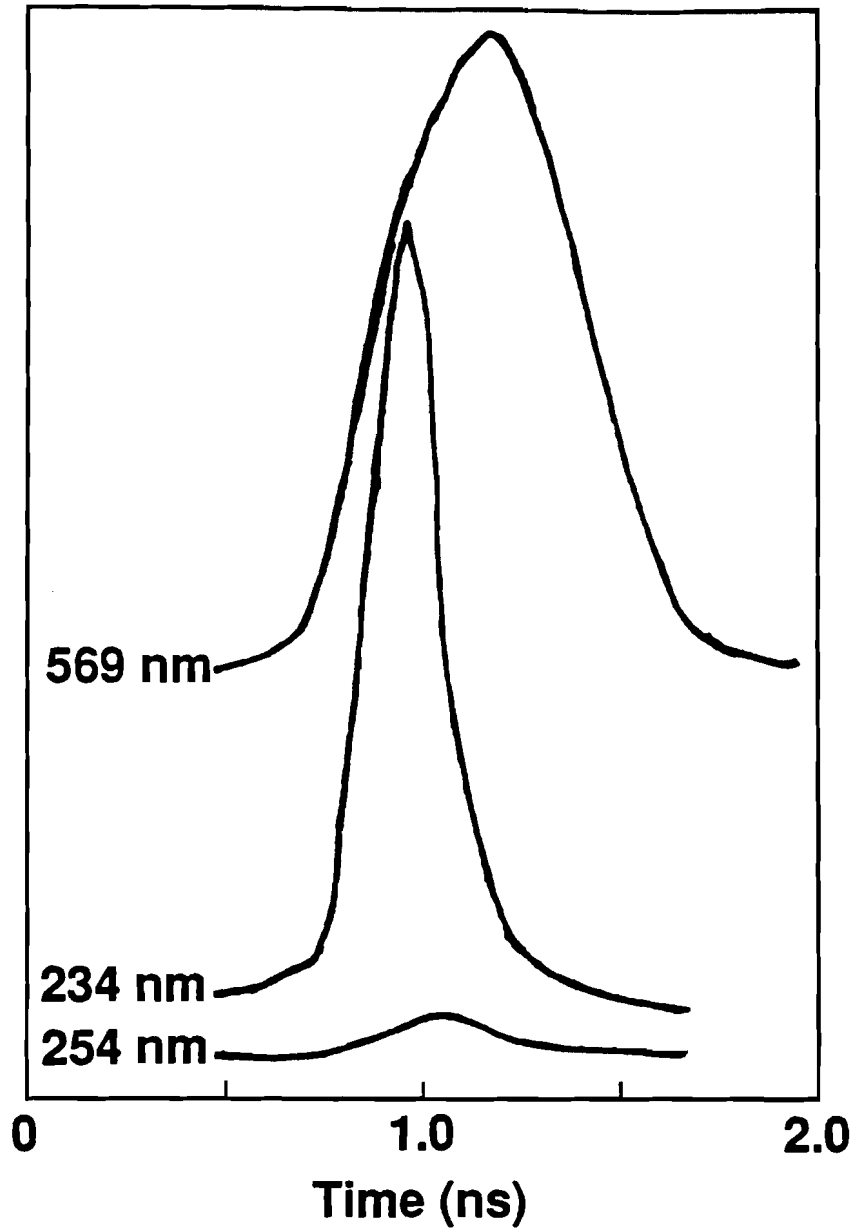
**Shot 18012208**

Figure V-1. Temporal evolution of a CH-target shot. The down-scatter emission peaks 200 ps after the  $3\omega/2$  emission does.

The scattered-light spectrum from shot 18012208 (Figure V-2), at approximately 0.5 ns into the interaction, shows that the three-halves signal is the dominant feature in the observed spectral region and that the scattering at 254 nm is a part of the  $3\omega_0/2$  signal. The down-scattered signal shows two distinct peaks, one between 550 and 600 nm and one between 650 and 702 nm. Splitting of the  $\omega_0/2$  signal (at 702 nm) is not apparent.

The second shot, 18012906, shown in Figure V-3, has some discrepancies, particularly in the three-halves emission that shows two distinct emission periods. The half-harmonic feature, like the three-halves a signature of two plasmon decay, is correlated with the first peak. Up-scattering at 254 nm is delayed slightly with respect to the  $3\omega_0/2$  signal and the down-scattering (at 569 nm) peaks at the minimum of the  $3\omega_0/2$  signal.

The scattered-light spectra, as well as the time evolution of the  $3\omega_0/2$  signal, of shot 18012906 differs from shot 18012208. The spectrum also changes drastically during the irradiation. Two different times will be considered. Time I is at the first peak of the  $3\omega_0/2$  emission and Time II is at the second peak. Time I up-scattering (Figure V-4) shows  $3\omega_0/2$  emission (cf. Figure V-3) and a very strong ETS scattering band that is 16 times more intense than the three-halves. Time II up-scattering (Figure V-5) has a  $3\omega_0/2$  peak comparable in intensity to Time I (again, cf. Figure V-3) and a much weaker remnant of the ETS band at 254 nm. The down-scattered spectrum has also shifted. Figure V-4 shows that at Time I, the down-scattering occurs in one large band that starts near 500 nm but does *not* extend to 700 nm, being cut off at 690 nm. The  $\omega_0/2$  signal is distinct and separated from the ETS signal. At the later Time II (Figure V-5), the peak of the down-scattering band has shifted to shorter wavelengths and, although the band also cuts off at 500 nm, the long wavelength edge is cut off at a

## Shot 18012208

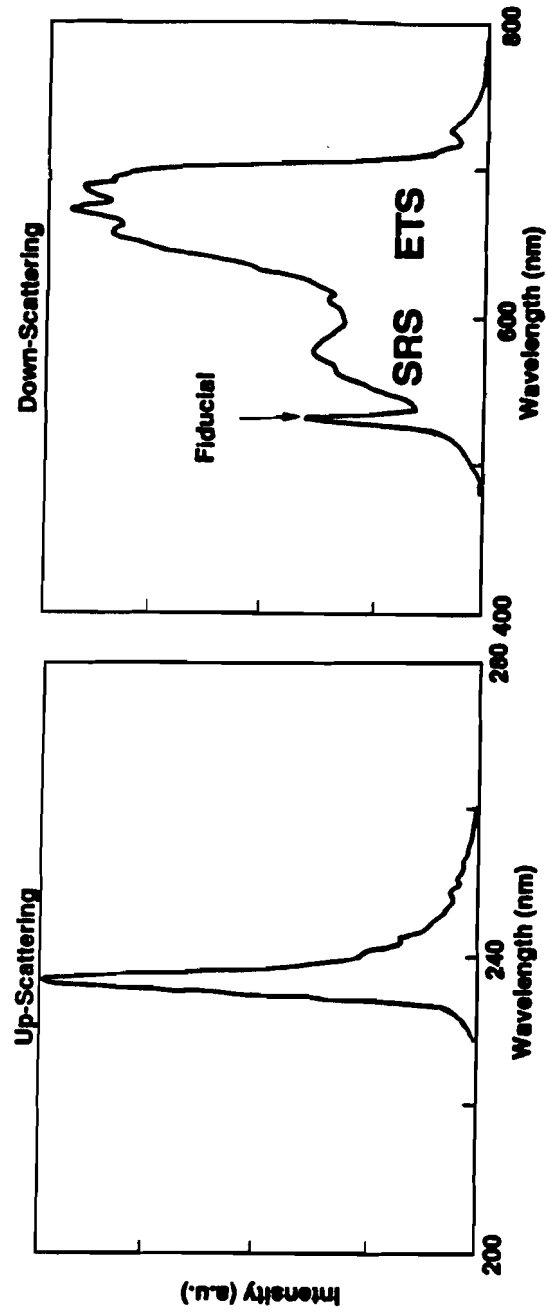


Figure V-2. This CH-target shot shows  $3\omega_0/2$  emission, ETS near  $\omega_0/2$ , and an SRS band near 600 nm.

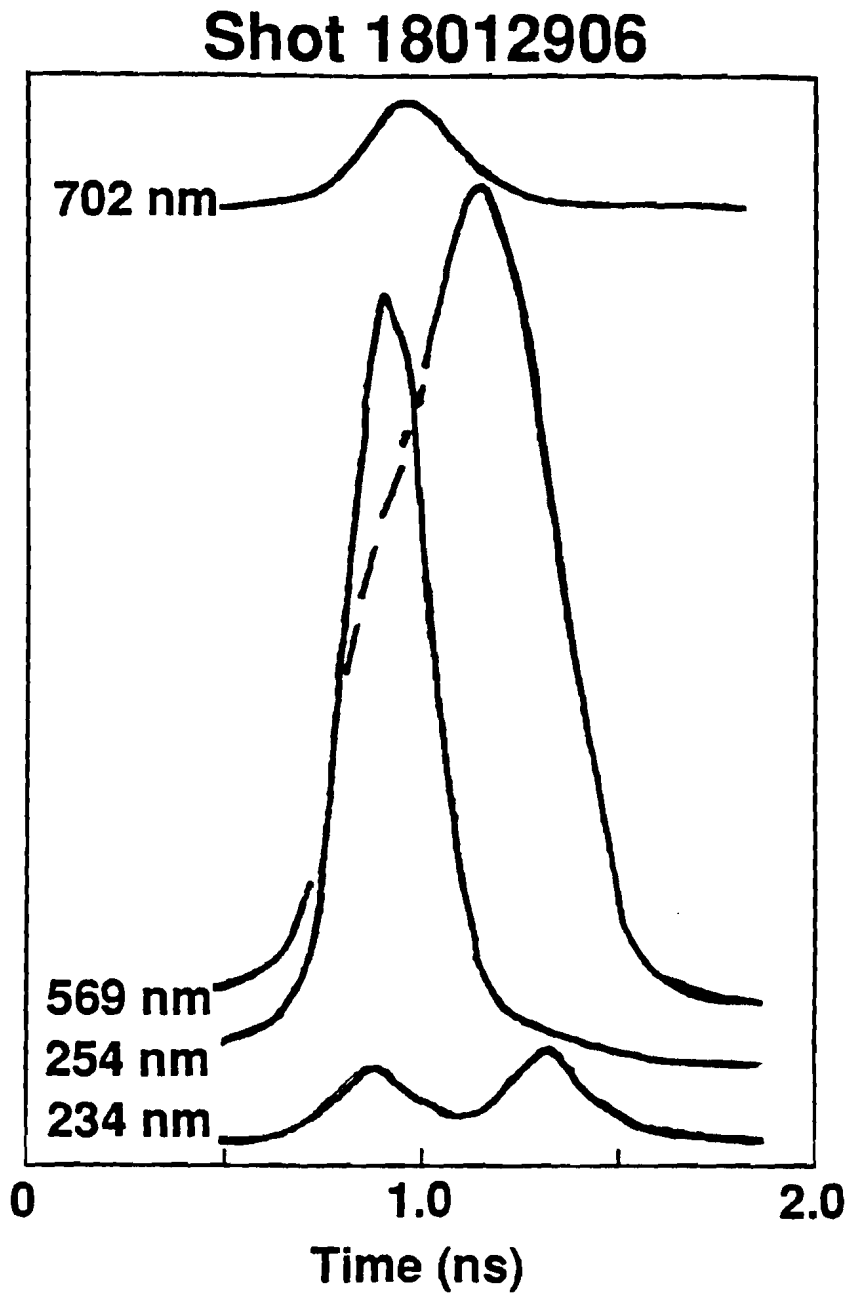


Figure V-3. Anomalous double-peaked behavior of the  $3\omega_0/2$  signal. The up-scattering is correlated with the first peak. Half-harmonic emission occurs earlier than the down-scattering does.



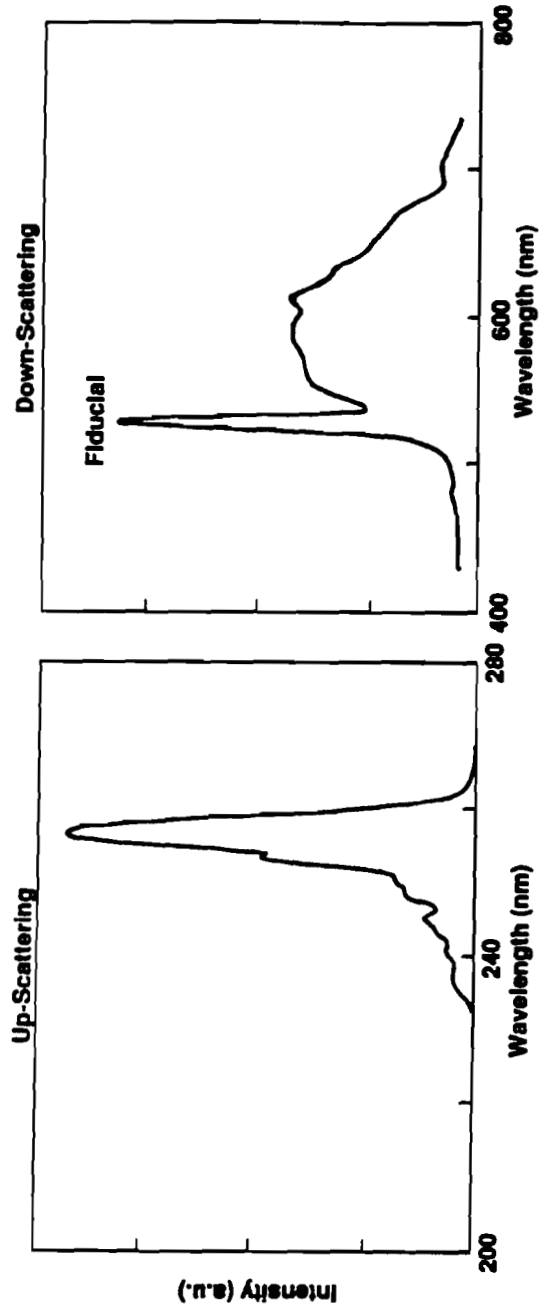
**Shot 18012906: Time I**

Figure V-4. At the first peak of  $3\omega/2$  emission, an unmistakable ETS band is present in the up-scattering. Only the SRS band is identifiable in the down-scattering.

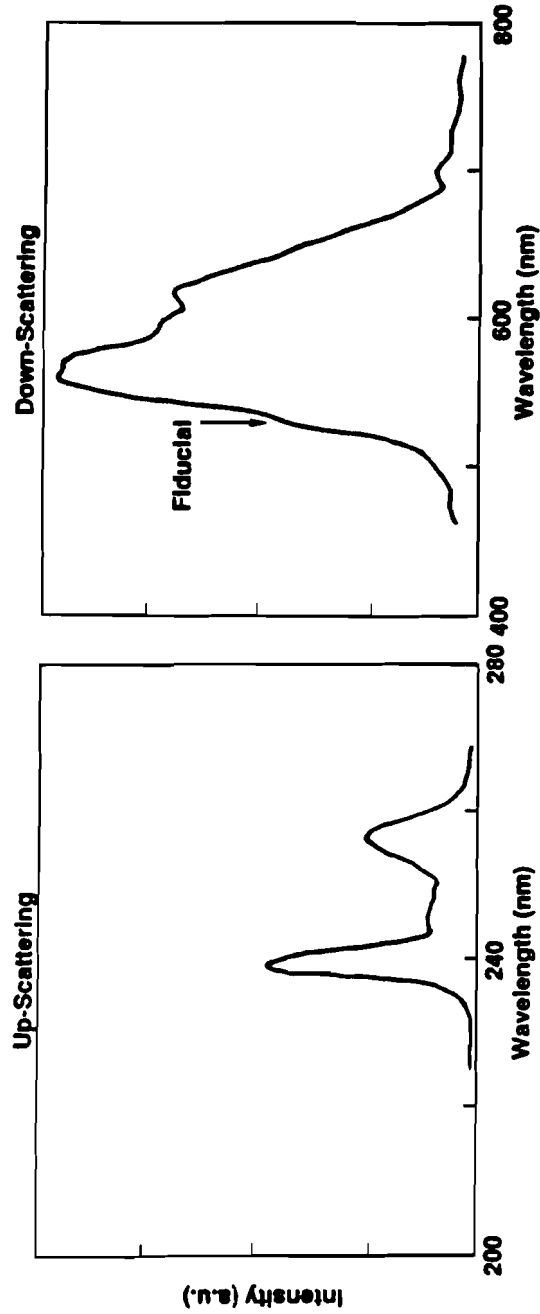
**Shot 18012906: Time II**

Figure V-5. At the second time, the up-scattering has diminished in intensity. The down-scattering now shows two strong peaks. The vertical scale of the up-scattered spectrum is ten times smaller than in the previous figure. The down-scattering spectrum has the same scale.

much shorter wavelength, 650 nm. The shape has also changed.

The Au target presents an opportunity to test the effects of target Z on ETS scattering. The scattered-light spectrum is presented in Figure V-6. The three-halves harmonic partly obscures the presence of an ETS band in the up-scattering spectrum. The down-scattering was mostly limited to a well-defined band between 600 and 700 nm. There is also a small band, distinct from the most intense scattering, at longer wavelengths than 700 nm (at lower frequencies than  $\omega_0/2$ ). The origin of this scattering band is unknown.

Table V-1 summarizes the laser conditions and the measured suprathermal-electron temperatures for the three single-beam shots. The electron temperatures are more suspect than they were for the multi-beam shots because of large scatter from each detector. There is no known reason for the large scatter. The cold temperatures are, as always, questionable because only two detectors were used to fix this component. In general, however, the electron temperatures were much higher than in the multi-beam shots. These "exploding-foil" targets had less mass than the multi-beam shots and the laser intensity was higher because of the shorter pulse length. Shot 18012906 had measured cold and superhot temperatures of 5.5 and 31 keV, respectively, while shot 18012208 had a superhot temperature of 40 keV. No cold temperature was measured for this shot. The Au target produced a higher superhot temperature (49 keV) and a lower cold temperature (4.6 keV) than the CH targets did.

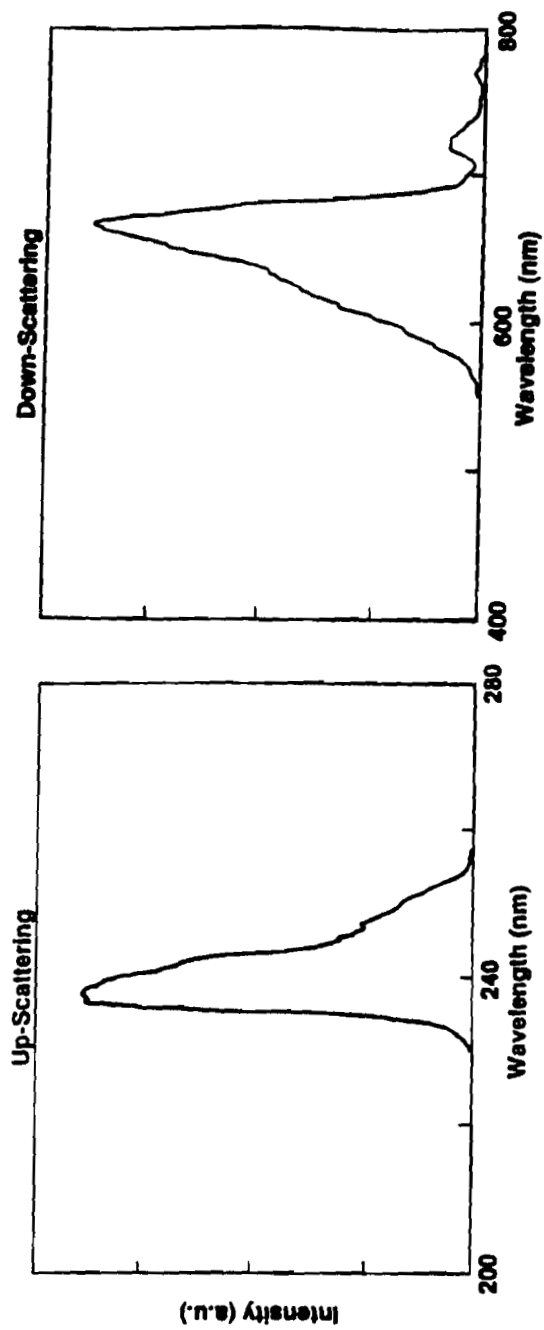
**Au Target: Shot 18010809**

Figure V-6. The Au target shows no SRS band in the down-scattering. An ETS band may be discerned in the up-scattering spectrum.

**Table V-1: Single-Beam Shots at LLNL**

Shot Number	18010809	18012208	18012906
Target Material	Au	CH	CH
Target Thickness ( $\mu\text{m}$ )	6	3	3
<b>351-nm Energy (kJ)</b>	2.4	2.3	2.2
<b>Intensity (<math>\times 10^{14}</math> W/cm<sup>2</sup>)</b>	48	48	45
<b>Electron Temperatures (keV)</b>			
Cold Temperature	4.6	—	5.5
Superhot Temperature	49	40	*31
<b>Ionization State (Z)**</b>	26 to 35	3.5	3.5

\* Large scatter

\*\* Determined from LILAC simulations<sup>81</sup>

### C. Discussion

Two different processes appear to be occurring in these shots: enhanced Thomson scattering (ETS) and stimulated Raman scattering (SRS). The ETS process is especially evident in the down-scattered spectrum of shot 18012208 (Figure V-2). The long-wavelength peak, between 600 and 700 nm can be reproduced using the measured superhot temperature of 40 keV. Because a cold temperature could not be determined from the x-ray data, it was assumed to be the same as the second shot, 5.5 keV. The quality of this fit is shown in Figure V-7 where the phase velocities of the scattering electron-plasma waves are plotted. In general, the agreement is quite good, especially for the low-phase-velocity (short-wavelength) cutoff. The up-scattered signal is predicted to be outside the wavelength range of observation between wavelengths of 185 and 210 nm.

The second down-scattered peak, between 550 and 600 nm, may be due to stimulated Raman scattering. The density profile of a thin foil may be considered to be parabolic at the highest density with an exponential tail on the laser-irradiated side. Figure V-8 shows the two different scale lengths involved. The density profile shown is from a LILAC simulation just after the foil burns-through. The parabolic part of the profile has a scale length,  $L_p$ , equal to 55  $\mu\text{m}$  where the profile was assumed to be  $n = n_0(1 - x^5/L_p^2)$ . The exponential part of the plasma has the profile  $n = n_0 \exp(-x/L)$  with  $L = 190 \mu\text{m}$ . The exponential scale length ( $L$ ) is used in the comparison of this experiment with those described in Chapters III and IV. In a parabolic profile, the SRS intensity threshold is given by<sup>82</sup>

$$I = \frac{5 \times 10^{15}}{\lambda_0^{2/3} L_p^{4/3}} T_e^{1/3} \left( \frac{n}{n_c} \right)^{-1/3} \frac{W}{\text{cm}^2}, \quad (\text{V-1})$$

where  $\lambda_0$  and  $L_p$  are expressed in microns,  $T_e$  in eV, and the critical density is  $n_c$ . For

## Shot 18012208

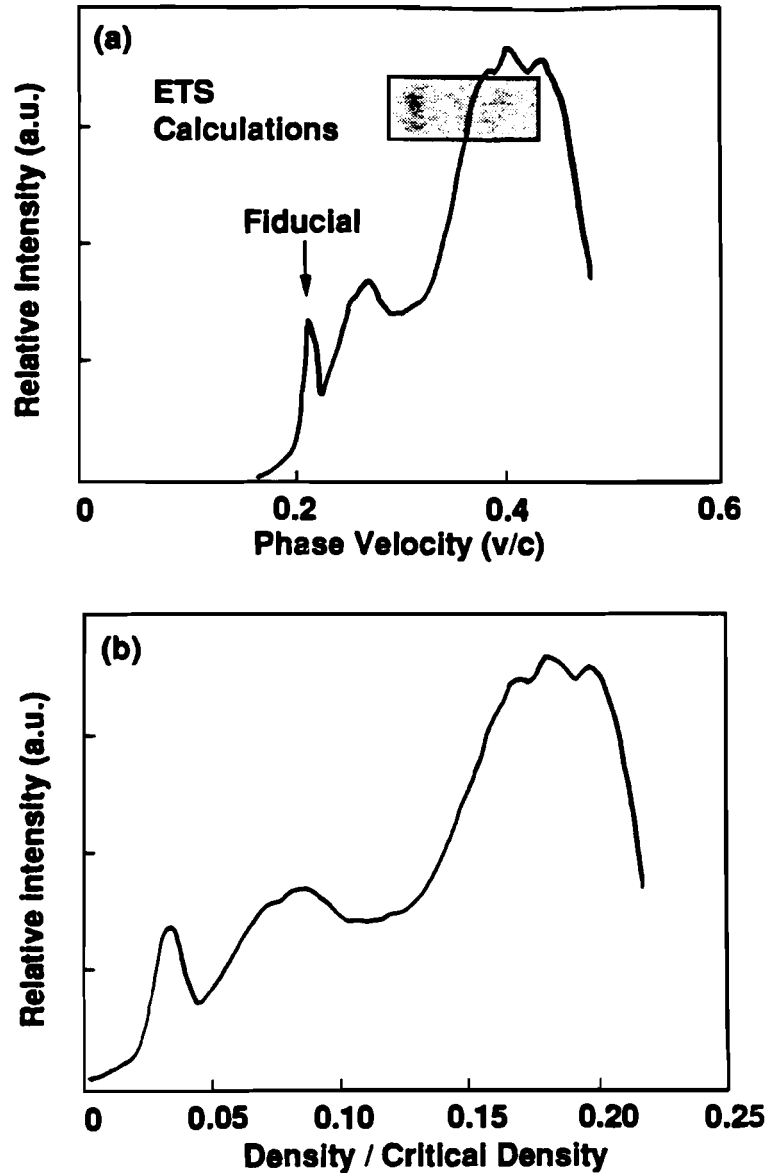


Figure V-7. The down-scattering from a CH-target is well-modelled by the ETS theory. A comparison between the theory and the absolute magnitude of the electron-plasma-wave phase velocity in the direction of the density gradient is shown in (a). In (b), it is seen that the down-scattering is from densities below  $n_c/4$ .

## Density Profile at Burn-Through

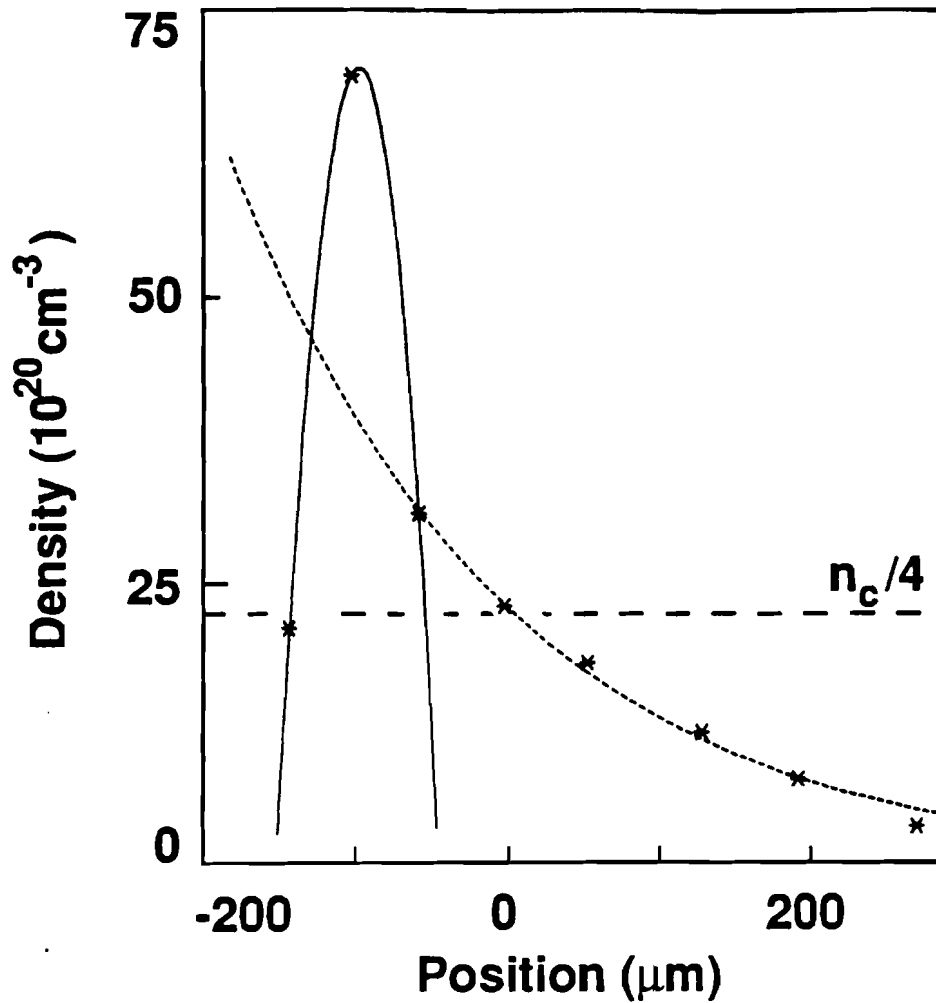


Figure V-8. When the plasma burns-through at 225 ps, a parabolic scale length of 55  $\mu\text{m}$  and an exponential scale length of 190  $\mu\text{m}$  are present in the plasma. The density profile is from a LILAC simulation.



the conditions of shot 18012208 (using  $n/n_c = 0.08$  as suggested by Figure V-7[b]), the intensity threshold is  $2 \times 10^{15}$  W/cm<sup>2</sup>. As Eq. (V-1) shows, the threshold is lower at higher peak densities. As the irradiation continues, the peak density falls and the entire plasma can be characterized by a parabolic profile. Figure V-9 shows that at 500 ps, the peak density is about  $0.12n_c$  and the parabolic scale length is  $680 \mu\text{m}$ . The SRS intensity threshold is then  $6 \times 10^{13}$  and is easily satisfied. The linear threshold is  $1.5 \times 10^{15}$  for the laser-irradiated ( $x > 0$ ) side of the target. Considering just the intensity threshold implies that any SRS observed is thus much more likely to be caused by the density profile being parabolic than any other cause, although the linear-profile threshold is also satisfied.

For Raman scattering, the electron density at the origin of the scattering determines the scattered-light frequency. Working backwards from the dispersion relation,

$$\omega_s^2 = \omega_p^2 + c^2 k_s^2, \quad (\text{V-2})$$

shows that the scattering is from the density range  $0.05n_c$  to  $0.11n_c$ . It also follows that the peak scattered-light intensity, which occurs at  $0.08n_c$ , corresponds to the density where the Raman gain is the largest. In a parabolic profile, this is at the peak density so that as the peak density falls, the scattered light should shift to shorter wavelengths (higher frequencies). This is not the case here. The Raman band remains fixed in wavelength throughout the interaction. This implies that because SRS is occurring at a fixed density, the linear-profile case is applicable, contrary to the intensity threshold implications of a parabolic profile.

Stimulated Raman scattering may also provide a source of superhot electrons, if the instability is absolute. The instability is absolute at the  $n_c/4$  density surface, but this would produce emission with frequency  $\omega_0/2$ , which was not seen. Stimulated Raman

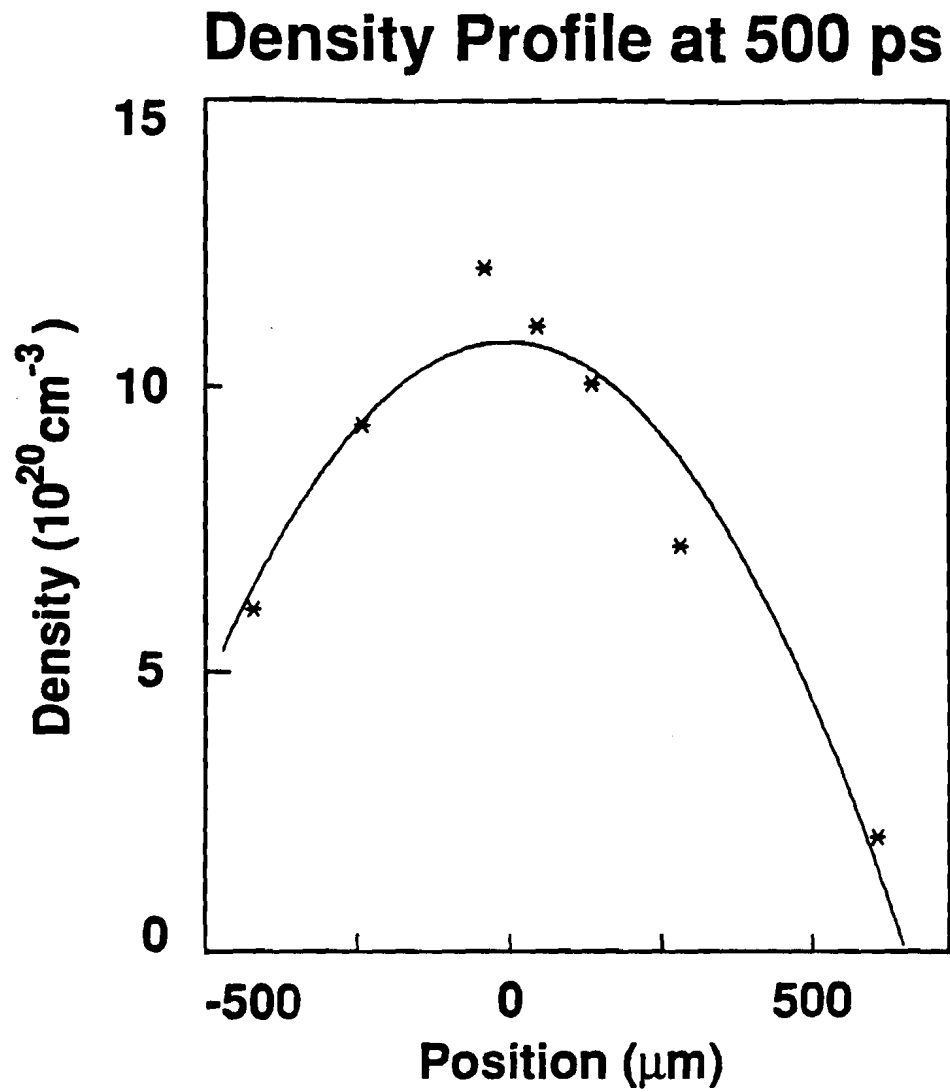


Figure V-9. At 500 ps into the same LILAC simulation, the peak density has fallen below  $n_c/8$  and the plasma has a parabolic scale length of  $680 \mu\text{m}$ .

scattering at the extremum of an underdense target is also absolutely unstable<sup>83-85</sup> and produces radiation at a frequency given by Eq. (V-2). The superhot electrons produced may certainly have a different characteristic temperature than those produced by two plasmon decay so that it is possible that two superhot temperatures may simultaneously exist in the plasma. The FFLEX temperature diagnostic would not necessarily be able to measure both components.

The second CH-target shot, 18012906, also had the same Raman band seen in Figure V-4 with no apparent ETS band. The measured electron temperatures ( $T_c = 5.5$  keV and  $T_{sh} = 31$  keV) predict up-scattering at wavelengths below 210 nm and down-scattering above 500 nm. Enhanced scattering was not observed at either wavelength band. The up-scattered signal, however, has a strong ETS band at approximately 254 nm. This corresponds to scattering from electron-plasma waves enhanced by 15 keV electrons with a 1 keV background. The corresponding down-scattering band occurs between 480 and 580 nm. In Figure V-4, at time I, this band overlaps the Raman signal and the two may not be differentiated. At time II, shown in Figure V-5, two peaks may be discerned in the down-scattered spectrum. Although the width of the band is the same, peaks at 550 and 600 nm are now evident. The 550-nm peak is the ETS band and the longer wavelength peak is the same Raman band as before. The up-scattered spectra shows that the 254-nm peak has decreased in intensity to a level below the  $3\omega_0/2$  signal. The down-scatter lags behind the up-scatter in both CH-target shots, shown in Figures V-1 and V-3.

The Au-target shot shows still different behavior. The up-scattering consists of the three-halves feature joined with an ETS feature at wavelengths slightly less than in the CH shots. The down-scattering peak is much closer to 702 nm, which corresponds to scattering from  $n_0/4$ . The peak, however, is not at exactly  $\omega_0/2$ ; it is separated from

$\omega_0/2$  by approximately 40 nm. While it is tempting to identify this band as produced by SRS at  $n_c/4$  and lower densities, its origin is more logically explained by ETS. The wavelength position of the band is similar to that measured from a CH target, Figure V-2. This is expected because target Z has little effect on the position of the ETS bands. The gap near  $n_c/4$  could be due to profile steepening, but is more readily explained by the finite velocity of the suprathermal electrons.

The SRS band is absent because the Au target will not burn-through during the laser pulse so that a parabolic profile is never formed. The larger mass of the Au target also reduced the plasma scale length. The absence of scattered light from the quarter-critical surface, where the SRS growth rate is highest, implies that the SRS threshold may only be surpassed in hot spots. Even where the threshold is satisfied, the growth rate is reduced by the shorter scale length. The entire spectrum may be explained by enhanced Thomson scattering rather than stimulated Raman scattering.

#### D. Summary

Intense, single-beam, 351-nm irradiations of thin CH and Au targets were made. The measured cold- and superhot-electron temperatures were much higher than in the multi-beam, long-scale-length experiments. The exponential scale length was determined from LILAC simulations to be approximately 190  $\mu\text{m}$ . The scattered-light spectra showed that both enhanced Thomson scattering and stimulated Raman scattering were present. The ETS predictions, using the measured temperature, were in good agreement with one CH-target experiment. Much lower temperatures needed to be invoked in order to model the other two target shots. However, the shift of the scattered light in the CH target is consistent with a decreased electron temperature. A

lower temperature was indeed measured on this shot. The peak of the down-scattering was found to lag behind the up-scattering by about 200 ps.

Raman scattering, peaked at 600 nm, was observed on the two CH shots. The wavelength of the scattering band did not shift even as the peak plasma density dropped from overdense to below  $0.1n_c$ . This is inconsistent with SRS from a parabolic profile because the largest emission is expected from the peak density where the instability growth rate is highest. A shift to lower wavelengths is therefore expected. The intensity threshold for SRS, for both parabolic and linear density profile plasmas, was exceeded.

The Au target showed the same ETS signal but had almost no SRS signal. The target did not burn-through and the shorter scale length, because of the larger target mass, increased the SRS threshold to an inaccessible value.

## Chapter VI: Discussion and Conclusion

The enhanced Thomson scattering theory (ETS) has been shown, in the three different experiments reported in this dissertation, to accurately reproduce the scattered-light spectrum between the laser frequency half-harmonics from a submicron-laser plasma interaction. In particular, the ETS theory accurately reproduces the position of the down-scattered band, the appearance and position of the up-scattered band, and explains the appearance of both scattered-light bands even below the convective stimulated Raman scattering theory threshold. The three experiments were able to test the ETS theory under widely varying plasma conditions. The success of the theory in modelling the experimental results is presented below. The possible causes of measured deviations from the theoretical calculations are then discussed. Surprisingly, many of the approximations and assumptions of the model are quite reasonable and relaxing them would have little effect on the predicted spectrum. This model is remarkably robust, being applicable to experiments whose scale lengths vary over two orders of magnitude, whose superhot-electron temperatures vary by a factor of 2, whose pump laser wavelength was either 0.527 or 0.351  $\mu\text{m}$ , and whose average laser intensity varies by a factor of 6.

### A. Success of Theory

Enhanced Thomson scattering (ETS), as used in this dissertation, describes the non-stimulated Raman scattering of laser light from electron-density fluctuations in a plasma which have been enhanced by the presence of suprathermal electrons.<sup>12,13</sup> This

process is different than stimulated Raman scattering (SRS), the coupling between the laser and plasma waves, which is an instability, has a threshold intensity, and whose growth rate is nonlinear. The ETS theory has successfully modelled experiments under three different plasma conditions. Using only measured electron temperatures, or the temperatures calculated in simulations, the theory was able to successfully reproduce the spectral positions of both the up-shifted and down-shifted scattered-light bands.

The differing laser and plasma conditions of the three experiments are contained in Table VI-1. The first experiment was a low-energy, low-intensity, single-beam experiment using the GDL system at the Laboratory for Laser Energetics at the University of Rochester. The laser wavelength was 0.527  $\mu\text{m}$ . Thick CH targets that produced a scale length of 80  $\mu\text{m}$  were used. Up-scattered light was only rarely observed because the nominal on-target intensity was too low to produce enough superhot electrons to amplify density variations and enhance the scattered-light level. The up-scattering observed in this experiments (as in Figure III-6) is postulated to be caused by the presence of random hot spots in the laser beam where the intensity may be several times higher than nominal. Only in the hot spots may enough superhot electrons be produced to initiate the up-scattering of ETS. The up-scattering was also difficult to detect because of the poor dynamic range of the film (Kodak 2495) used to record the spectra.

Down-scattered light was observed (Figure III-5) on every shot. Because down-scattering has a lower superhot-electron fraction than up-scattering does, it was expected that down-scattering would occur more often.

The data was modelled very well by the ETS theory. Simultaneous up- and down-scattered spectra are shown in Figure III-8. The scattering bands due to superhot electrons were in reasonable agreement with the actual temperature measurement, given

**Table VI-1: Typical Plasma Conditions**

<b>Series</b>	<b>LLE</b>	<b>Long-Scale- Length</b>	<b>Single-Beam</b>
<b>Chapter</b>	<b>III</b>	<b>IV</b>	<b>V</b>
<b><u>Laser Conditions</u></b>			
Laser System	GDL	Nova	Nova
Laser Wavelength (nm)	527	351	351
Number of Beams	1	10	1
Pulse Shape	Gaussian	Square	Square
Pulse Length (ns)	0.6	2	1
Energy (J)	60	19,000	2,300
Intensity ( $\times 10^{14}$ W/cm <sup>2</sup> )	8	9	48
<b><u>Plasma Conditions</u></b>			
Target Material	CH	CH	CH
Target Thickness ( $\mu\text{m}$ )	50	15	3
Scale Length ( $\mu\text{m}$ )	80	1,600	200
Scale Length ( $\lambda_0$ )	150	5,000	600
<b><u>Electron Temperatures (keV)</u></b>			
Cold Temperature	1.5	2.7	5.5
Hot Temperature	5 to 10	—	—
Superhot Temperature	> 15	25	35



the accuracy of the x-ray diagnostic. In addition, the presence of resonance absorption electrons of less than 10 keV was inferred from the presence of a second up-scattering band.<sup>32</sup> This electron component was impossible to detect with the configuration of the x-ray diagnostic. While the superhot down-scattering threshold was less than the up-scattering threshold, the reverse was true for the hot-electron threshold. Therefore, the hot-up-scattering band was produced, but the corresponding down-scattering band was not because of the high hot-electron threshold of this band.

The second experiment utilized the high power and flexibility of the Nova laser system at the Lawrence Livermore National Laboratory. Nine Nova beams, operating at 0.351  $\mu\text{m}$ , formed a long-scale-length plasma. The tenth, or interaction, beam was delayed until the plasma scale length was estimated to be  $5,000\lambda_0$ . Simultaneous time-resolved measurements of both the up- and down-scattered-light spectrum were made; an example is shown in Figure IV-4. Enhanced Thomson scattering from both the heating beams and the interaction beam was observed. The predicted width and position of the bands were in good agreement with the measurements, as illustrated in Figure IV-15. Because the two spectra were observed at the same angle with respect to the symmetry axis of the laser, the observed scattering originated at different densities, Figure IV-16, and scattered from different electron-plasma waves, Figure IV-17. These considerations were taken into account in producing the predictions of Figure IV-15. It should be emphasized that a plot of the calculated scattering bands, like Figure II-4, has no inherent symmetry in terms of electron-plasma-wave frequency, density at the origin of scattering, or wavelength. The theory only calculates the scattering in one direction, assuming that all electron-plasma waves exist at all densities below critical density.

The final set of experiments was performed using a single arm of the Nova

laser. These experiments produced a hot, medium-scale-length plasma because the laser intensity was higher ( $5 \times 10^{15}$  W/cm<sup>2</sup>) and the wavelength shorter (0.351  $\mu$ m) than in the GDL experiments. ETS was observed on two CH-target shots and one Au-target shot. The two CH targets did not behave exactly the same. The spectrum on one could be modelled with the measured temperatures, Figure V-7, but the second required temperatures below those measured. The temperature of the second shot was measured to be lower, however, so that qualitatively, the behavior was as expected.

Another down-scattered band, attributed to stimulated Raman scattering (SRS), was present in both CH-target shots. The intensity threshold and growth rate of SRS depends on whether the density profile is parabolic or linear. The highest growth rate in a parabolic profile occurs at the peak density where the instability is absolute. For the targets in these experiments, the parabolic-thresholds were more easily met. The scattered-light frequency is proportional to the density at the origin of scattering, for either a parabolic or linear profile. The scattered-wavelength peak did not shift during the interaction, as would be expected if the peak density of plasma were decreasing as the plasma burned-through, implying that the density was not parabolic. This anomalous result is not understood.

The Raman band was absent in the Au-target shot (Figure V-6) although the ETS bands were easily discernable. The larger target mass decreased the sound speed, reducing the scale length and preventing the formation of a parabolic profile. No Raman thresholds were then exceeded.

## B. Deviations from the Theory

Although the enhanced Thomson scattering theory was able to reproduce the spectral positions of the two scattered-light bands, the high- and low-phase-velocity cutoffs were not always exactly right. Comparisons between experiment and theory are most easily made in phase-velocity space of the electron-plasma wave. Because of limitations in the image analysis software and in the photographic film used as detectors, detailed comparisons of the GDL data could not be made. In general, however, the width of the scattering bands is overestimated. More detailed comparisons can be made with the data taken at Lawrence Livermore National Laboratory. The calculated spectrum is compared to the actual data in Figure IV-12. It is apparent that although the spectral positions of the two bands are correctly reproduced, the width of the bands is overestimated in the up-scattering and underestimated in the down-scattering. This is shown more explicitly in Figure IV-15, where the scattering is plotted in terms of phase velocity. The down-scattering is actually in better agreement with the theory than was evident from Figure IV-12. The up-scattering does not extend to phase velocities as high as those predicted.

The single-beam shots also show some of these problems. The down-scattering, shown in Figure V-7, extends to higher phase velocities than predicted. Many of the theoretical calculations require an asymmetric phase velocity distribution to correctly, and simultaneously, match both the up- and the down-scattering spectra. In the rest of this section, several of the assumptions made about the laser plasma, in both the derivation of the ETS theory and the application of the theory to the experiments, will be examined.

The first assumption examined is the effect of a tilted density gradient. It was assumed that the plasma density gradient was perpendicular to the target plane for all of

the ETS calculated spectra and phase-velocity plots. Relaxing this assumption would change only the magnitude of the observed electron-plasma wave vector. While the direction of  $\mathbf{k}_{epw}$  is different for up- and down-scattering, the difference is small, and this correction to the phase velocity would be small. Not only is it a small correction, it would also tend to shift both scattering bands towards higher, or both to lower, phase velocities, and the shift would be of the same magnitude. Because an asymmetric shift of the up-scattering band is needed to reproduce the data, this correction is not important.

The finite angular extent of the irradiating beam may affect the wavelength range of the scattered-light bands and must be considered. In order to achieve high intensities at the target plane, the laser beams must be focused to a small spot. Both the GDL and Nova beams were focused using optics as fast as  $f/3.6$ , which corresponds to an opening angle of  $16^\circ$  for each beam. All of the experiment-to-model comparisons in this dissertation were made assuming that the angle of interest was the angle between the observation angle and the center of the beam. For instance, the Nova diagnostics were  $27^\circ$  from the axis of the interaction beam. Scattering from other oblique rays may also be important.

The center ray does provide a good approximation to the average ray, although different parts of the laser beam scatter from different electron-plasma waves. The denominator of the scattered power spectrum [Eqs. (II-110) to (II-113)], which determines where a scattering band is possible, depends only weakly on the angles of observation and the target normal, so that deviations of a few degrees do not make large changes in the position of the scattered-light band. Rays closer to the observation direction are more backscattered than other rays. At other angles, the scattering electron-plasma waves may be traveling in a direction that is more closely the direction

of the density gradient. These waves will have higher phase velocities in the density-gradient direction, implying scattering at different frequencies. The closer the direction of propagation of the electron-plasma waves is to the density gradient, the lower the number of suprathermal electrons needed to produce scattering. This may also affect the shape of the scattered-light spectrum, because while the number of suprathermal electrons in a given plasma volume is fixed, the amount of amplification of each electron-plasma wave depends on its wave vector. The amount that each electron-plasma wave is above threshold will vary from one ray to the next, which may explain why one portion of the scattered-light band is amplified more than another. The finite divergence of the laser beam causes the scattering bands to widen slightly and may partly explain the spectral shape of the bands.

The ETS theory assumes that the suprathermal electrons are produced in a monoenergetic, unidirectional burst traveling down the density gradient. Light is scattered by electron-plasma waves that travel at all different directions with respect to the density gradient. Each is enhanced by the suprathermal electrons in a certain way. Relaxing the unidirectional assumption would mean that each electron-plasma wave would be enhanced differently, but each would still exist in the plasma. Each plasma wave would still scatter the wave at the same frequency, but the scattered-light intensity at that frequency would vary. Therefore, this assumption has no effect on the spectral positions of the bands, but only on the spectral shape of each band, for which no theory has been advanced.

Numerical calculations have shown that allowing the suprathermal electron distribution to have a finite energy width has little effect on the scattered light.<sup>63</sup> Intuitively, it is expected that a non-monoenergetic beam would produce wider scattering bands because the reverse-slope region for growth of the plasma waves

















































































